

DESIGN PARADIGM FOR MODULAR MULTILEVEL CONVERTER BASED
GENERATOR RECTIFIER SYSTEMS

A Dissertation

Submitted to the Faculty

of

Purdue University

by

Raj Sahu

In Partial Fulfillment of the

Requirements for the Degree

of

Doctor of Philosophy

August 2019

Purdue University

West Lafayette, Indiana

**THE PURDUE UNIVERSITY GRADUATE SCHOOL
STATEMENT OF DISSERTATION APPROVAL**

Dr. Scott D. Sudhoff, Chair

School of Electrical and Computer Engineering

Dr. Dionysios C. Aliprantis

School of Electrical and Computer Engineering

Dr. Steven D. Pekarek

School of Electrical and Computer Engineering

Dr. Jianghai Hu

School of Electrical and Computer Engineering

Approved by:

Dr. Dimitrios Peroulis

Head of the School Graduate Program

To my mother Manisha who selflessly devoted her life for me and my sister. Mother, there is nothing equivalent to your love and devotion, and I am forever indebted to you.

To *Vāsudeva* Krishna whom I may never understand, whom I blamed for all my faults, and who still helps me in his *mysterious* ways.

ACKNOWLEDGMENTS

No words can express my deepest gratitude to Dr. Scott Sudhoff, who helped and guided me in numerous ways during my PhD. I am very thankful to him for believing in me. I am also thankful to my committee members Dr. Steven Pekarek, Dr. Dionysios Aliprantis and Dr. Jianghai Hu for their valuable comments and suggestions. I am grateful to my fellow Power and Energy group colleagues for all their help during my doctoral study. I would like to thank the U.S. Office of Naval Research for supporting this project under award number N00014-16-1-2956.

TABLE OF CONTENTS

	Page
LIST OF TABLES	viii
LIST OF FIGURES	ix
ABSTRACT	xiii
1 Introduction	1
1.1 PMAC-MMC based Generator Rectifier System	3
1.2 Literature Review	5
1.3 Proposed Work	7
1.3.1 Approach	8
1.4 Organization of the dissertation	10
2 Metamodeling Of Electric Machines	12
2.1 Electric Machine Structure	13
2.2 Electric Machine Design Equations	13
2.2.1 Conductors, Current and Current Density	15
2.2.2 Winding Loss, Resistance, Volume and Electrical Mass	17
2.2.3 Field Analysis and Core Losses	19
2.2.4 Flux Linkage, Voltage, Torque, Power and Efficiency	22
2.3 Metamodel Formulation	23
2.4 Metamodel Usage	31
3 Waveform-level Model Of PMAC-MMC System	39
3.1 Variable definitions	40
3.2 Reference frame transformation	41
3.3 Generator rectifier model	42
3.4 Control Scheme	44
3.5 Modulation scheme and capacitor voltage balancing	47

	Page
3.5.1	Level-shifted Sinusoidal Pulse Width Modulation 47
3.5.2	Capacitor voltage balancing scheme 48
3.6	Simulation Results of Waveform-level Model 48
4	High-speed Simulation Of The PMAC-MMC system 53
4.1	Calculation of Generator Current, and DC and Fundamental Component of MMC Current 54
4.2	MMC AC side Fundamental Converter Voltage 55
4.3	Capacitor Voltage Ripple Calculations 56
4.4	Submodule Duty Cycle and Switching Signal Calculation 59
4.5	Currents in MMC Arm and DC Bus Capacitor 60
4.6	Total Loss Calculation and Convergence 61
4.7	Comparison between detailed and high-speed simulation model 64
4.7.1	Case A 64
4.7.2	Case B 68
4.7.3	Case C 71
4.8	Conclusions 74
5	Submodule Power Losses And Thermal Model 75
5.1	MMC Semiconductor Losses 75
5.1.1	Conduction Losses in Semiconductor Devices 76
5.1.2	Switching Losses in Semiconductor Devices 78
5.2	Semiconductor Loss Dissipation in Submodule 81
5.2.1	Forced Convection Heat Sink 81
5.2.2	Heat Sink Metamodel 90
5.3	Submodule Thermal Model 92
6	Passive Devices In Modular Multilevel Converter 95
6.1	Polypropylene Film Capacitor 95
6.2	MMC Arm Inductor 97
6.2.1	Permanent Magnet based E-E core Inductor 100

	Page
6.2.2 Standard EE-core Inductor	114
7 Multi-objective Optimization Of MMC Based Generator-Rectifier System .	118
7.1 Design Problem Formulation	118
7.1.1 Design Space	119
7.1.2 Design Constraints	121
7.1.3 Design Metrics	126
7.1.4 Design Fitness	128
7.2 PMAC-MMC Design Studies	131
7.2.1 Optimization Results	134
8 Conclusions And Future Work	147
REFERENCES	149
A Semiconductor Device Parameters	154
B Polypropylene Capacitor Model Parameters	155
C Inductor Material Parameters	156
D FEA Validations Of Inductor MEC	157
VITA	161

LIST OF TABLES

Table	Page
2.1 Variable Normalization	15
2.2 Variable Normalization 2	15
2.3 Scaled Design Search Space	24
5.1 Semiconductor Device Conduction Status	77
5.2 Devices exhibiting switching loss in switching cycle	79
5.3 Heat Sink Design Search Space	89
5.4 Heat Sink Metamodel Parameters	92
6.1 Core Branch Permeance Parameters	105
7.1 Fixed Design Parameters	122
7.2 Constraint Test	129
7.3 Pseudo-code for Calculation of the Fitness Function	129
7.4 Design Space for Case (a): EE-core Inductor	132
7.5 Design Space for Case (b): EE-PMI	133
7.6 Case (a) Design Results at 604 kg	143
B.1 Polypropylene Capacitor Model Parameters	155
C.1 FINEMET FT3-M Core Material Parameters	156
C.2 Permanent Magnet Parameters	156
D.1 EE-PMI Design Parameters	157
D.2 Standard EE-Core Design Parameters	159

LIST OF FIGURES

Figure	Page
1.1 PMAC-MMC Generator Rectifier System	4
1.2 H-bridge Converter based Submodule	4
1.3 Manual System Design Process [7]	5
1.4 Optimization based System Design Process [7]	5
1.5 MMC based Generator-Rectifier System Design Process	8
2.1 Surface Mounted PMAC Generator Structure [29]	14
2.2 Stator Developed Diagram [29]	14
2.3 Rotor Function [29]	19
2.4 Normalized Electromagnetic Volume vs Specific Torque Density	25
2.5 Normalized Electromagnetic Mass vs Specific Torque Density	26
2.6 Normalized Resistive Loss vs Specific Torque Density	26
2.7 Normalized Eddy Current loss vs Specific Torque Density	27
2.8 Normalized Hysteresis Loss vs Specific Torque Density	27
2.9 Generator Efficiency vs Specific Torque Density	28
2.10 Normalized Current Density vs Specific Torque Density	28
2.11 Normalized Resistance vs Specific Torque Density	29
2.12 Normalized q -axis Inductance vs Specific Torque Density	29
2.13 Referred Machine Terminal Line-line Voltage	30
2.14 Normalized Machine λ_m vs Specific Torque Density	30
2.15 Electromagnetic Volume vs Specific Torque Density	33
2.16 Electromagnetic Mass vs Specific Torque Density	33
2.17 Resistive Loss vs Specific Torque Density	34
2.18 Eddy Current Loss vs Specific Torque Density	34
2.19 Hysteresis Loss vs Specific Torque Density	35

Figure	Page
2.20 Generator Efficiency vs Specific Torque Density	35
2.21 Current Density vs Specific Torque Density	36
2.22 Resistance vs Specific Torque Density	36
2.23 Machine q -axis Inductance vs Specific Torque Density	37
2.24 Machine λ_m vs Specific Torque Density	37
2.25 Generator Dimensions vs Specific Torque Density	38
2.26 Generator Rotor Tip Speed vs Specific Torque Density	38
3.1 Modular Multilevel Converter	39
3.2 H-bridge Converter based Submodule Topology	40
3.3 DC Bus Voltage Control	45
3.4 Machine q - and d - axis Current Control	46
3.5 Second Harmonic Elimination in Arm Currents	47
3.6 Level-Shifted Sinusoidal PWM	49
3.7 Switching Scheme for Upper Arm of a -phase of the MMC	49
3.8 Generator Current	50
3.9 MMC Upper Arm Current	51
3.10 MMC Lower Arm Current	51
3.11 MMC Upper Arm Submodule Capacitor Voltage	52
3.12 MMC Lower Arm Submodule Capacitor Voltage	52
4.1 High-Speed Simulation Flow Chart for Generator-Rectifier System	63
4.2 Machine Current Comparison for Case A	65
4.3 MMC Upper Arm Current Comparison for Case A	66
4.4 MMC Lower Arm Current Comparison for Case A	66
4.5 MMC Upper Arm Submodule Capacitor Voltage Comparison for Case A	67
4.6 MMC Lower Arm Submodule Capacitor Voltage Comparison for Case A	67
4.7 Machine Current Comparison for Case B	69
4.8 MMC Upper Arm Current Comparison for Case B	69
4.9 MMC Lower Arm Current Comparison for Case B	70

Figure	Page
4.10 MMC Upper Arm Submodule Capacitor Voltage Comparison for Case B . . .	70
4.11 MMC Lower Arm Submodule Capacitor Voltage Comparison for Case B . . .	71
4.12 Machine Current Comparison for Case C	72
4.13 MMC Upper Arm Current Comparison for Case C	72
4.14 MMC Lower Arm Current Comparison for Case C	73
4.15 MMC Upper Arm Submodule Capacitor Voltage Comparison for Case C . . .	73
4.16 MMC Lower Arm Submodule Capacitor Voltage Comparison for Case C . . .	74
5.1 Semiconductor Devices Conduction Status	77
5.2 Switching Loss Instants in a Switching Period	79
5.3 Devices Exhibiting Switching Loss in Switching Period	80
5.4 Structure of Parallel Plate Fin Heat Sink	81
5.5 Equivalent Thermal Circuit of Heat Sink per Fin Gap	83
5.6 Pareto-optimal Front of the Design	90
5.7 Heat Sink Dimensions vs Heat Sink Mass	91
5.8 Fan Power vs Heat Sink Mass	91
5.9 Fan power vs Thermal Resistance	92
5.10 Equivalent Thermal Model Circuit for Submodule	93
6.1 MMC Machine Current for Modified Study from Chapter 3	99
6.2 MMC Upper Arm Current for Modified Study from Chapter 3	99
6.3 EI-core PMI geometry	101
6.4 Nanocrystalline Core Material [54]	102
6.5 FINEMET based EE-core PMI geometry	103
6.6 EE-PMI Magnetic Equivalent Circuit	104
6.7 Air Gap Fringing Paths in EE-PMI	106
6.8 Horizontal Flux Leakage in EE-PMI	107
6.9 Ideal Conductor Packing in the Winding	109
6.10 EE-core Inductor Geometry	116
6.11 Standard EE-core Inductor MEC	117

Figure	Page
7.1 System Loss vs Mass	135
7.2 Case (a): Standard EE-core MMC Parameter Distribution	135
7.3 Case (b): Standard EE-PMI MMC Parameter Distribution	136
7.4 Generator Specific Torque Density	136
7.5 Electrical Fundamental Frequency	137
7.6 MMC Arm Inductance	137
7.7 Switching Frequency	138
7.8 Submodule Capacitance	138
7.9 Number of submodules	139
7.10 DC Bus Capacitance	139
7.11 Generator q -axis Current	140
7.12 Case (a): System Component Loss	140
7.13 Case (b): System Component Loss	141
7.14 Case (a): System Component Mass	141
7.15 Case (b): System Component Mass	142
7.16 Generator Current	144
7.17 MMC Upper Arm Current	144
7.18 MMC Lower Arm Current	145
7.19 MMC Upper Arm Submodule Capacitor Voltage Ripple	145
7.20 MMC Lower Arm Submodule Capacitor Voltage Ripple	146
D.1 EE-PMI Geometry	158
D.2 EE-PMI FEA Validation	158
D.3 EE-Core Geometry	159
D.4 EE-Core FEA Validation	160

ABSTRACT

Sahu, Raj Ph.D., Purdue University, August 2019. Design paradigm for Modular Multilevel Converter based Generator Rectifier Systems. Major Professor: Scott D. Sudhoff.

Modular Multilevel Converters (MMC) are being widely considered for medium to high voltage DC generation systems. Integrated system design optimization of the generator-MMC system through multi-objective optimization is of interest, because such an approach allows the trade-off between competing objectives (for example, mass and loss) to be explicitly and quantitatively identified. In this work, such an optimization based design paradigm for MMC based generator rectifier systems is developed. To formulate the design problem as a multi-objective optimization problem, it is required that the system waveforms can be obtained to facilitate the imposition of constraints and the estimation of power losses. Similarly, it is also desired to include detailed electric machine magnetic and electrical analysis in design optimization, as well as aspects such as the inductor and heat sink design. Such development typically requires detailed component design and simulation models for the electric machine and converter which are computationally expensive. As an alternative, the proposed work utilizes an electric machine metamodel, heat sink metamodel, and high-speed steady-state simulation model for the MMC to facilitate multi-objective optimization minimizing system metrics of interest while satisfying system constraints. Using the developed component simulation and design models, a multi-objective optimization based design of an MMC based generator-rectifier system is conducted.

1. INTRODUCTION

For long distance power transmission, High Voltage DC (HVDC) based transmission has several advantages over traditional AC power transmission which include efficient operation, lower cost for bulk transmission than High Voltage AC (HVAC), and the capability to exchange power between two asynchronous systems [1]. Due to zero reactive power transport and smaller footprint, HVDC transmission losses are reduced relative to HVAC power transmission. Historically, reduced transmission loss has been the primary reason for the development of HVDC based transmission. However, in recent times, willingness to integrate more renewable energy sources into traditional power systems has also encouraged the implementation of HVDC based transmission [2]. In particular, increased penetration of offshore renewable sources of energy, for example, offshore wind farms and solar farms, favor HVDC power based transmission over conventional AC transmission [2].

Similarly, for microgrid operation, Medium Voltage DC (MVDC) power distribution is being widely studied. For example, in shipboard power systems, the MVDC based Integrated Power System (IPS) promises efficient operation of the system with high power density and is under development to be implemented in future ships [3,4]. MVDC based power system architecture allows for a highly reliable operation with increased survivability [3].

In such DC power transmission/distribution systems, power electronic converters are ubiquitous. Historically, the thyristor based 2-level Line Commuted Converter (LCC) has been used for HVDC conversion. However, the switching frequency for such converters is limited for high voltage operation due to increased switching losses. Such converters require large filters (mass and volume wise) to improve harmonic performance, and to address the power quality at the input and output of the converter. On the other hand, multilevel converters have been successful in efficient operation of

medium to high voltage drive and rectifier systems [5,6]. The design is such that the DC bus voltage is distributed over a number of power sub-stages so that each power electronic switch observes a low voltage stress. This allows low voltage switches to be used. The AC side of multilevel converters exhibits multiple voltage levels, as compared to 2-levels in 3-phase full-wave bridge rectifiers. The harmonic content and Total Harmonic Distortion (THD) of AC side voltage can be greatly reduced by increasing the number of voltage levels in multilevel converters, and hence multilevel converters are being widely studied for their implementation in industry for medium to high voltage DC operation. This work considers such multilevel converters for rectification operation.

For the application in MVDC/HVDC operation, several multilevel converter topologies have been proposed in the literature including the Neutral Point Clamped (NPC) converter, the cascaded H-bridge converter, and the Modular Multilevel Converter (MMC) [5]. Of the topologies proposed, the Modular Multilevel Converter is particularly attractive for medium to high voltage DC applications due to its inherent modularity, scalability, and highly efficient performance as compared to other multilevel converter topologies [5], [6]. Hence, an MMC based system is considered herein.

The goal of this research is to develop a design paradigm for MVDC/HVDC generator-rectifier system which utilizes Permanent Magnet AC (PMAC) machine for generation and an MMC for rectification. Integrated design optimization of such systems is complex due to large number of design variables [7]. Consider, for example, the generator design. The generator fundamental electrical frequency and speed are considered to be unknowns which has direct impact on the generator as well as multilevel converter and passive component sizing. Optimal design of generator dimensions, currents, core-material, and winding itself is a complex multi-objective optimization problem [7]. Now consider optimal design of the multilevel converter along with the generator while considering the generator converter interaction. A modification in fundamental duty cycle or number of AC voltage levels in the multilevel converter could require modifications in generator winding, passive filters, current rating of the

generator, switching frequency etc. for the optimal system design. There are multiple similar design variables in the system design which closely interact with each other to impact the overall system performance.

In this dissertation, a system design process is explored which can simultaneously address the generator and the MMC while optimizing the overall system for design metrics of interest as well as considering the interaction and operational aspects of the two subsystems. In subsequent sections of this chapter, the system structure is introduced, the design problem is defined, a literature survey is conducted, and finally the goals of the work along with discussion on content of this dissertation are presented.

1.1 PMAC-MMC based Generator Rectifier System

The generator rectifier system considered is shown in Fig. 1.1. The MMC (shaded) contains 6 arms with an ‘upper’ and ‘lower’ arm associated with each phase. Each MMC arm has a filter inductor to filter the harmonic component of currents in leg and a total of N submodules connected in series, shown as the **SB** block in Fig. 1.1. Several submodule topologies have been proposed in literature [5], [6], however the two most commonly implemented topologies are the half-bridge converter and the H-bridge (full-bridge) converter. In this work, H-bridge converter submodule topology, shown in Fig. 1.2, will be considered due to its inherent fault blocking capability. The considered submodule contains 4 semiconductor switches, 4 power diodes, and a submodule capacitor. Detailed variable definitions and analysis are presented in Chapter 3.

One active area of MMC research is its optimal design. Selection of the number of submodules to be used in the MMC is important. Increasing the number of submodule reduces the harmonic content in the arm currents, but adds additional conduction losses, mass, and control complexity. The submodule volume and mass depends on the current and voltage ratings. The arm inductor also adds to the mass of the

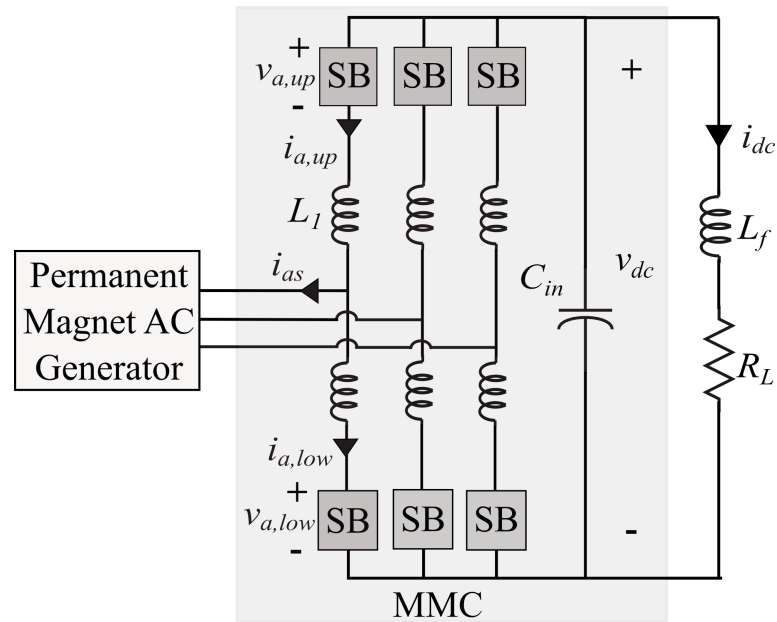


Fig. 1.1. PMAC-MMC Generator Rectifier System

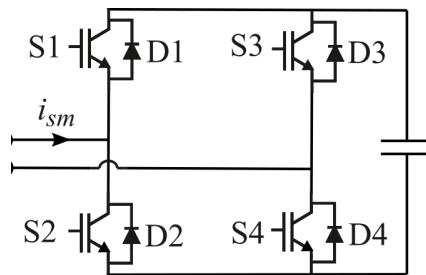


Fig. 1.2. H-bridge Converter based Submodule

MMC structure, but reduces the harmonic content in the arm current. Similarly, the selection of switching frequency is important. Excessive switching frequency could lower the mass of the passives but yield high losses which in turn could increase heat sink mass. As mentioned earlier, at the source side, varying PMAC generator parameters changes the MMC current, and could change the current rating and size of switches and passive components. Hence, development of an optimal system design methodology is of interest. It is also necessary that the designed system satisfies various constraints, for example, maximum allowed capacitor voltage ripple. Clearly,

the PMAC-MMC system design problem is complex and it requires many operational aspects to be simultaneously taken into consideration. Previous work to address these challenges is next reviewed.

1.2 Literature Review

In the literature, the design problem is usually approached by one of two methods: (a) manual design where design parameters are selected based on design equations as shown in Fig. 1.3, (b) optimization based design as shown in Fig. 1.4 [7].

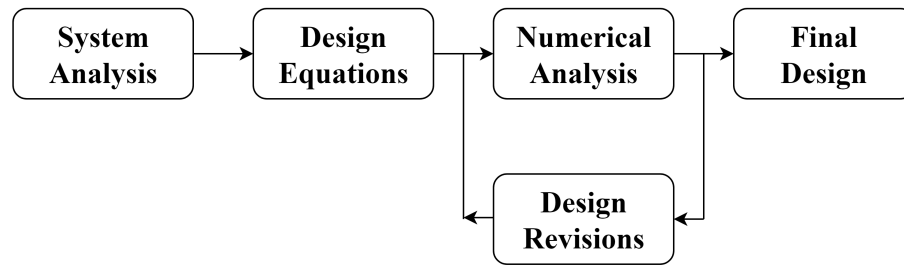


Fig. 1.3. Manual System Design Process [7]

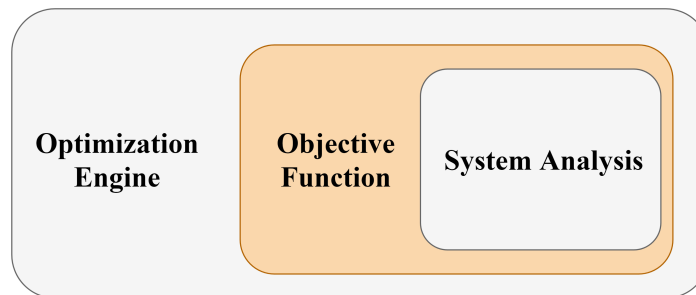


Fig. 1.4. Optimization based System Design Process [7]

Manual Design Methods for MMC

Manual methods select parameters based on design equations derived from an approximate system analysis, as shown in Fig. 1.3. Of those, many MMC design methods are based on specifying passive component values, namely the arm inductance and submodule capacitance. These passive values are selected based on predefined steady state and transient conditions, and system constraints as discussed in [8–13]. In particular, the arm inductance specification is calculated based on limiting the peak-peak amplitude of the arm circulatory current in [8], limiting second harmonic current and the worst case DC short current in the arms in [9] and the worst case DC short current in the arms in [10]. The submodule capacitor is selected based on maximum allowed voltage ripple, a submodule voltage capability requirement and a maximum capacitor ripple current in [10]; maximum allowed voltage ripple and maximum allowed voltage in [11] and maximum allowed voltage ripple in [12, 13]. These methods provide a means for the system designer to determine component values. However, they do not provide an exploration of the trade-off between competing objectives and the MMC may not be optimal in a loss vs mass/volume sense.

An extension of the manual approach is to devise sensitivity functions or calculate performance trends vs system parameters to identify trade-offs using a detailed MMC simulation or approximate analysis [14–16]. Sensitivity based methods are insightful but do not fully explore the design space. Further, methods [14–16] do not develop a formal multi-objective optimization design procedure, which is a major goal this work.

Optimization Based Design

These methods are based on an optimization approach, as shown in Fig. 1.4. Such methods require a detailed system analysis, based on which a objective function is devised. That objective function is optimized for required goals using an optimization engine.

Work presented in [17] and [18] move towards a formal multi-objective optimization of the MMC, minimizing two competing objectives such as system volume and loss. In [17] a detailed waveform-level simulation model is utilized to develop the multi-objective optimization problem for MMC design. Due to the computationally expensive nature of detailed waveform-level simulation model, [17] is highly computationally demanding. In [18] an MMC design method for steady-state operation minimizing system loss and volume is presented assuming a fixed fundamental and switching frequency. While useful, neither [17] nor [18] consider the generator design, and both consider a simplified magnetic analysis of the arm inductor neglecting its core losses. Hence, [17] and [18] are not applicable for the problem considered in this paper where the source generator is also considered along with the details of inductor design and variation in fundamental frequency and switching frequency.

Multi-objective optimization of DC generation system has been discussed in [19–22]. The authors develop an optimization based design paradigm minimizing system mass and loss for a low power MVDC generation system which optimizes the generator along with 2-level rectifier. Optimal design of system utilizing wound rotor synchronous machine, PMAC machine and hybrid machines is presented where major focus of the research is on development of optimal generator design methods [19–21]. In [22], multi-objective optimization of low power DC generator system utilizing PMAC generator and wide-band gap devices is shown while considering the transient behaviour of the 2-level converter. While useful, none of the presented works in [19–22] consider HVDC applications or multilevel converters in the design optimization.

1.3 Proposed Work

The purpose of this work is to formulate a formal multi-objective optimization based design paradigm for the generator-rectifier system shown in Fig 1.1. The novelty of this work exists in efficient inclusion of electric machine and arm inductor magnetic

design in the system optimization, utilization of high-speed simulation model for MMC, the extensive exploration of the design space, and establishing performance trade-offs in a time-efficient manner. The design process adopted for this paper is shown in Fig. 1.5.

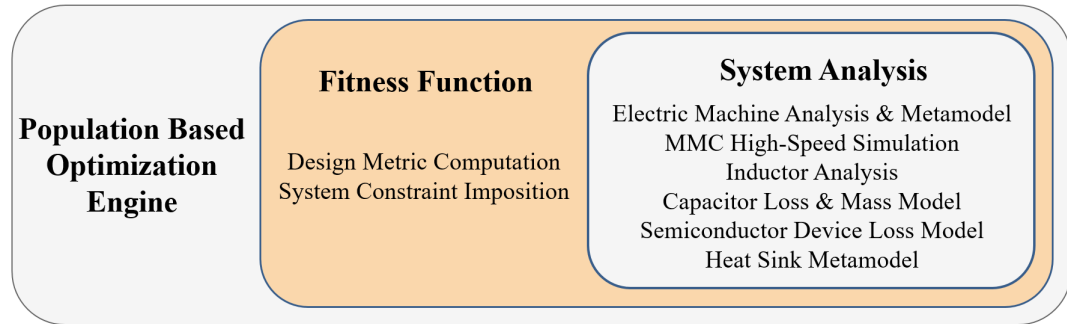


Fig. 1.5. MMC based Generator-Rectifier System Design Process

1.3.1 Approach

As explained, the goal is to create a multi-objective optimization based design method for the PMAC-MMC system. Evolutionary algorithms are widely used to solve multi-objective optimization problems. In this work, genetic algorithm will be used to solve the PMAC-MMC design optimization problem. Some operating condition constraints desired to be satisfied by the design solution are:

1. Generator, MMC and load power requirements are satisfied.
2. Component current density limits are satisfied.
3. Capacitor voltage and current ripple is within limits.
4. Switching frequency is within specified limits.
5. Harmonic component of leg currents are within required specifications.
6. Inductor core flux density limits and dimensional limits are satisfied.
7. Heat sink and submodule thermal constraints are satisfied.

To formulate a multi-objective optimization problem involving PMAC-MMC system design, it is required that the system waveforms can be obtained so as to estimate losses and impose constraints related to the proper operation of the MMC. In particular, steady-state waveforms of the system are of interest. These waveforms are particularly important in the MMC arm inductor design, and selection of submodule capacitor, switching frequency and the number of submodules. For example, arm current waveforms will be used to calculate steady-state inductor losses, and find appropriate inductance value so as to limit current ripple. Similarly, submodule capacitor voltage waveforms will be used for loss and voltage ripple calculations. However, these attributes are a function of the properties of the components designed. Also, multi-objective optimization will require a time domain simulation for every evaluation of the objective function, and so may require on the order of 10^4 - 10^6 time domain simulations. Hence, detailed simulation models of MMCs will result in a slow execution of the optimization engine and are not ideal for a such design approach. Hence a method for fast estimation of the MMC waveforms is required. This work proposes a high-speed simulation of the MMC to be used in a multi-objective design environment.

Similarly, designing generator is in-itself a multi-objective optimization problem minimizing its mass and loss. Detailed machine design procedure have been proposed in literature [7, 19–21], however, to reduce the computational burden of electric machine design but still retain the details of its design, a metamodel approach of the generator design is taken. The generator metamodel is advantageous relative to traditional machine scaling equations as it does detailed analysis of the generator as well as quickly estimates the trade-off between the machine mass and loss, and poses a reduced computational burden to the overall system optimization.

For the filter inductor of MMC arm, details in inductor magnetic design are considered for a standard and permanent magnet inductor. Similarly, capacitor and semiconductor device models are presented using the data from manufacturer data-

sheets. Finally, a forced air heat-sink metamodel is developed to account for the heat dissipation system in MMC.

The proposed design method will start with the development of component analysis and system simulation models for components utilized in Fig. 1.1. These include the electric generator design model, MMC high-speed simulation model, semiconductor (power electronic switch and diode) and passive devices (arm inductor, submodule capacitor) models, and heat-sink metamodel. Next, using the detailed analysis of components, a multi-objective fitness (objective) function will be formulated which imposes various system constraints required for system operation, and calculates the metrics of interest. Optimization of the fitness function yields the Pareto-optimal set of designs. Finally, multi-objective optimization of a notional PMAC-MMC system is carried out to demonstrate the functionality of the proposed design paradigm.

1.4 Organization of the dissertation

The organization of this work is as follows:

- Chapter 2 develops metamodel of a Permanent Magnet AC generator. This chapter will introduce the notion of scaled electric machine design, and then develop a metamodel from the results of multi-objective optimization of the scaled electric machine design paradigm.
- Chapter 3 develops the waveform-level model of the PMAC MMC generator rectifier system. This model will be used as reference to verify the results from a high-speed simulation model proposed in Chapter 4.
- Chapter 4 develops a high-speed simulation of the MMC to rapidly calculate PMAC-MMC system waveforms. This chapter also includes various system waveforms for different test cases so as to validate high-speed simulation model using detailed simulation model developed in Chapter 3.

- Chapter 5 presents semiconductor device models to calculate conduction and switching losses, and a forced air heat sink metamodel which will be utilized to develop thermal model of the submodule.
- Chapter 6 presents models for the submodule capacitor, and the detailed design model of permanent magnet based EE-core inductor and standard EE-core inductor.
- Chapter 7 sets forth a multi-objective optimization based design paradigm for a PMAC-MMC system. This involves development of optimization problem by describing the design space and the variables, calculation of mass and loss using the developed design/simulation models, and imposition of several constraints. Finally a case study is presented to demonstrate the functionality of the proposed design paradigm.
- Chapter 8 concludes the work with a discussion of future research.

2. METAMODELING OF ELECTRIC MACHINES

In the introduction of the work, it was shown that the development of optimal design method for the considered generator-rectifier system includes consideration of the generator. A straightforward approach is to select the generator from available manufacturer catalogues. This method of selection is fast and doesn't require detailed machine analysis, however, it is generally unknown how close the available machines come to the optimum for the considered system. A catalogue of relevant machines maybe sparse for some applications, and a high-performance system such as marine or aerospace application requires the machine to be as optimal as possible as the system size is of great importance in such applications. Hence generator selection from an available catalogue may not be ideal.

One method to overcome the shortcomings of a catalogue based selection is to develop a detailed electric machine design and optimization procedure. Such methods include a detailed analysis of electric machine including its field and loss calculations, and implement multi-objective optimization of the machine, satisfying a set of constraints while minimizing the metrics of interests by formulating an appropriate objective function [7]. The outcome of such design methods is set of non-dominated designs, called a Pareto-optimal front, which enables the system designer to extensively explore the system design space based on system requirements. Though very useful, such methods are computationally too intense to be included in a global multi-objective optimization wherein a MMC and its components are optimized along with a generator, while satisfying the system operating requirements. A detailed machine design procedure would create a large search space, and hence may lead to a sub-optimal solution during optimization due to insufficient computational resources.

To overcome the slowness of the detailed machine design procedures, scaling equations have been formulated in literature [23–28]. These scaling equations can quickly

predict machine size based on power or torque requirements, however, at cost of inaccurate machine loss calculations. Work presented in [23–26] do not incorporate the losses in machine which is important as it directly impacts range and cooling requirements. Authors in [27, 28] consider resistive losses but neglect core losses and its variation with speed. None of the work presented in [23–28] present a trade-off between machine size and its losses which is important from a system optimization perspective. Hence a method is required which can predict the trade-offs between competing objectives while requiring low computational resources with a reasonable model accuracy.

To address the aforementioned issues presented for the electric machine design, authors in [29] present a electric machine metamodeling procedure. A metamodel is a model of a model. Metamodel captures the details in electric machine design while itself poses a low computational demand on the global optimization problem. This chapter presents development of such electric generator metamodel.

2.1 Electric Machine Structure

To formulate an electric machine metamodel, a machine topology must be selected. Herein, a surface mounted permanent magnet AC (PMAc) generator is considered as shown in Fig. 2.1. Dimensions have been defined in the figure except shaft radius which is r_{sh} . The active stator region includes the stator teeth and slots, and the stator conductors within the slots. A portion of developed diagram of stator is shown in Fig. 2.2 with dimensions of stator slot and tooth. A more detailed description of machine geometry is presented in [7].

2.2 Electric Machine Design Equations

A detailed electric machine design model has been presented in [7] and [29], however, for completeness a brief overview of the design equations is shown herein. In this work, a scale independent normalized electric machine design procedure is uti-

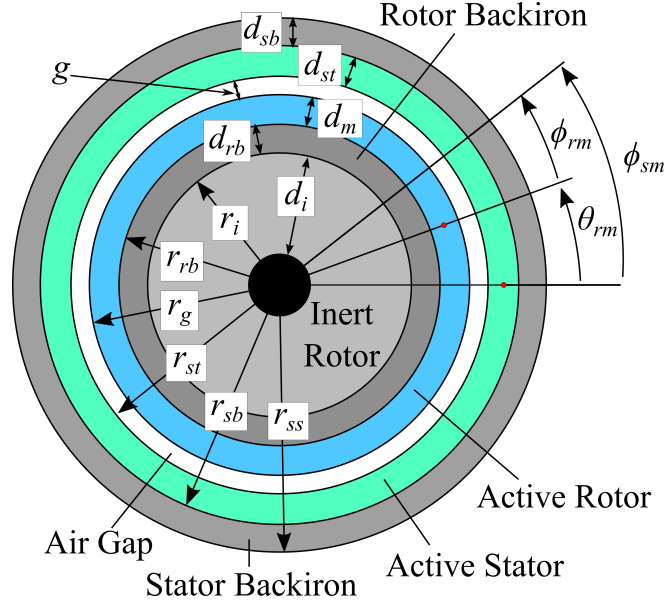


Fig. 2.1. Surface Mounted PMAC Generator Structure [29]

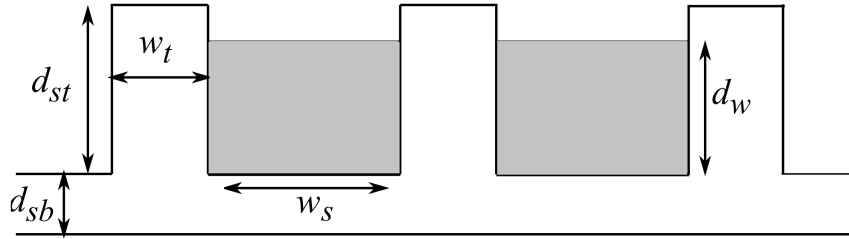


Fig. 2.2. Stator Developed Diagram [29]

lized which formulates design equation based on a common base, and can be utilized to generate a metamodel. A general variable normalization philosophy for power magnetic devices is presented in [29] and [30]. Table 2.1 presents the variable normalization definitions. Flux density and voltage are not scaled. In Table 2.1 the normalization base D is the reference output power at generator terminals $P_{out,g}^*$.

In addition to aforementioned normalization, some variables will be normalized with respect to fundamental component of peak value of conductor density, N_{s1} . These variables will be denoted with a (') and described as 'referred'. The variables

normalized with N_{s1} are shown in Table 2.2. Next, scaled electric machine design

Table 2.1.
Variable Normalization

Parameter	Normalization	Parameter	Normalization
Length	$\hat{x} = x/D$	Area	$\hat{a} = a/D^2$
Volume	$\hat{v} = v/D^3$	Mass	$\hat{M} = M/D^3$
Current	$\hat{i} = i/D$	Current Density	$\hat{J} = JD$
Power	$\hat{P} = P/D$	Torque	$\hat{T} = T/D^3$
Time	$\hat{t} = t/D^2$	Frequency	$\hat{f} = fD^2$
Angular Speed	$\hat{\omega} = \omega D^2$	Flux Linkage	$\hat{\lambda} = \lambda/D^2$
Resistance	$\hat{R} = RD$		

Table 2.2.
Variable Normalization 2

Parameter	Referred Quantity	Parameter	Referred Quantity
Current	$i' = iN_{s1}$	Resistance	$R' = R/N_{s1}^2$
Inductance	$L' = L/N_{s1}^2$	Voltage	$V' = V/N_{s1}$
Flux Linkage	$\lambda' = \lambda/N_{s1}$	Conductor Density	$n' = n/N_{s1}$
Winding Function	$w' = w/N_{s1}$		

equations are presented [29].

2.2.1 Conductors, Current and Current Density

This section sets forth equations for calculation of machine winding function, slot area fraction and current density for assumed machine geometry, slot conductor density and machine currents [29].

The referred slot conductor density in generator a - phase, n'_{as} , is assumed to be of the form

$$n'_{as} = \sin(\phi_s) - \alpha_3 \sin(3\phi_s) \quad (2.1)$$

where ϕ_s is $P/2$ times ϕ_{rm} . It is convenient to define the total referred number of slot conductors in one direction, N'_s , and the peak slot conductor density, k_n , as

$$N'_s = \frac{1}{2} \int_0^{2\pi} |n'_{as}| d\phi_s \quad (2.2)$$

$$k_n = \max(|n'_{as}| + |n'_{bs}| + |n'_{cs}|) \quad (2.3)$$

Using [7, 29], the referred end conductor density m'_{as} can be expressed as

$$m'_{as} = -\frac{2}{P} \left(\cos(\phi_s) - \frac{\alpha_3}{3} \cos(3\phi_s) \right) \quad (2.4)$$

for which the number of end conductors, M'_s , and peak end conductor density, k_m can be calculated as

$$M'_s = \frac{1}{2} \int_0^{2\pi} |m'_{as}| d\phi_s \quad (2.5)$$

$$k_m = \max(|m'_{as}| + |m'_{bs}| + |m'_{cs}|) \quad (2.6)$$

From [7], the q - and d - axis normalized winding functions can be expressed

$$w'_{qs} = \frac{2}{P} (\cos(\theta_r - \phi_s)) \quad (2.7)$$

$$w'_{ds} = \frac{2}{P} (\sin(\theta_r - \phi_s)) \quad (2.8)$$

where θ_r is $P/2$ times θ_{rm} . Similarly, the normalized q - and d - axis generator currents can be calculated as

$$\hat{i}'_{qs} = \sqrt{2} \hat{I}'_s \cos \phi_i \quad (2.9)$$

$$\hat{i}'_{ds} = -\sqrt{2} \hat{I}'_s \sin \phi_i \quad (2.10)$$

where \hat{I}'_s is the rms normalized generator current. Using [7], the stator slot area fraction α_{ssaf} is given by

$$\alpha_{ssaf} = 1 - \frac{2(1 - \alpha_{ss})}{2 + \frac{\hat{d}_{st}}{\hat{r}_{st}}} \quad (2.11)$$

where α_{ss} is fraction of the angle spanned by a stator slot over the angle spanned by a slot and tooth. Slot conductor packing factor k_{pfs} can be calculated as

$$k_{pfs} = \frac{2k_n \hat{a}'_c}{\hat{r}'_{sb}{}^2 - \hat{r}'_{st}{}^2 \alpha_{ssa f}} \quad (2.12)$$

where \hat{a}'_c is cross-sectional area of the conductor. Finally, the machine rms current density \hat{J}_{rms} is given as

$$\hat{J}_{rms} = \frac{\hat{I}'_s}{\hat{a}'_c} \quad (2.13)$$

2.2.2 Winding Loss, Resistance, Volume and Electrical Mass

This subsection describes calculation of conductor resistance and its losses, and volumes of different parts of the generator [29].

The normalized effective slot length can be computed as

$$\hat{l}_{seff} = \hat{l} + \alpha_{ew} \frac{k_m k_{pfs} \alpha_{ssa f} (\hat{r}'_{sb} + \hat{r}'_{st})}{2k_n k_{pfe} \alpha_{dw}} \quad (2.14)$$

where \hat{l} is the length of slot, α_{dw} is the depth of the winding relative to the slot, k_{pfe} is end winding packing factor, α_{ew} is factor to account for conductor protrude from the ends of the slot and is taken as 2. Using (2.14), the normalized total electric length of the machine \hat{l}_{te} is calculated as

$$\hat{l}_{te} = \hat{l} + (\alpha_{ew} + 1) \frac{k_m k_{pfs} \alpha_{ssa f} (\hat{r}'_{sb} + \hat{r}'_{st})}{2k_n k_{pfe} \alpha_{dw}} \quad (2.15)$$

One phase conductor volume for slot and end region, \hat{v}_{cspp} and \hat{v}_{cepp} respectively, can be expressed

$$\hat{v}_{cspp} = 2\hat{l}_{seff} \hat{a}'_c N'_s \quad (2.16)$$

$$\hat{v}_{cepp} = (\hat{r}'_{sb} + \hat{r}'_{st}) \hat{a}'_c M'_s \quad (2.17)$$

The slot and end region conductor resistances, \hat{R}'_{ss} and \hat{R}'_{se} , respectively, for one phase of the machine can be calculated using conductor volume and conductance σ as

$$\hat{R}'_{ss} = \frac{\hat{v}_{cspp}}{\hat{a}'_c \sigma} \quad (2.18)$$

$$\hat{R}'_{se} = \frac{\hat{v}_{cepp}}{\hat{a}'_c \sigma} \quad (2.19)$$

using which the total conductor resistive loss \hat{P}_r is computed as

$$\hat{P}_r = 3\hat{R}'_s \hat{I}'_s{}^2 = 3(\hat{R}'_{ss} + 2\hat{R}'_{se}) \hat{I}'_s{}^2 \quad (2.20)$$

Next, the total volumes of slot conductor \hat{v}_{cs} , end region conductor \hat{v}_{ce} , stator backiron \hat{v}_{sb} , stator teeth \hat{v}_{st} , permanent magnet \hat{v}_{pm} , rotor backiron \hat{v}_{rb} , and the rotor inert region \hat{v}_{ri} can be calculated as

$$\hat{v}_{cs} = 3\hat{v}_{cspp} \quad (2.21)$$

$$\hat{v}_{ce} = 3\hat{v}_{cepp} \quad (2.22)$$

$$\hat{v}_{sb} = \pi \hat{l} (\hat{r}_{ss}^2 - \hat{r}_{sb}^2) \quad (2.23)$$

$$\hat{v}_{st} = \pi \hat{l} (\hat{r}_{sb}^2 - \hat{r}_{st}^2) (1 - \alpha_{ssaf}) \quad (2.24)$$

$$\hat{v}_{pm} = \pi \hat{l} (\hat{r}_{rg}^2 - \hat{r}_{rb}^2) \alpha_{pm} \quad (2.25)$$

$$\hat{v}_{rb} = \pi \hat{l} (\hat{r}_{rb}^2 - \hat{r}_{ri}^2) \quad (2.26)$$

$$\hat{v}_{ri} = \pi \hat{l} (\hat{r}_{ri}^2 - \hat{r}_{rs}^2) \quad (2.27)$$

In (2.25) α_{pm} the fraction of angle spanned by the pm over 2π . The circumscribing volume of the generator, \hat{v}_{te} , is computed using

$$\hat{V}_{ge} = \pi \hat{l}_{te} \hat{r}_{ss}^2 \quad (2.28)$$

Using the calculated volumes, the mass of stator steel \hat{M}_{ss} , rotor steel \hat{M}_{rs} , magnet \hat{M}_{pm} and conductors \hat{M}_c can be calculated as

$$\hat{M}_{ss} = \rho_s (\hat{v}_{sb} + \hat{v}_{st}) \quad (2.29)$$

$$\hat{M}_{rs} = \rho_r \hat{v}_{rb} \quad (2.30)$$

$$\hat{M}_{pm} = \rho_m \hat{v}_{pm} \quad (2.31)$$

$$\hat{M}_c = \rho_c (\hat{v}_{cs} + 2\hat{v}_{ce}) \quad (2.32)$$

where ρ_s, ρ_r, ρ_m and ρ_c are stator steel, rotor steel, magnet and conductor mass densities, respectively.

Machine electromagnetic mass is defined as mass except structure, case and cabinet mass of the machine. Using calculated component mass in (2.29)-(2.32), the total electromagnetic generator mass \hat{M}_{ge} is given as

$$\hat{M}_{ge} = \hat{M}_{ss} + \hat{M}_{rs} + \hat{M}_{pm} + \hat{M}_c \quad (2.33)$$

2.2.3 Field Analysis and Core Losses

This subsection presents the magnetic field analysis and the calculation of core losses in different parts of the machine using [29]. In this analysis, it is assumed that $\theta_r = 0$, so that $\phi_r = \phi_s$. As shown in Fig.2.3, the functions μ_{rm} and B_m describe the relative permeability and residual magnetization of the material in the rotor active region. Therein, B_r and χ_m are residual magnetization and incremental susceptibility, respectively, of the magnet.

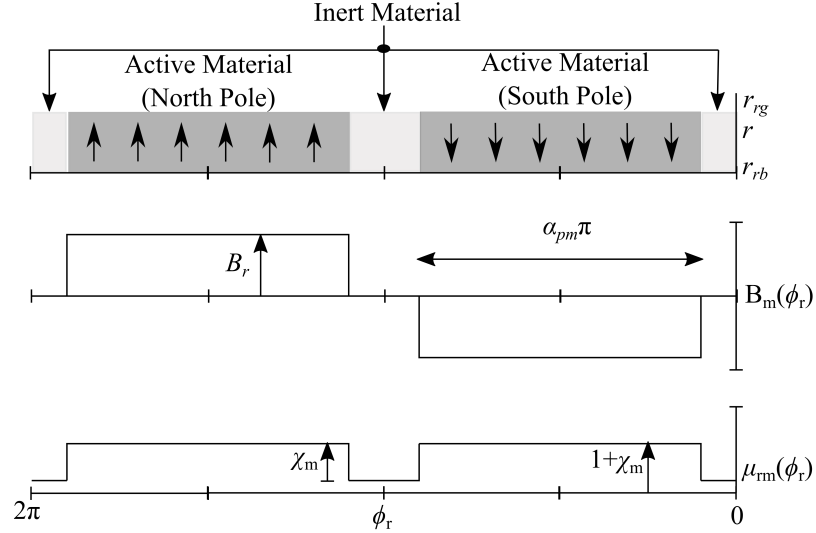


Fig. 2.3. Rotor Function [29]

The stator MMF due to winding currents, \hat{F}_s , and rotor MMF due to permanent magnet, \hat{F}_m , can be expressed as

$$\hat{F}_s = \frac{3\sqrt{2}}{P} \hat{I}'_s \cos(\phi_r - \phi_i) \quad (2.34)$$

$$\hat{F}_m = \frac{\hat{d}_m}{\mu_0 \mu_{rm}(\phi_r)} B_m(\phi_r) \quad (2.35)$$

The quantities \hat{R}_m and \hat{R}_g are the reluctance densities associated with active rotor and airgap, and are computed as

$$\hat{R}_m = \frac{\hat{r}_{rb}}{\mu_0 \mu_{rm}(\phi_r)} \ln \left(1 + \frac{\hat{d}_m}{\hat{r}_{rb}} \right) \quad (2.36)$$

$$\hat{R}_g = \frac{\hat{r}_{rb}}{\mu_0} \ln \left(1 + \frac{c_s \hat{g}}{\hat{r}_{rb} + \hat{d}_m} \right) \quad (2.37)$$

Using the Gauss's law, as shown in [7,29], the radial flux density at the rotor backiron, B_{rrb} , is given by

$$B_{rrb} = \frac{\hat{F}_s + \hat{F}_m}{\hat{R}_m + \hat{R}_g} \quad (2.38)$$

The minimum field intensity in the positively magnetized region of the magnet is calculated as

$$H_{mn} = \frac{\hat{r}_{rb}}{\hat{r}_g} \left(\frac{\min_{\phi_s, B_m > 0} (B_{rrb})}{\mu_0 (1 + \chi_m)} \right) \quad (2.39)$$

Next, the tangential component of the flux density in the rotor backiron, B_{trb} , satisfies

$$(\hat{d}_{rb} B_{trb}) = -\frac{2}{P} \hat{r}_{rb} \left[\int_0^{\phi_s} B_{rrb} d\phi - \frac{1}{2} \int_0^\pi B_{rrb} d\phi \right] \quad (2.40)$$

using which the normalized depth of the rotor backiron \hat{d}_{rb} can be computed as

$$\hat{d}_{rb} = \frac{\max(\hat{d}_{rb} B_{trb})}{B_{r,lim}} \quad (2.41)$$

From [29], the magnetizing component of the radial flux density inside the stator tooth, B_{rstm} , is determined as

$$B_{rstm}(\phi_s) = \frac{6n_{spp}}{2\pi(1 - \alpha_{ss})} \int_{\phi_s - \frac{\pi}{6n_{spp}}}^{\phi_s + \frac{\pi}{6n_{spp}}} \frac{\hat{r}_{rb} B_{rrb}}{\hat{r}_{st}} d\phi \quad (2.42)$$

where n_{spp} is the number of slots per pole per phase. Similarly, the counterclockwise directed tangential component of the magnetizing flux density, B_{tsbm} is given by

$$B_{tsbm} = -\frac{\hat{d}_{rb}B_{trb}}{\hat{d}_{sb}} \quad (2.43)$$

The effective radial flux density in the stator tooth, B_{rstl} , and stator backiron, B_{tbsl} are given as

$$B_{rstl} = \mu_0 \frac{3\sqrt{2}P}{8(1-\alpha_{ss})} \frac{\hat{d}_{st}^2 k_{pfs}}{\hat{r}_{st} k_n} \alpha_{dw} (2 - \alpha_{dw}) \hat{J}_{rms} \cos(\phi_s - \phi_i) \quad (2.44)$$

$$B_{tbsl} = \mu_0 \frac{3\sqrt{2}P}{4} \frac{\hat{d}_{st}^2 k_{pfs}}{\hat{d}_{sb} k_n} \alpha_{dw} (2 - \alpha_{dw}) \hat{J}_{rms} \sin(\phi_s - \phi_i) \quad (2.45)$$

The derivation of (2.44) and (2.45) has been provided in [29]. Finally, the flux density in stator tooth, B_{st} , and tangential stator backiron flux density, B_{tsb} , can be expressed using

$$B_{st} = B_{rstm} + B_{rstl} \quad (2.46)$$

$$B_{tsb} = B_{tsbm} + B_{tbsl} \quad (2.47)$$

Next, the hysteresis loss density in the core will be calculated using [29] as

$$\hat{p}_{ch} = k_{h\beta} B_{pk}^\beta \hat{f}_r \quad (2.48)$$

where \hat{f}_r is the normalized generator electrical frequency, B_{pk} is the peak flux density, and $k_{h\beta}$, β are hysteresis loss parameters [29]. The eddy current loss density in the core will be approximated as

$$\hat{p}_{ce} = 2\pi \hat{f}_r k_{ef} \int_0^{2\pi} \left(\frac{dB}{d\phi_s} \right)^2 d\phi_s \quad (2.49)$$

where k_{ef} is the eddy current loss parameter given in [29]. Using (2.48) and (2.49), expressions for the hysteresis and eddy current loss densities in stator teeth, $\hat{p}_{ch,st}$ and $\hat{p}_{ce,st}$, respectively, and the hysteresis and eddy current loss densities in stator backiron, $\hat{p}_{ch,sb}$ and $\hat{p}_{ce,sb}$, respectively, can be calculated.

To this end, the total hysteresis loss in machine can be expressed as

$$\hat{P}_h = \hat{p}_{ch,st} \hat{v}_{st} + \hat{p}_{ch,sb} \hat{v}_{sb} \quad (2.50)$$

and the total eddy current loss can be computed using

$$\hat{P}_e = \hat{p}_{ce,st}\hat{v}_{st} + \hat{p}_{ce,sb}\hat{v}_{sb} \quad (2.51)$$

2.2.4 Flux Linkage, Voltage, Torque, Power and Efficiency

This subsection describes design equations for machine flux linkage, electromagnetic torque, power and efficiency [29].

The q - and d - axis magnetizing flux linkages can be expressed as

$$\hat{\lambda}'_{qm} = \hat{r}_{st}\hat{l}(1 - \alpha_{ss}) \int_0^{2\pi} w'_q B_{rstm} d\phi_s \quad (2.52)$$

$$\hat{\lambda}'_{dm} = \hat{r}_{st}\hat{l}(1 - \alpha_{ss}) \int_0^{2\pi} w'_d B_{rstm} d\phi_s \quad (2.53)$$

From [7], the referred line-line peak voltage of the machine terminals can be calculated as

$$v'_{ll,pk} = \sqrt{3} \sqrt{\left(\hat{R}'_s \hat{i}'_{qs} + \hat{\omega}_r \hat{\lambda}'_{dm}\right)^2 + \left(\hat{R}'_s \hat{i}'_{ds} - \hat{\omega}_r \hat{\lambda}'_{qm}\right)^2} \quad (2.54)$$

The electromagnetic torque produced by the machine can be computed using

$$\hat{T}_e = \frac{3P}{4} \left(\hat{\lambda}'_{dm} \hat{i}'_{qs} - \hat{\lambda}'_{qm} \hat{i}'_{ds} \right) \quad (2.55)$$

which, when corrected to include the core losses in machine, is given by

$$\hat{T}_{ec} = \hat{T}_e - \frac{\hat{P}_c P}{4\pi \hat{f}_r} \quad (2.56)$$

where \hat{P}_c is total core loss in the machine.

The electromagnetic specific torque density of the machine is expressed by

$$\rho_{TM} = \frac{|\hat{T}_{ec}|}{\hat{M}_{ge}} \quad (2.57)$$

The total generator losses can be computed as the sum of the resistive and core losses as

$$\hat{P}_{gl} = \hat{P}_h + \hat{P}_e + \hat{P}_r \quad (2.58)$$

The input and output power are computed as

$$\hat{P}_{ing} = -\hat{T}_{ec}\hat{\omega}_{rm} \quad (2.59)$$

and

$$\hat{P}_{outg} = \hat{P}_{ing} - \hat{P}_{gl} \quad (2.60)$$

using which the efficiency of the machine is given by

$$\eta_g = \frac{\hat{P}_{outg}}{\hat{P}_{ing}} \quad (2.61)$$

where in (2.59) $\hat{\omega}_{rm}$ is mechanical speed of the machine.

This completes the design equations required to formulate a metamodel. Details on the formulation and development of these design equations is presented in [29].

2.3 Metamodel Formulation

Based on the design equations presented in previous section, and design assumptions and design constraints presented in [29], multi-objective optimization of normalized generator design is carried out. The design space for the optimization, shown in Table 2.3, is taken from [29]. In Table 2.3, $P_{g,min}$ and $P_{g,max}$ are the minimum and maximum generator power output considered for the metamodel formulation, and $B_{r,smco}$ is the residual flux density of the Sm2C017 R30 magnet material. The design model is optimized for minimum normalized electromagnetic mass and normalized loss using method presented in [29]. Outcome of the multi-objective optimization is Pareto-optimal front of designs, and each design contains information of generator parameters such as dimensions, loss, mass, and circuit parameters. Multiple speeds of the generator are considered in order to construct a model which is speed independent.

From (2.54), it can be observed that d - axis stator flux linkage can be utilized to allow the machine operate at lower line-line terminal voltage, at cost of increased d - axis winding losses. To simplify the analysis and reduce the design space, in this

analysis it is assumed that the DC bus voltage is sufficient so that no stator d - axis current or no rotor flux weakening is required. From this, using (2.9) and (2.10), current angle $\phi_i = \pi$ for the generator operation.

Table 2.3.
Scaled Design Search Space

Parameter	Minimum	Maximum
\hat{r}_{st}	$10^{-2}/P_{max}$	$10/P_{min}$
α_{dm}	10^{-2}	0.3
α_g	10^{-4}	0.2
α_{st}	10^{-2}	1
α_{sb}	10^{-2}	0.5
α_{ss}	$5 \cdot 10^{-2}$	0.95
α_{pm}	$5 \cdot 10^{-2}$	0.95
α_{dol}	0.5	6
B_r^*	$0.5B_{r,smco}$	$B_{r,smco}$
\hat{J}_{rms}	$10^6 P_{min}$	$10^8 P_{max}$
P	2	30

To this end, the function form utilized to represent the information obtained from multi-objective optimization of normalized design model as a continuous function of requirements is given by [29]

$$f_z(\rho_{TM}, \hat{\omega}_{rm}) = \frac{\sum_{i=1}^{N_{zn}} a_{z,i} \rho_{TM}^{n_{zn\rho,i}} \hat{\omega}_{rm}^{n_{zn\omega,i}}}{1 + \sum_{j=1}^{N_{zd}} b_{z,j} \rho_{TM}^{n_{zd\rho,j}} \hat{\omega}_{rm}^{n_{zd\omega,j}}} \quad (2.62)$$

where ‘ z ’ represents a variable being interpolated. For a given ‘ z ’ term, the number of numerator and denominator terms, N_{zn} and N_{zd} , numerator and denominator exponents $n_{zn\rho,i}$, $n_{zn\omega,i}$, $n_{zd\rho,j}$, $n_{zd\omega,j}$ and finally numerator and denominator coefficients

$a_{z,i}$ $b_{z,j}$ are constants which are found by curve fitting techniques so that (2.62) best fits the normalized design data. For the generator metamodel,

$$z \in \{\hat{M}_{ge}, \hat{V}_{ge}, \hat{J}_{rms}, \hat{P}_r, \hat{P}_h, \hat{P}_e, v'_{llpk}, \hat{R}'_s, \hat{L}'_q, \hat{L}'_d, \hat{\lambda}'_m, P, \alpha_{dol}\} \quad (2.63)$$

To do this, normalized designs are conducted for a number of values of $\hat{\omega}_{rm}$. The specific torque density and normalized speed hence become the two variables about which the metamodel is based.

In this work, it is considered that the required generator power requirement is between 0.5-5 MW operating at speed between 1000 and 8000 RPM. The normalized design process is run at 8 corresponding logarithmically distributed normalized speed covering this range. Thus the normalized speed range is $[0.0026, 0.0068, \dots, 2.0944] \times 10^{16}$. Figs. 2.4-2.14 illustrate scaled properties vs metamodel fit. In each case, there are eight sets of data, one for each normalized speed. In Figs. 2.4-2.14, U_D is the unit of the considered base D which is Watt.

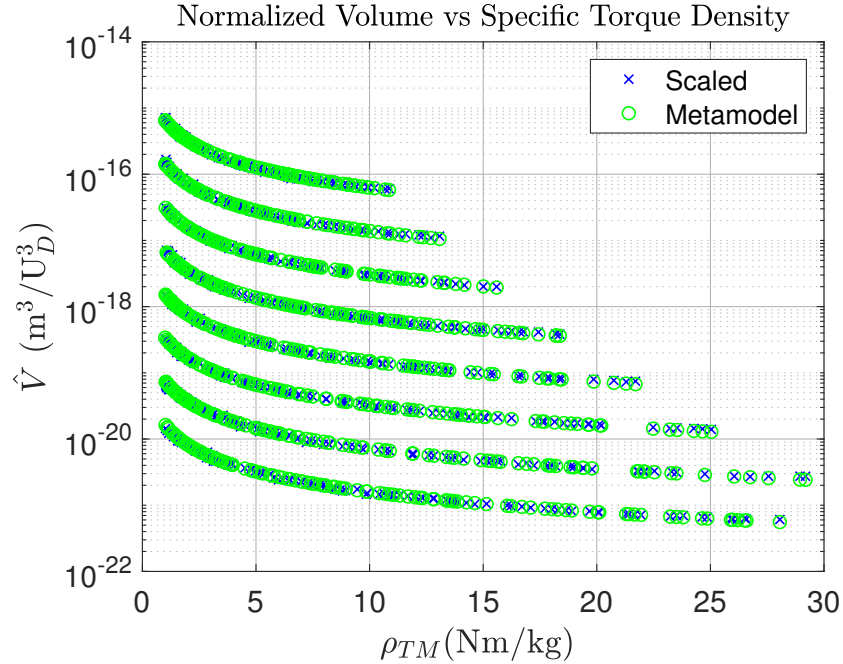


Fig. 2.4. Normalized Electromagnetic Volume vs Specific Torque Density

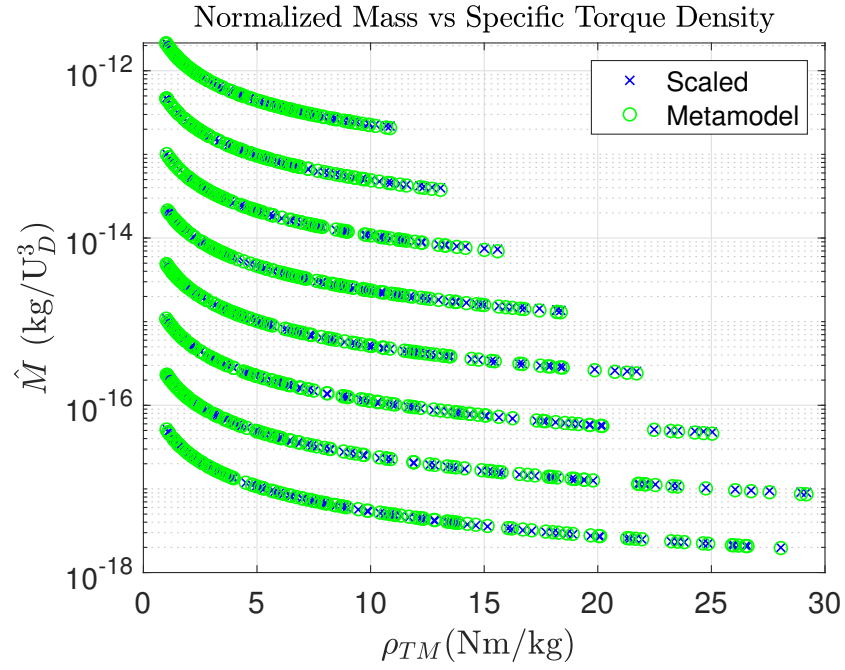


Fig. 2.5. Normalized Electromagnetic Mass vs Specific Torque Density

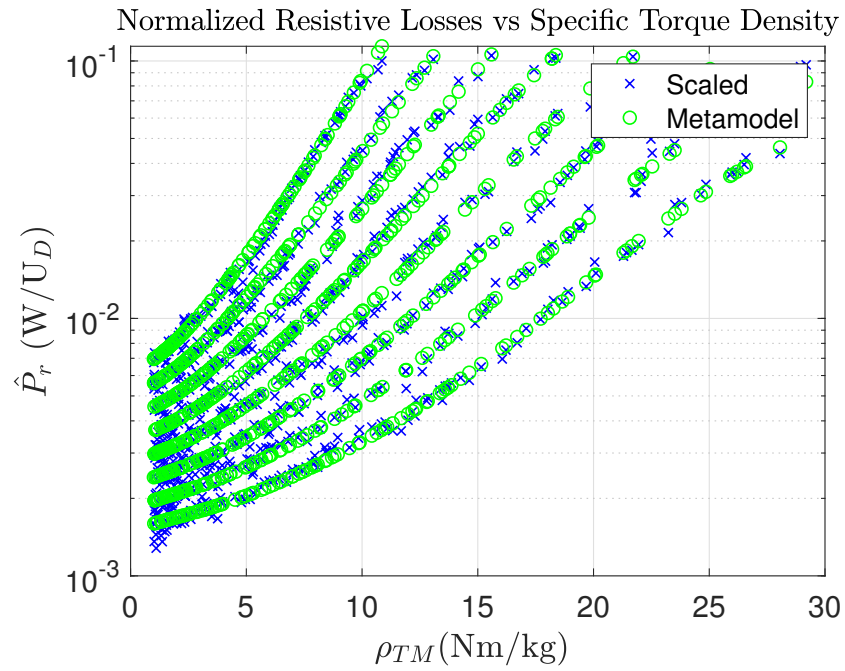


Fig. 2.6. Normalized Resistive Loss vs Specific Torque Density

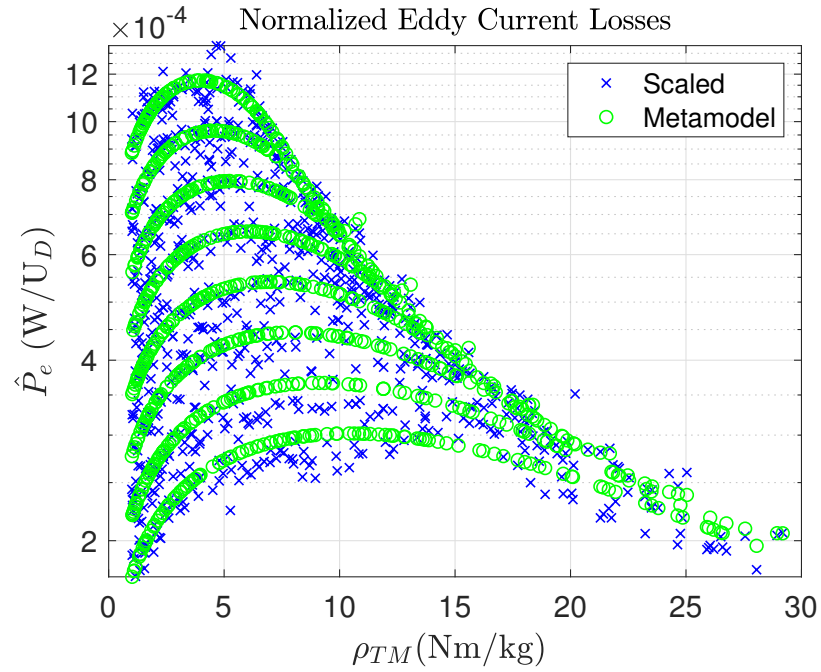


Fig. 2.7. Normalized Eddy Current loss vs Specific Torque Density

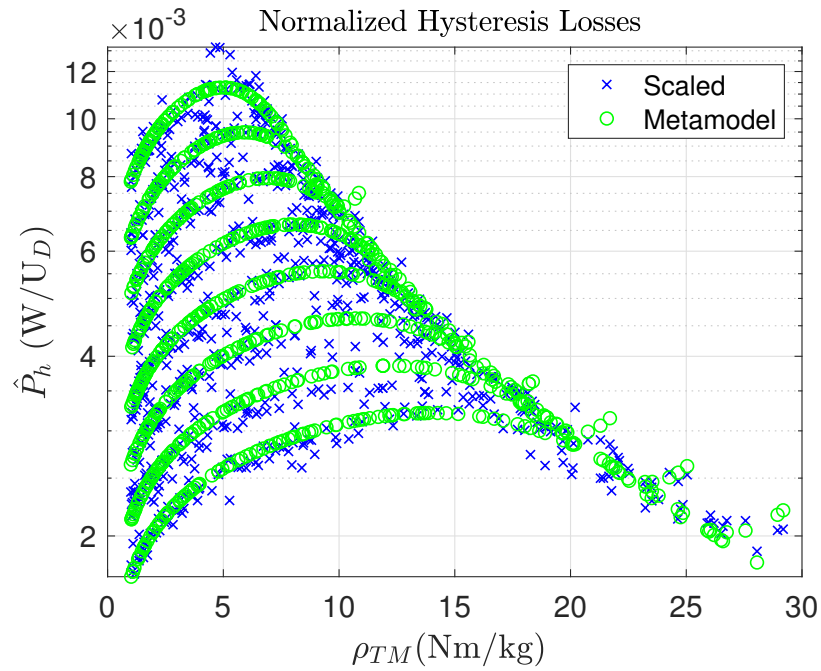


Fig. 2.8. Normalized Hysteresis Loss vs Specific Torque Density

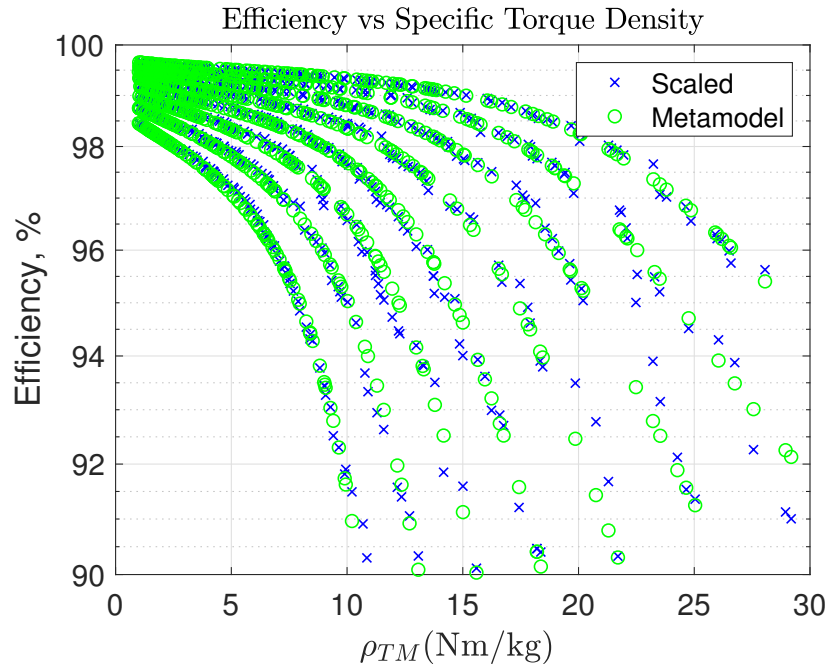


Fig. 2.9. Generator Efficiency vs Specific Torque Density

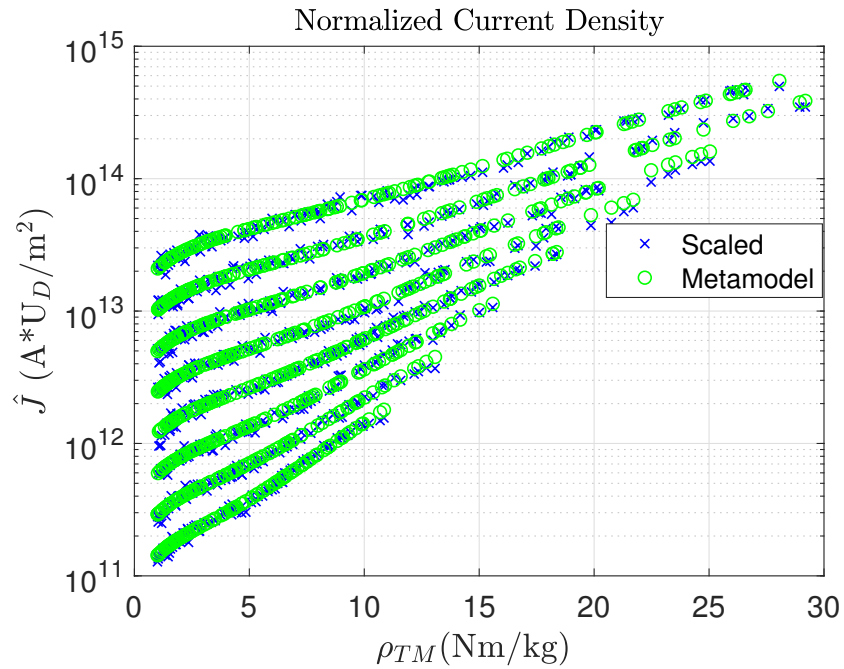


Fig. 2.10. Normalized Current Density vs Specific Torque Density

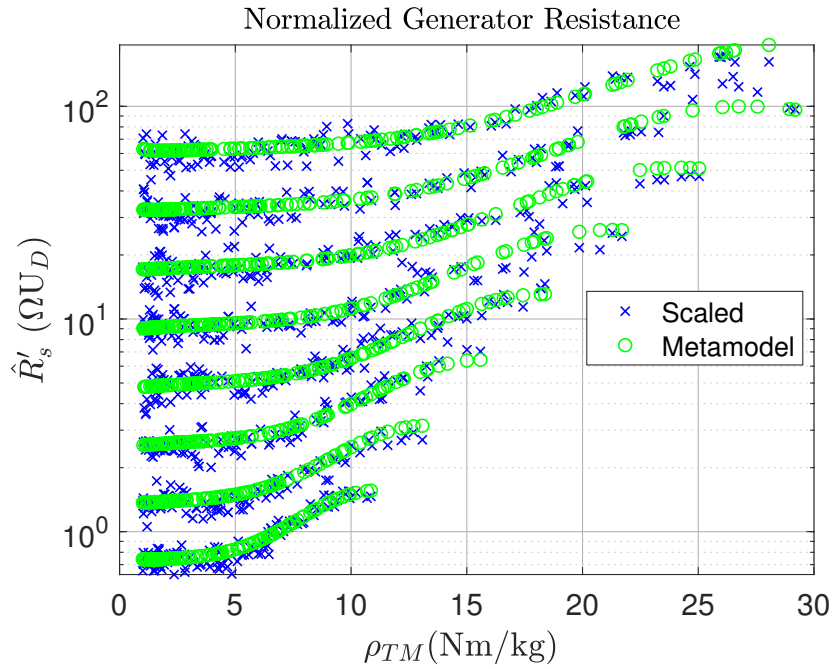
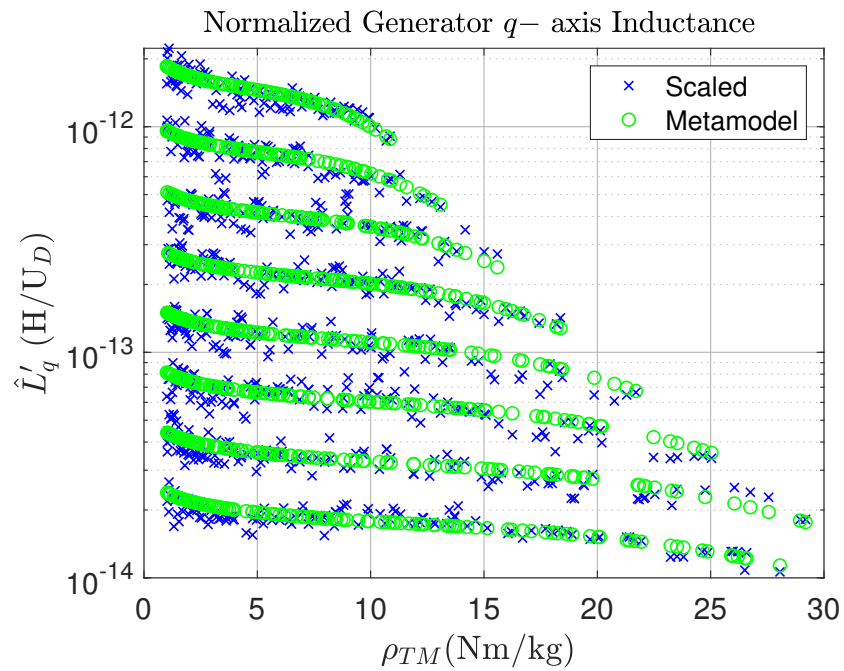


Fig. 2.11. Normalized Resistance vs Specific Torque Density

Fig. 2.12. Normalized q -axis Inductance vs Specific Torque Density

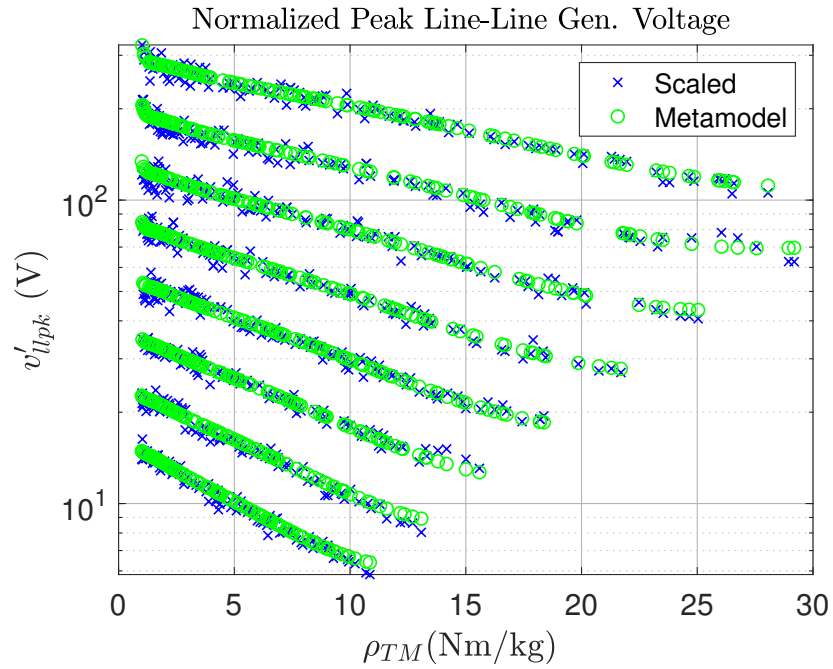
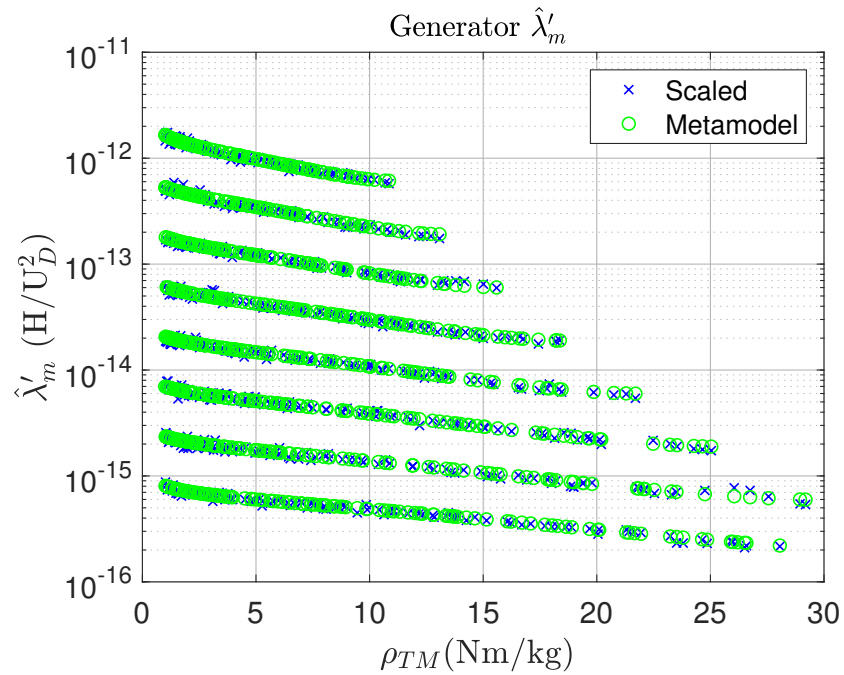


Fig. 2.13. Referred Machine Terminal Line-line Voltage

Fig. 2.14. Normalized Machine λ_m vs Specific Torque Density

Due to inexact fitting, the difference between metamodel and scaled data exists. However, in general the fit is reasonable. For example, considering efficiency, 97% of metamodel predictions are within 0.5% of the scaled data. The metamodel parameters are presented in [31].

2.4 Metamodel Usage

As presented in [29], to use the metamodel, the user first specifies the normalization base, which is the specification of generator power output P_{go} . The user also specifies the generator mechanical rated speed w_{rm} . With the speed information, using (2.62), quantities listed in (2.63) can be calculated for a specified range of specific torque density (taken between 1 - 20 Nm/kg in this work). Next, using specified P_{go} , and Table 2.1, the normalized generator quantities can be calculated as function of specific torque density. However, calculation of referred quantities in Table 2.2 still requires N_{s1} , and the referred quantities need to be moved back to non-referred values so as to consider the interaction between generator and rectifier.

To this end, the value of N_{s1} can be estimated using Table 2.2, equation (2.54) and peak-peak line voltage at MMC AC terminals. For the MMC, the peak fundamental line-line AC voltage for unit duty cycle, ignoring harmonic components in voltage, can be calculated as [6]

$$v_{llpk,mmc} \approx \max \left(\frac{V_{dc}}{2} + \frac{V_{dc}}{2} \cos(\theta_r + \delta_{mmc}) - \frac{V_{dc}}{2} - \frac{V_{dc}}{2} \cos \left(\theta_r - \frac{2\pi}{3} + \delta_{mmc} \right) \right) \quad (2.64)$$

which simplifies to

$$v_{llpk,mmc} \approx \frac{\sqrt{3}}{2} V_{dc} \quad (2.65)$$

where V_{dc} is the DC bus voltage and δ_{mmc} is the MMC voltage phase angle relative to machine q - axis.

From (2.54) and (2.65), the generator terminal voltage and DC bus voltage can be related as

$$N_{s1} v'_{llpk} \leq \frac{\sqrt{3}}{2} V_{dc} \quad (2.66)$$

leading to

$$N_{s1} \leq \frac{\sqrt{3}V_{dc}}{2v'_{llpk}} \quad (2.67)$$

in order for the assumption of sufficient DC bus voltage to be valid. Recall that v'_{llpk} can be calculated using (2.62).

Note that the calculation in (2.64) does not consider the harmonic components in the MMC arm voltages. A higher harmonic content in arm voltage could lead to lower DC bus voltage available to the generator. Hence, selecting maximum value for N_{s1} may not be practical. Also, a low value of N_{s1} leads to high generator current as it increases inversely with N_{s1} for a given value of referred current (see Table 2.2). Though generator resistive losses are unaffected (as the actual resistance decreases proportional to N_{s1}^2 , see Table 2.2 and (2.20)), the MMC resistive loss will increase. Hence a very low N_{s1} is not desired, and a suitable value of N_{s1} needs to be considered. In this work, N_{s1} is taken as

$$N_{s1} = \alpha_{ns1} \frac{\sqrt{3}V_{dc}}{2v'_{llpk}} \quad (2.68)$$

where $\alpha_{ns1} \in [0.5, 1]$ is taken as a design parameter. Using α_{ns1} , the formulated design equations, metamodel, and Table 2.2, the machine parameters can be calculated.

As an example, a generator supplying P_{go} 1 MW at 3600 rpm tied to a 5 kV DC bus is considered with α_{ns1} equal to 0.85. The parameters are calculated using the metamodel as a function of specific torque density as shown in Fig. 2.15-2.26. As discussed, the metamodel data does not consider the structural or case mass/volume/length, and only presents the electromagnetic values. Using the calculated machine dimensions and speed, tip speed of the rotor surface is calculated as shown in Fig. 2.26. A constraint is imposed on the tip speed during metamodel usage to achieve viable designs. Details on validation of the metamodel with a detailed electric machine design model is presented in [29].

This completes the formulation of metamodel of PMAC generator. This metamodel will be utilized in next chapters to include the interaction between generator and rectifier, and formulate a multi-objective design paradigm for the considered PMAC-MMC system. Details on formulation and validation is presented in [29].

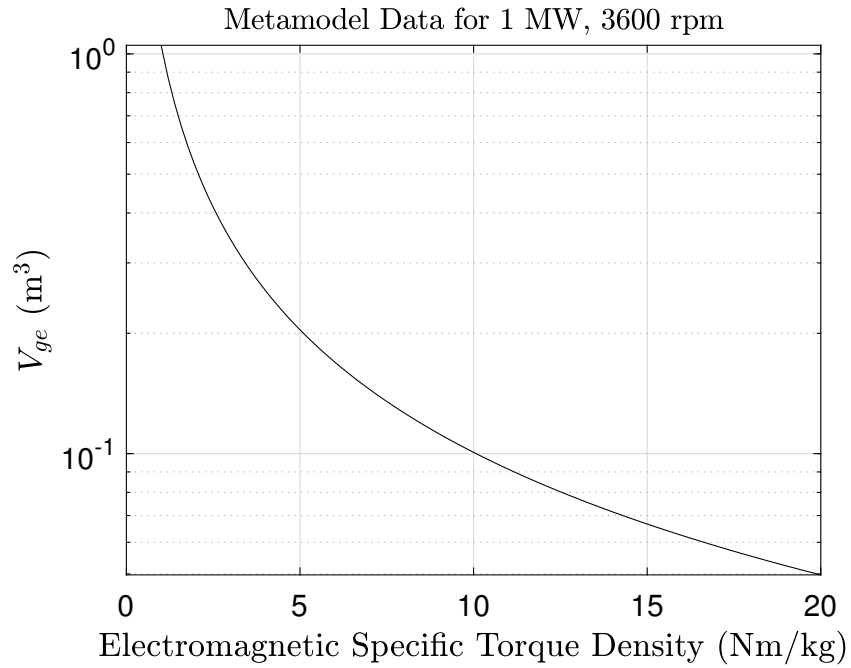


Fig. 2.15. Electromagnetic Volume vs Specific Torque Density

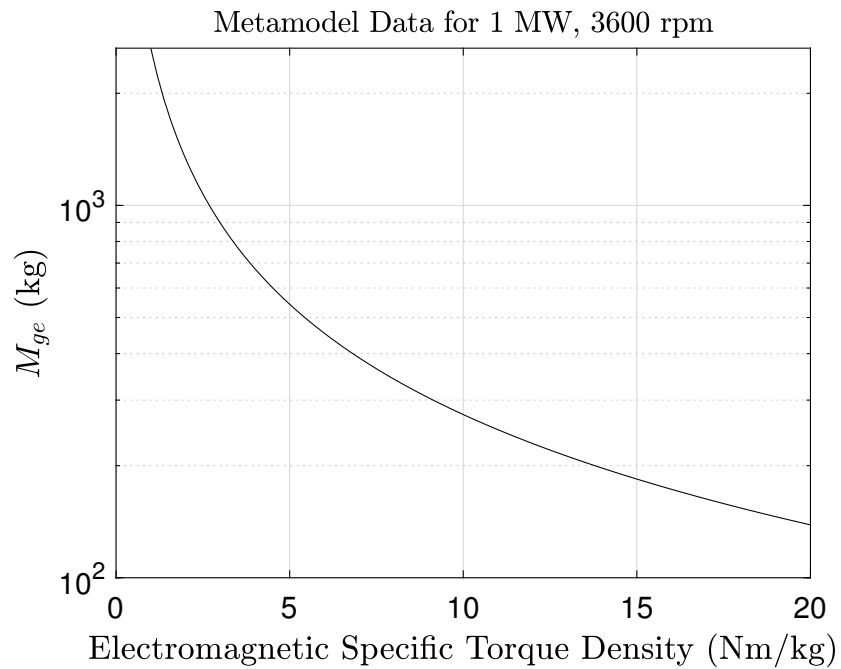


Fig. 2.16. Electromagnetic Mass vs Specific Torque Density

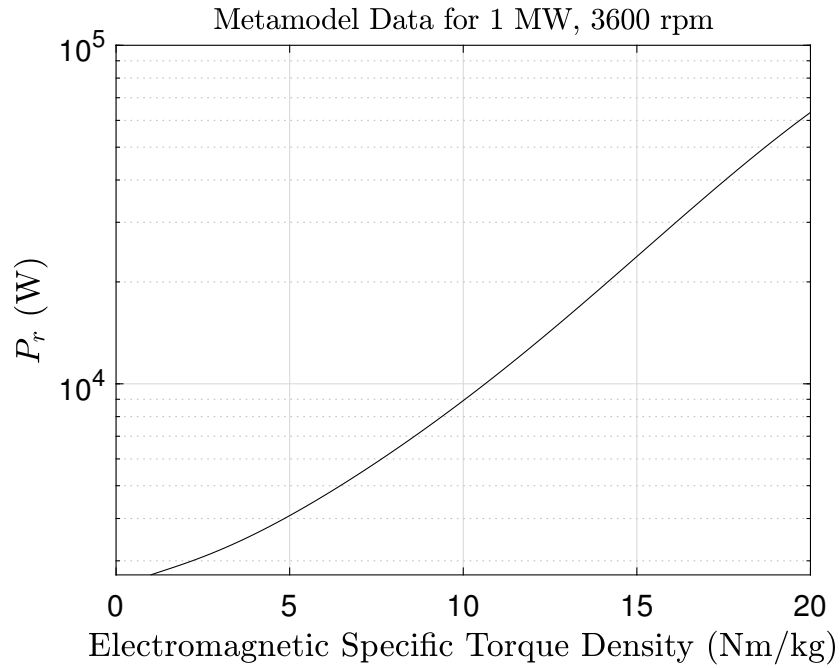


Fig. 2.17. Resistive Loss vs Specific Torque Density

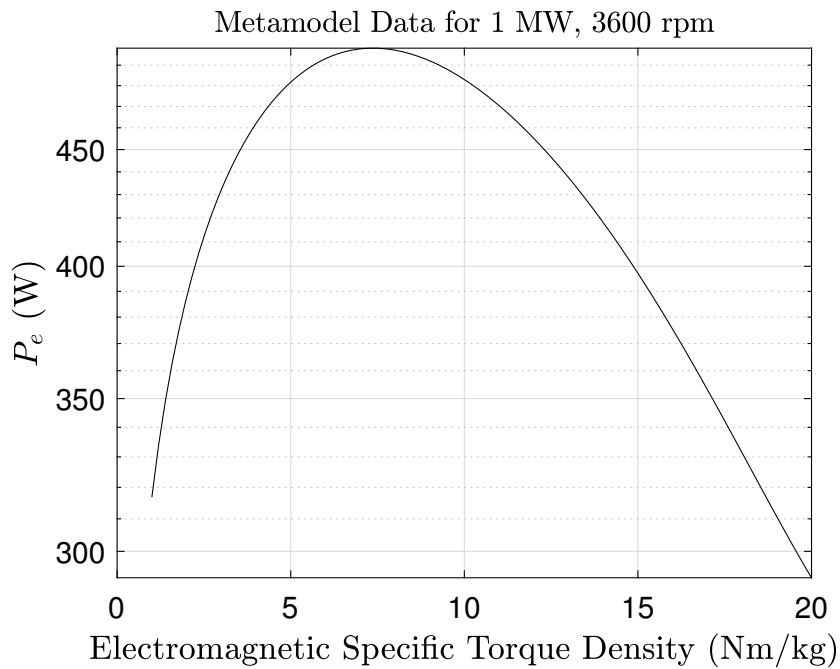


Fig. 2.18. Eddy Current Loss vs Specific Torque Density

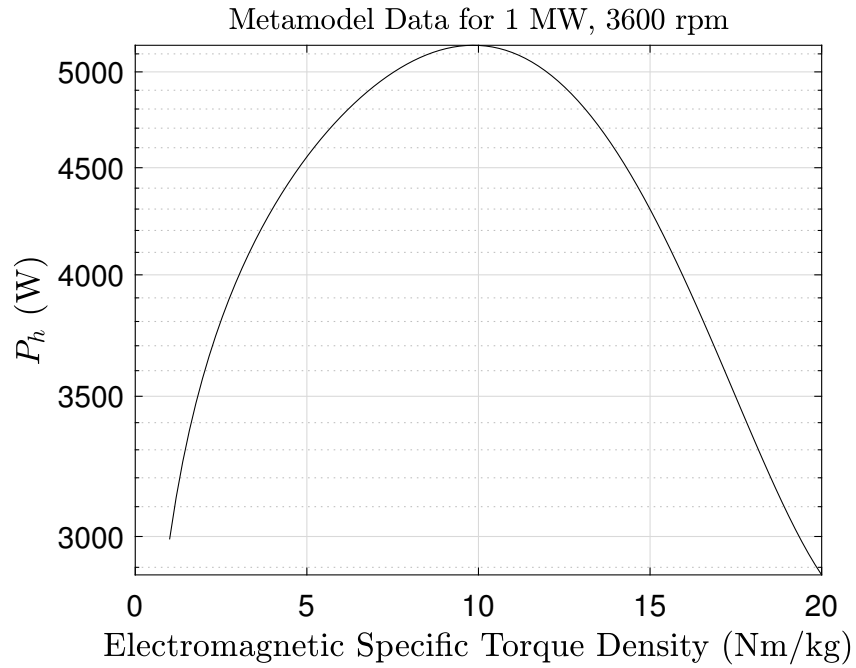


Fig. 2.19. Hysteresis Loss vs Specific Torque Density

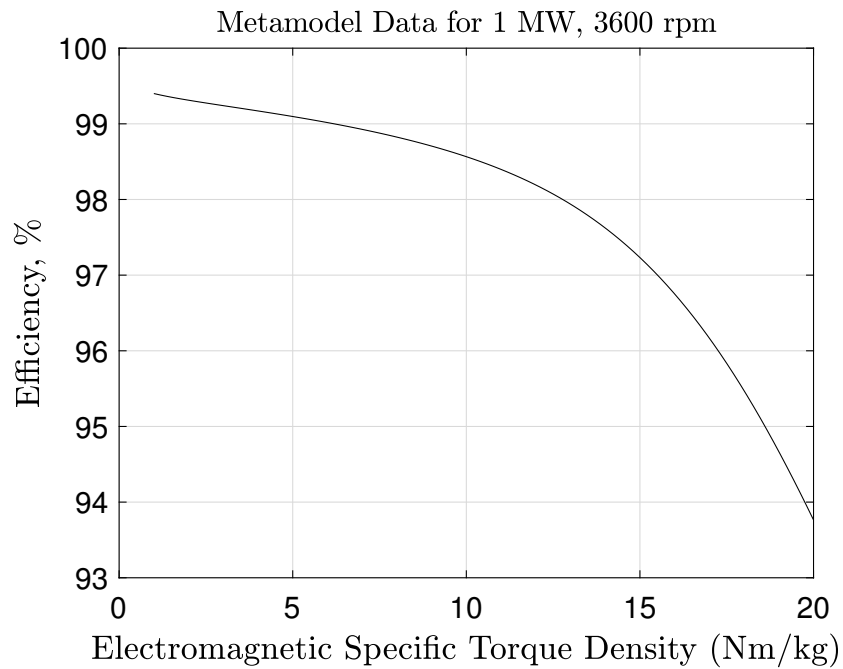


Fig. 2.20. Generator Efficiency vs Specific Torque Density

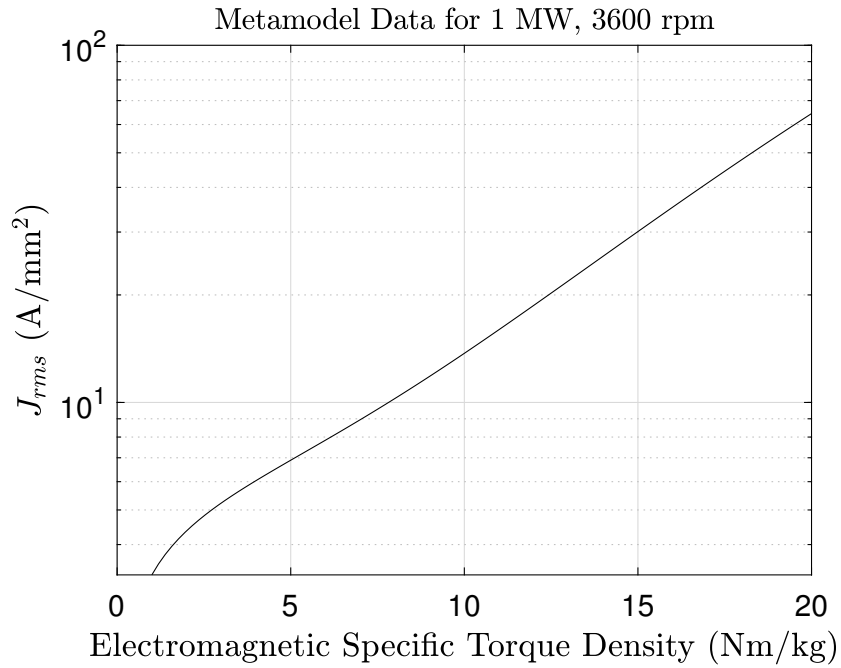


Fig. 2.21. Current Density vs Specific Torque Density

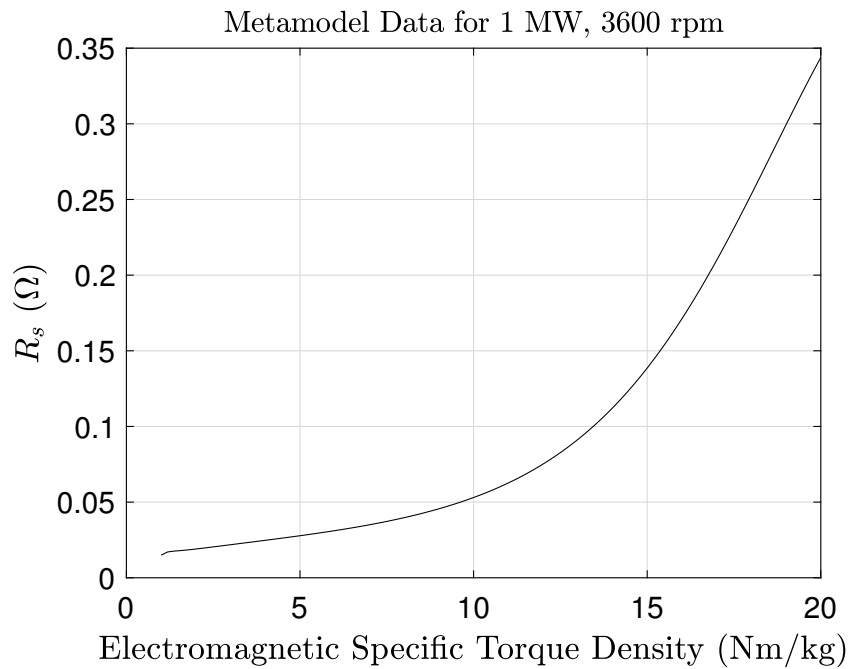


Fig. 2.22. Resistance vs Specific Torque Density

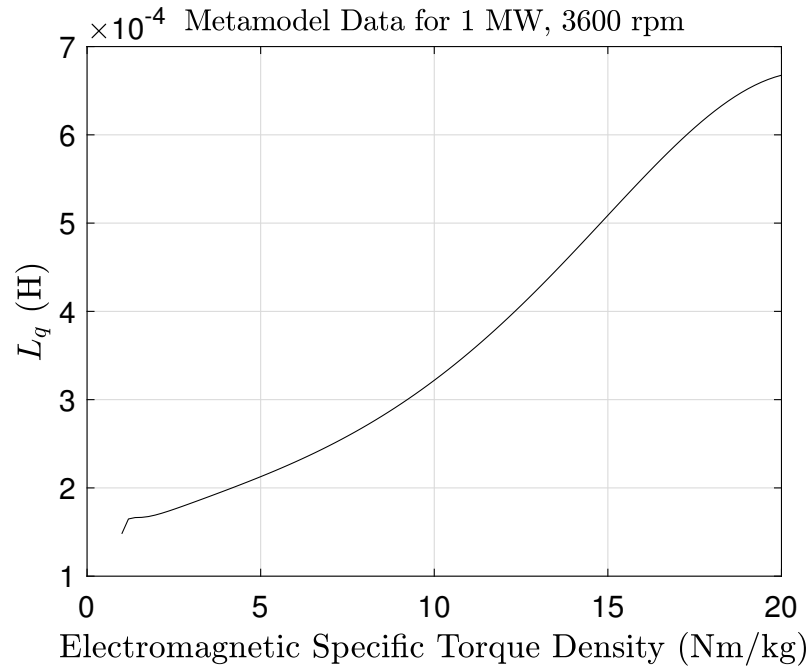


Fig. 2.23. Machine q -axis Inductance vs Specific Torque Density

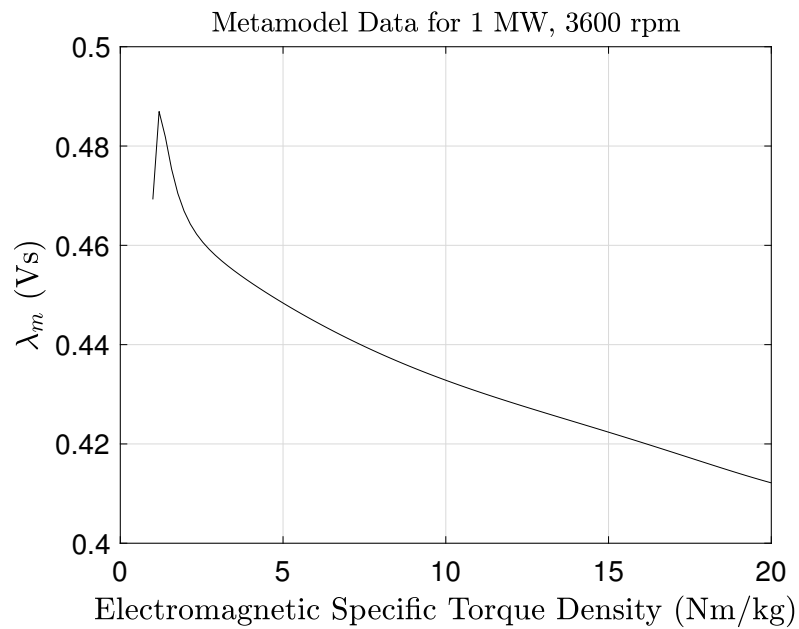


Fig. 2.24. Machine λ_m vs Specific Torque Density

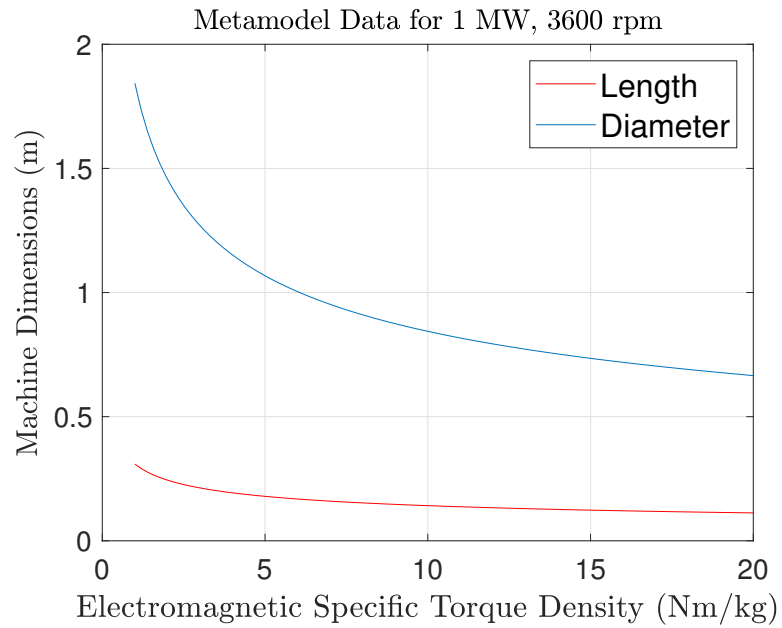


Fig. 2.25. Generator Dimensions vs Specific Torque Density

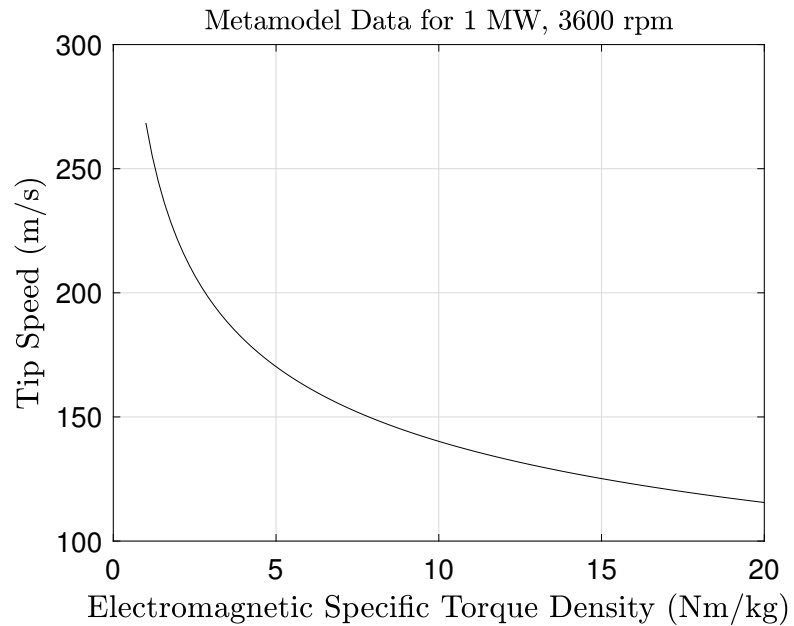


Fig. 2.26. Generator Rotor Tip Speed vs Specific Torque Density

3. WAVEFORM-LEVEL MODEL OF PMAC-MMC SYSTEM

In this chapter, a waveform-level model of the generator-rectifier system shown in Fig. 3.1 is set forth. This simulation model will be used for the development and verification of the proposed high-speed simulation model in Chapter 4. The detailed system diagram is shown in Fig. 3.1 along with the submodule topology in Fig. 3.2.

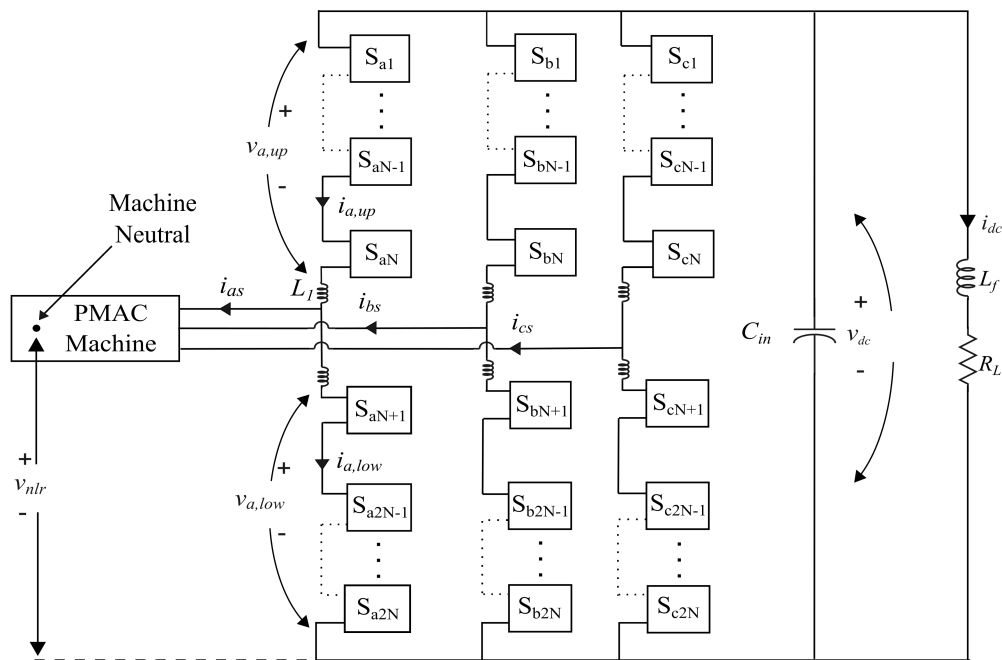


Fig. 3.1. Modular Multilevel Converter

As mentioned earlier, each arm contains N submodules and a filter inductor. For the purpose of development of the waveform-level model, each submodule switch is represented using an ideal switch with forward switch voltage drop $V_{sw, fw}$ and resistance $R_{sw, fw}$. Similarly, the forward biased diode is modeled as an ideal diode

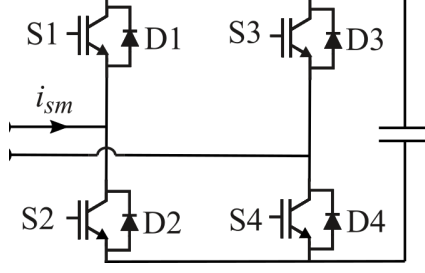


Fig. 3.2. H-bridge Converter based Submodule Topology

with forward voltage drop $V_{d,fw}$ and resistance $R_{d,fw}$. Any time delay in switching is neglected. Switching losses are not included in this model.

3.1 Variable definitions

The first step in developing a waveform-level model is to define system variables. To this end, $\mathbf{v}_{x,cap,up}$ is defined as vector containing the x -phase upper arm submodule voltages, where $x \in \{‘a’, ‘b’, ‘c’\}$. That is

$$\mathbf{v}_{x,cap,up} = \left[v_{1,x,cap,up} \quad v_{2,x,cap,up} \quad \cdots \quad v_{i,x,cap,up} \quad \cdots \quad v_{N,x,cap,up} \right]^T \quad (3.1)$$

where $i \in \{1, 2, \dots, N\}$ is submodule index and $v_{i,x,cap,up}$ is the x -phase upper arm submodule i capacitor voltage. Similarly, for the lower arm

$$\mathbf{v}_{x,cap,low} = \left[v_{1,x,cap,low} \quad v_{2,x,cap,low} \quad \cdots \quad v_{j,x,cap,low} \quad \cdots \quad v_{N,x,cap,low} \right]^T \quad (3.2)$$

where $j \in \{1, 2, \dots, N\}$ is submodule index and $v_{j,x,cap,up}$ is the x -phase lower arm submodule j capacitor voltage. The voltage between the machine neutral and lower rail of the MMC is v_{nlr} . The voltage across the x -phase of machine terminals to the machine neutral is denoted v_{xs} . The current going into the x -phase of machine is denoted i_{xs} . For the MMC, $v_{x,up}$ is defined as total voltage across the submodules in upper arm of x -phase. Similarly $v_{x,low}$ is defined as total voltage across the submodules in the x -phase lower arm as shown in Fig. 3.1. The voltage across submodule i in upper arm is defined as $v_{i,x,up}$ and is calculated as sum of capacitor voltage and switch

drops. Similarly, $v_{j,x,low}$ is defined as the x -phase voltage across submodule j in the lower arm. In the MMC arms, $i_{x,up}$ is defined as current in upper arm whereas $i_{x,low}$ is defined as current in lower arm. At the load end, v_{dc} is defined as the instantaneous voltage across the DC bus capacitor and i_{dc} is defined as the load current.

For the i^{th} submodule in the upper arm, $s_{i,x,up}$ denotes the switching signal for the submodule, and it can take on values of 0 or 1. A zero value of $s_{i,x,up}$ means that the submodule capacitor is bypassed whereas value equal to 1 denotes positive turn-on of the submodule with $+v_{i,x,cap,up}$ voltage at submodule terminals. The negative state is not utilized. The vector $\mathbf{s}_{x,up}$ contains switching signal for each submodule in upper arm. In particular

$$\mathbf{s}_{x,up} = \begin{bmatrix} s_{1,x,up} & s_{2,x,up} & \cdots & s_{i,x,up} & \cdots & s_{N,x,up} \end{bmatrix}^T \quad (3.3)$$

Similarly, for lower arm $s_{i,x,low}$ can be defined. Hence, $\mathbf{s}_{x,low}$ is given by

$$\mathbf{s}_{x,low} = \begin{bmatrix} s_{1,x,low} & s_{2,x,low} & \cdots & s_{i,x,low} & \cdots & s_{N,x,low} \end{bmatrix}^T \quad (3.4)$$

3.2 Reference frame transformation

It will be convenient to define transformation matrix \mathbf{K}_s , which transforms abc variables to an arbitrary reference frame. From [32]

$$\mathbf{f}_{qd0} = \mathbf{K}_s \mathbf{f}_{abc} \quad (3.5)$$

where

$$\mathbf{f}_{qd0} = \begin{bmatrix} f_q & f_d & f_0 \end{bmatrix}^T \quad (3.6)$$

$$\mathbf{f}_{abc} = \begin{bmatrix} f_a & f_b & f_c \end{bmatrix}^T \quad (3.7)$$

$$\mathbf{K}_s = \frac{2}{3} \begin{bmatrix} \cos(\theta) & \cos\left(\theta - \frac{2\pi}{3}\right) & \cos\left(\theta + \frac{2\pi}{3}\right) \\ \sin(\theta) & \sin\left(\theta - \frac{2\pi}{3}\right) & \sin\left(\theta + \frac{2\pi}{3}\right) \\ \frac{1}{2} & \frac{1}{2} & \frac{1}{2} \end{bmatrix} \quad (3.8)$$

and θ is the position of the arbitrary reference frame. The speed of the reference frame is denoted as $\omega = d\theta/dt$ in rad/s. In (3.5)-(3.7), \mathbf{f} may be current or voltage

variables in the system. For example, the machine currents in $qd0$ variables, \mathbf{i}_{qd0s} , may be expressed

$$\mathbf{i}_{qd0s} = \mathbf{K}_s \mathbf{i}_{abc} \quad (3.9)$$

3.3 Generator rectifier model

This section develops the dynamic equations for the PMAC-MMC system. From Fig. 3.1

$$i_{xs} = i_{x,up} - i_{x,low} \quad (3.10)$$

where $x \in \{‘a’, ‘b’, ‘c’\}$. It will be convenient to define x - phase total current $i_{x,ul}$ as

$$i_{x,ul} = i_{x,up} + i_{x,low} \quad (3.11)$$

Using (3.11), circulatory current $i_{x,circ}$ is defined as

$$i_{x,circ} = i_{x,ul}/2 \quad (3.12)$$

From Kirchhoff’s current law

$$i_{a,up} + i_{b,up} + i_{c,up} = i_{a,low} + i_{b,low} + i_{c,low} \quad (3.13)$$

The capacitor voltage of each submodule in upper arm is governed by

$$pv_{i,x,cap,up} = s_{i,x,up} i_{x,up} / C_{sm} \quad (3.14)$$

where p is the time derivative operator. Similarly, for lower arm

$$pv_{i,x,cap,low} = s_{i,x,low} i_{x,low} / C_{sm} \quad (3.15)$$

Assuming a symmetrical 3-phase inductor, from Kirchhoff’s voltage law

$$\begin{bmatrix} L_{s,i} & L_{m,i} & L_{m,i} \\ L_{m,i} & L_{s,i} & L_{m,i} \\ L_{m,i} & L_{m,i} & L_{s,i} \end{bmatrix} \mathbf{p}\mathbf{i}_{abc,ul} = \begin{bmatrix} v_{dc} \\ v_{dc} \\ v_{dc} \end{bmatrix} - (\mathbf{v}_{abc,up} + \mathbf{v}_{abc,low} + R_i \mathbf{i}_{abc,ul}) \quad (3.16)$$

where $L_{s,i}$ and $L_{m,i}$ are the self inductance and mutual inductance between phases of the inductor, respectively, and R_i is the inductor winding resistance. Again, from Kirchoff's voltage law, the machine voltage can be expressed as

$$\mathbf{v}_{abc s} = -R_i \mathbf{i}_{abc,up} - \mathbf{L}_1 \mathbf{p} \mathbf{i}_{abc,up} - \mathbf{v}_{abc,up} + (v_{dc} - v_{nlr}) \begin{bmatrix} 1 & 1 & 1 \end{bmatrix}^T \quad (3.17)$$

Similarly, machine voltage in terms of lower arm quantities can be expressed as

$$\mathbf{v}_{abc s} = +R_i \mathbf{i}_{abc,low} + \mathbf{L}_1 \mathbf{p} \mathbf{i}_{abc,low} + \mathbf{v}_{abc,low} - v_{nlr} \begin{bmatrix} 1 & 1 & 1 \end{bmatrix}^T \quad (3.18)$$

Combining (3.17) and (3.18) yields

$$\mathbf{v}_{abc s} = -\frac{R_i}{2} \mathbf{i}_{abc s} - \frac{1}{2} \mathbf{L}_1 \mathbf{p} \mathbf{i}_{abc s} - \frac{1}{2} (\mathbf{v}_{abc,up} - \mathbf{v}_{abc,low}) + \left(\frac{v_{dc}}{2} - v_{nlr} \right) \begin{bmatrix} 1 & 1 & 1 \end{bmatrix}^T \quad (3.19)$$

It should be noted that machine neutral is not connected so if parasitic connections are ignored, zero sequence current cannot flow into the machine terminals.

Using the variable transformation defined in (3.5), (3.19) can be expressed as

$$\mathbf{v}_{qd0s} = -\frac{R_i}{2} \mathbf{i}_{qd0s} - \frac{1}{2} \begin{bmatrix} L_{q,i} & 0 & 0 \\ 0 & L_{d,i} & 0 \\ 0 & 0 & L_{0,i} \end{bmatrix} \mathbf{p} \mathbf{i}_{qd0s} - \frac{\omega}{2} \begin{bmatrix} L_{d,i} i_{ds} \\ -L_{q,i} i_{qs} \\ 0 \end{bmatrix} - \frac{1}{2} (\mathbf{v}_{qd0,up} - \mathbf{v}_{qd0,low}) + \begin{bmatrix} 0 & 0 & (\frac{v_{dc}}{2} - v_{nlr}) \end{bmatrix}^T \quad (3.20)$$

where

$$L_{q,i} = L_{d,i} = L_{s,i} - L_{m,i} \quad (3.21)$$

$$L_{0,i} = L_{s,i} + 2L_{m,i} \quad (3.22)$$

and where \mathbf{v}_{qd0s} , $\mathbf{v}_{qd0,up}$ and $\mathbf{v}_{qd0,low}$ are $qd0$ voltages, and \mathbf{i}_{qd0s} is the $qd0$ machine current.

The analysis presented above is expressed in the arbitrary reference frame and is independent of machine equations. For the PMAC machine, the rotor reference frame is chosen. Machine equations in rotor reference frame can be written as [32]

$$\mathbf{v}_{qd0s}^r = R_s \mathbf{i}_{qd0s}^r + \begin{bmatrix} L_q & 0 & 0 \\ 0 & L_d & 0 \\ 0 & 0 & L_0 \end{bmatrix} \mathbf{p} \mathbf{i}_{qd0s}^r + \omega_r \begin{bmatrix} L_d i_{ds}^r + \lambda_m \\ -L_q i_{qs}^r \\ 0 \end{bmatrix} \quad (3.23)$$

where R_s is the machine resistance, L_q , L_d and L_0 are the q -axis, d -axis and 0-sequence inductances, respectively, λ_m is the amplitude of the flux linkage due to the permanent magnet as viewed from stator winding, and ω_r is the electrical rotor speed. Converting (3.20) to rotor reference frame, equating it to (3.23), and manipulating, the time derivative of the machine currents can be expressed as

$$p i_{qs}^r = \frac{1}{L_{q,eq}} \left(-R_{eq} i_{qs}^r - \omega_r \lambda_m - \omega_r L_{d,eq} i_{ds}^r - \frac{1}{2} (v_{q,up}^r - v_{q,low}^r) \right) \quad (3.24)$$

$$p i_{ds}^r = \frac{1}{L_{d,eq}} \left(-R_{eq} i_{ds}^r + \omega_r L_{q,eq} i_{qs}^r - \frac{1}{2} (v_{d,up}^r - v_{d,low}^r) \right) \quad (3.25)$$

$$p i_{0s}^r = \frac{1}{L_{0,eq}} \left(-R_{eq} i_{0s}^r - \frac{1}{2} (v_{0,up}^r - v_{0,low}^r) + \frac{v_{dc}}{2} - v_{nlr} \right) = 0 \quad (3.26)$$

where

$$R_{eq} = R_s + \frac{R_i}{2} \quad (3.27)$$

$$L_{q,eq} = L_q + \frac{L_{q,i}}{2} \quad (3.28)$$

$$L_{d,eq} = L_d + \frac{L_{d,i}}{2} \quad (3.29)$$

$$L_{0,eq} = L_0 + \frac{L_{0,i}}{2} \quad (3.30)$$

The time derivative of the current through load resistance R_L can be expressed

$$p i_{dc} = \frac{v_{dc} - R_L i_{dc}}{L_f} \quad (3.31)$$

Finally, the DC bus voltage is governed by

$$p v_{dc} = \frac{1}{C_{in}} \left(-i_{dc} - \sum_{x \in \{ 'a', 'b', 'c' \}} \frac{i_{x,ul}}{2} \right) \quad (3.32)$$

3.4 Control Scheme

It will be convenient to define $qd0$ converter voltages in the rotor reference frame as the voltage source term in (3.24)-(3.26). In particular,

$$\mathbf{v}_{qd0,conv}^r = -\frac{1}{2} (\mathbf{v}_{qd0,up}^r - \mathbf{v}_{qd0,low}^r) \quad (3.33)$$

Using (3.5), the converter voltage in abc variables, $\mathbf{v}_{abc,conv}$, can be defined as

$$\mathbf{v}_{abc,conv} = \mathbf{K}_s^{-1} \mathbf{v}_{qd0,conv}^r \quad (3.34)$$

Control diagrams for the MMC control system are shown in Figures 3.3, 3.4 and 3.5. Fig. 3.3 shows the DC bus voltage control which controls the DC bus voltage to a commanded value of V_{dc}^* [33]. In the DC voltage control, a reference DC current i_{dc}^* is generated using the PI controller. The actual DC current is fed-forward for improved control performance. Using i_{dc}^* , and power balance between generator and DC load, and neglecting losses, the reference q - axis current command i_{qs}^{r**} is generated. A current reference limit is imposed on the controller to limit the maximum absolute value of the commanded current to i_{pklim} . The output of the controller is i_{qs}^{r*} . The difference between i_{qs}^{r**} and i_{qs}^{r*} is multiplied by the anti wind-up gain and fed back so the wind up is limited. As discussed earlier, assuming sufficient DC bus voltage, the d - axis current is commanded to be zero.

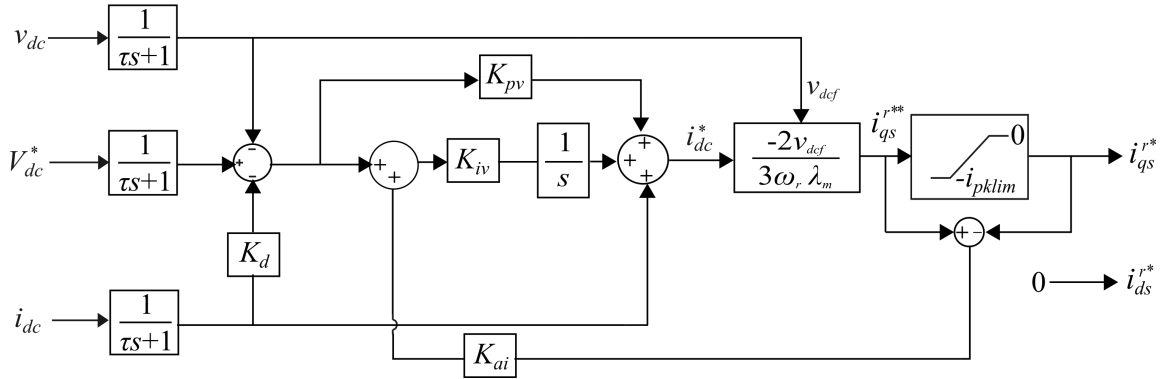


Fig. 3.3. DC Bus Voltage Control

The output of the DC bus voltage control (that is the commanded q - and d - axis machine currents) is supplied to the q - and d - axis machine current control system which generates the MMC AC output voltage reference $\mathbf{v}_{abc,conv}^*$ as shown in Fig

3.4 [34]. The reference q - and d - axis currents are inputs to a using PI and feed-forward control to generate q - and d - axis converter voltage, as defined in (3.33). Next, the inverse transformation from (3.34) is utilized to convert the q - and d - axis quantities to abc variables.

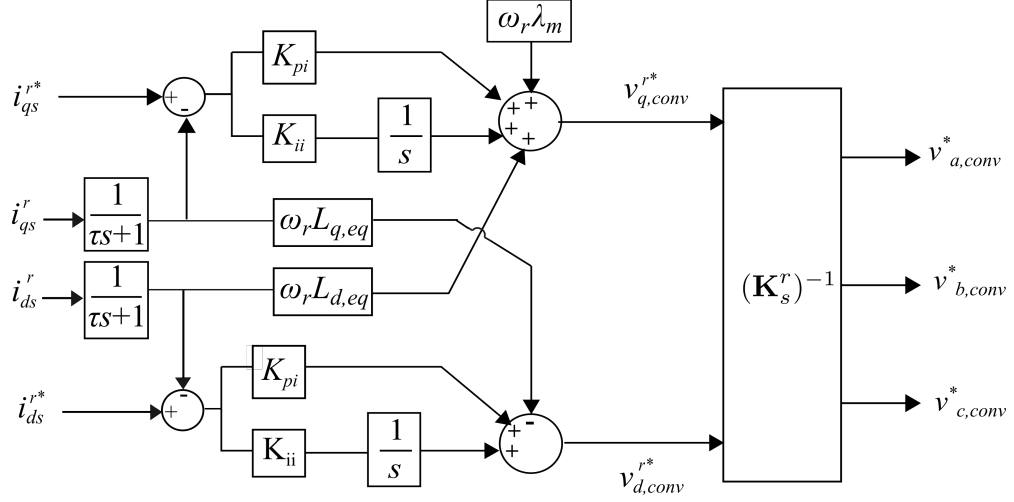


Fig. 3.4. Machine q - and d - axis Current Control

In MMCs, a second harmonic circulatory component of arm current exists as discussed in [6, 34, 35]. It is generated due to the interaction of the fundamental component of the duty cycle with the fundamental component of the submodule capacitor voltage and the DC component of duty cycle with the second harmonic component of submodule capacitor voltage. Fig. 3.5 shows the control system employed for second harmonic current elimination in the MMC arm current [35]. As shown, the reference value of the circulatory component of current, defined in (3.12), is set to zero. A reference frame rotating at double the frequency of fundamental component is utilized to eliminate the second harmonic current ripple by adding an appropriate second harmonic common mode reference voltage $-v_{2x,conv}^*$ to each arm of x -phase.

To this end, the duty cycle for upper arm, $d_{x,up}$ is defined as

$$d_{x,up} = \frac{1}{2} - \frac{v_{x,conv}^*}{V_{dc}^*} - \frac{v_{2x,conv}^*}{V_{dc}^*} \quad (3.35)$$

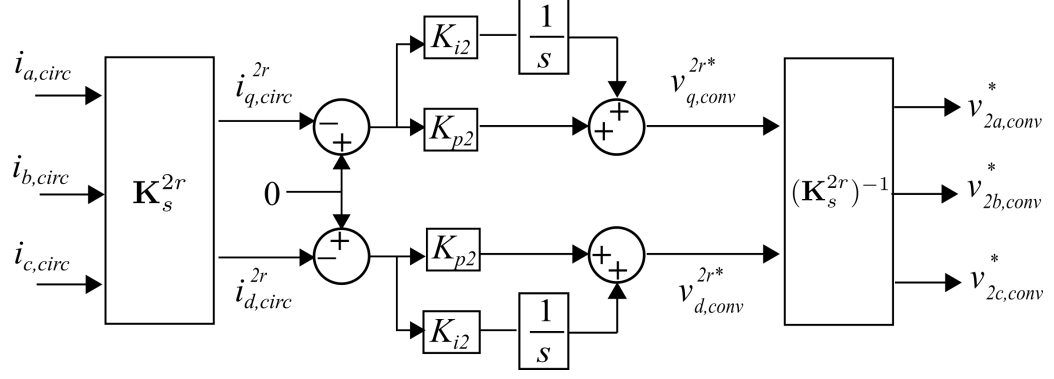


Fig. 3.5. Second Harmonic Elimination in Arm Currents

and for lower arm, $d_{x,low}$ is defined as

$$d_{x,low} = \frac{1}{2} + \frac{v_{x,conv}^*}{V_{dc}^*} - \frac{v_{2x,conv}^*}{V_{dc}^*} \quad (3.36)$$

Next, an appropriate modulation and capacitor voltage balancing technique is selected to control the DC bus voltage.

3.5 Modulation scheme and capacitor voltage balancing

3.5.1 Level-shifted Sinusoidal Pulse Width Modulation

Based on the commanded voltages, a level-shifted Sinusoidal Pulse Width Modulation (SPWM) scheme is utilized to calculate number of submodules to be turned on in each arm [36]. It uses the duty cycle calculated from (3.35) and (3.36) for each phase. This modulation technique is demonstrated for a test case of 2 submodules as shown in Fig. 3.6. The upper trace in Fig. 3.6 shows a comparison of the duty cycle with level-shifted triangles whereas the lower trace shows the number of submodules to be turned on accordingly. For example, if the duty cycle has value greater than the lower triangle wave but lower than the upper triangle wave, one submodule is turned on. Similarly, if the duty cycle has value greater than the upper triangle wave, both submodules are turned on. If duty cycle is smaller than the lower triangle wave, no submodules are turned on as shown in Fig. 3.6.

3.5.2 Capacitor voltage balancing scheme

The switching signal for each submodule is determined using capacitor voltage balancing technique which ensures that the capacitor voltage in all submodules of a arm are equal [36]. In Fig. 3.7, the switching scheme is shown for upper arm of a -phase. Herein, $N_{a,up}$ and $N_{a,low}$ represent number of submodules to be turned on for upper arm and lower arm, respectively, of a -phase. Consider upper arm of a -phase of the MMC. Assuming that at some switching instant, the level-shifted SPWM modulation technique determines that a total of $N_{a,up}$ submodules are required to be turned on out of N submodules. If capacitor voltages are sorted, the balancing technique would determine the direction of current going through the i^{th} capacitor if the i^{th} submodule is to be turned on. If the direction of current is such that it would charge the capacitors, the voltage balancing technique would turn on $N_{a,up}$ submodules which have the lowest voltage out of N submodules. Similarly, if the current going through the capacitors discharges the capacitors, the technique would turn on $N_{a,up}$ submodules which have the highest voltage. Using such submodule switching technique, total energy exchange by all the submodules in one arm will be nearly equal in one power cycle. This will ensure the requirement of same capacitor voltage variation in all the submodules of a arm.

3.6 Simulation Results of Waveform-level Model

To demonstrate the simulation of the developed simulation model, a notional 100 kW generator rectifier system with 2 kV DC bus voltage is considered. The generator has 16 poles with $L_q = L_d = 0.6$ mH, $\lambda_m = 0.23$ Vs and R_s is 20 m Ω . The load resistance R_L is set equal to 40 Ω . The generator speed is kept at 3000 RPM. There are 4 submodules per arm, and the arm filter self inductance $L_{s,i}$ is kept at 0.36 mH. The inductor series resistance R_i is 16 m Ω and the capacitor equivalent series resistance is 39 m Ω . The submodule capacitance is set equal to 1.38 mF and the switching frequency is equal to 13.36 kHz. The switch forward voltage drop $V_{sw,fw}$ is

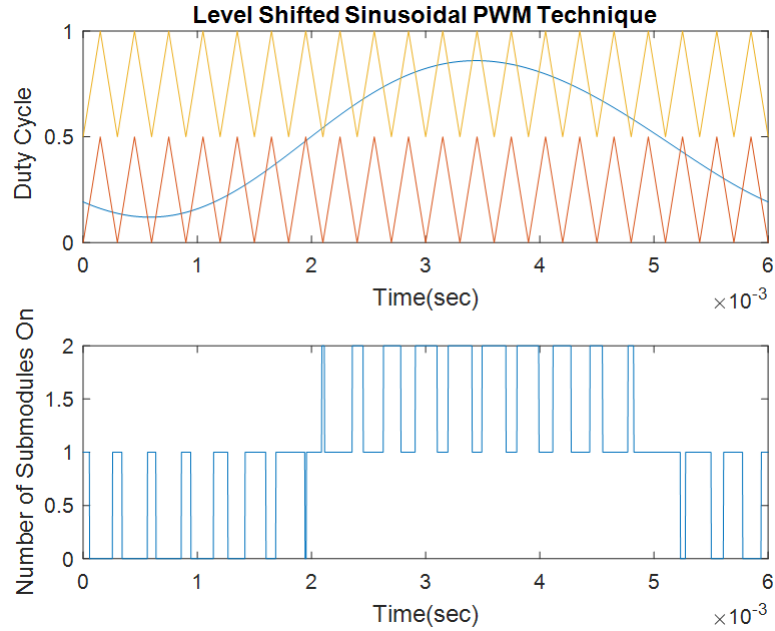
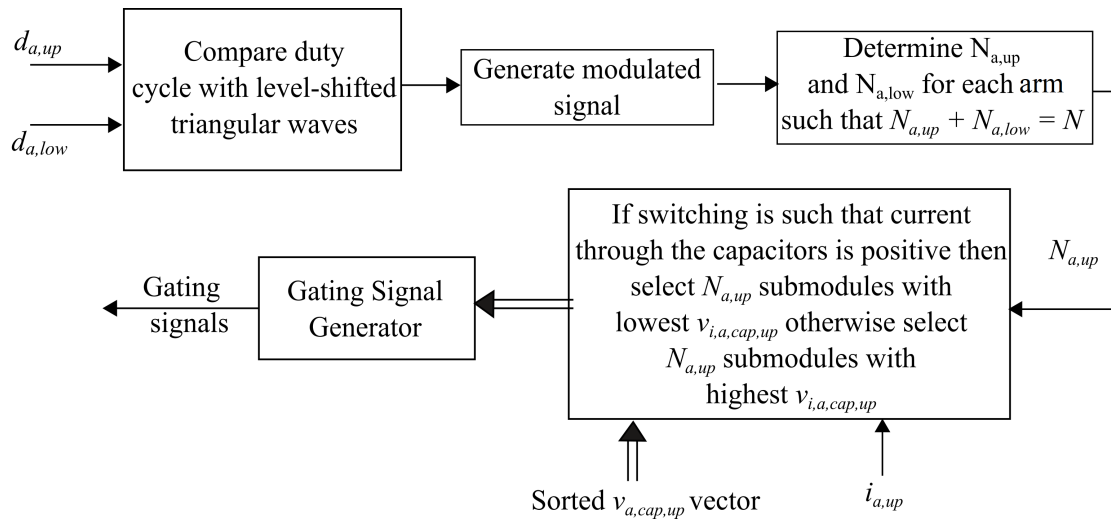


Fig. 3.6. Level-Shifted Sinusoidal PWM

Fig. 3.7. Switching Scheme for Upper Arm of a -phase of the MMC

0.6 V and the forward resistance $R_{sw, fw}$ is $15.28 \mu \text{ m}\Omega$. The diode forward voltage drop $V_{d, fw}$ is 0.56 V and the forward resistance $R_{d, fw}$ is $1.7 \mu \text{ m}\Omega$. MATLAB Simulink is utilized to simulate the developed model.

In this work, steady state waveforms are of interest, and hence the results, as shown in Figs. 3.8 - 3.12, are at steady state of the system. As can be seen, the controllers have been able to control the DC bus and the generator current, balance the capacitor voltages, and eliminate the second harmonic current. However, some higher order harmonics exist, as can be seen MMC arm currents and DC load current. To this end, the model will be used in subsequent chapters to validate the developed high-speed simulation model.

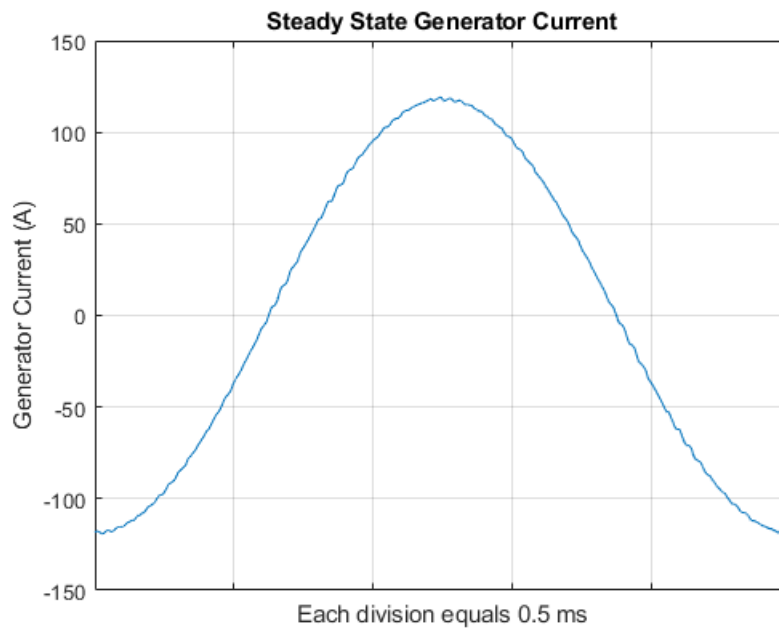


Fig. 3.8. Generator Current

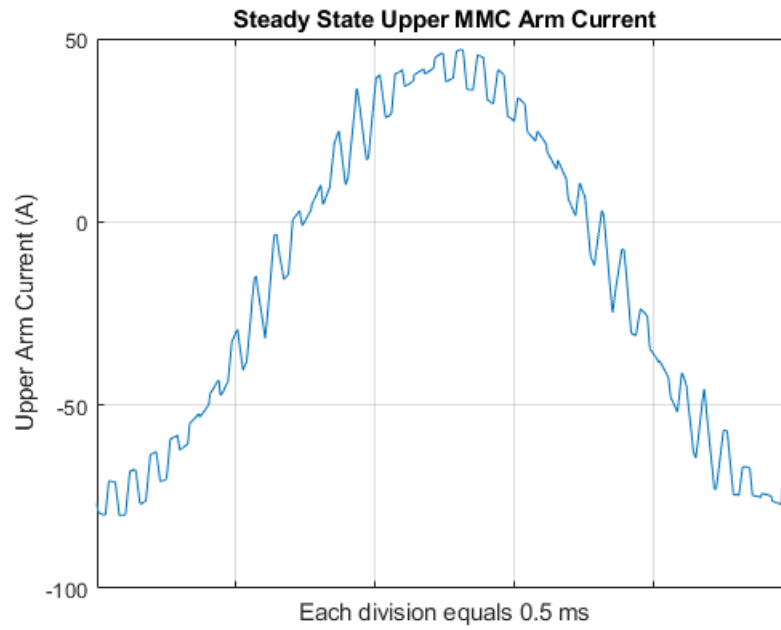


Fig. 3.9. MMC Upper Arm Current

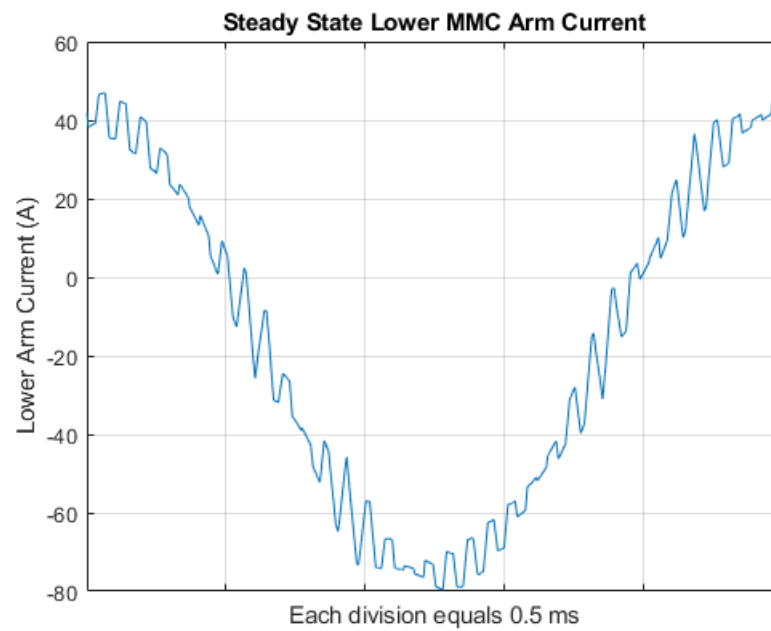


Fig. 3.10. MMC Lower Arm Current

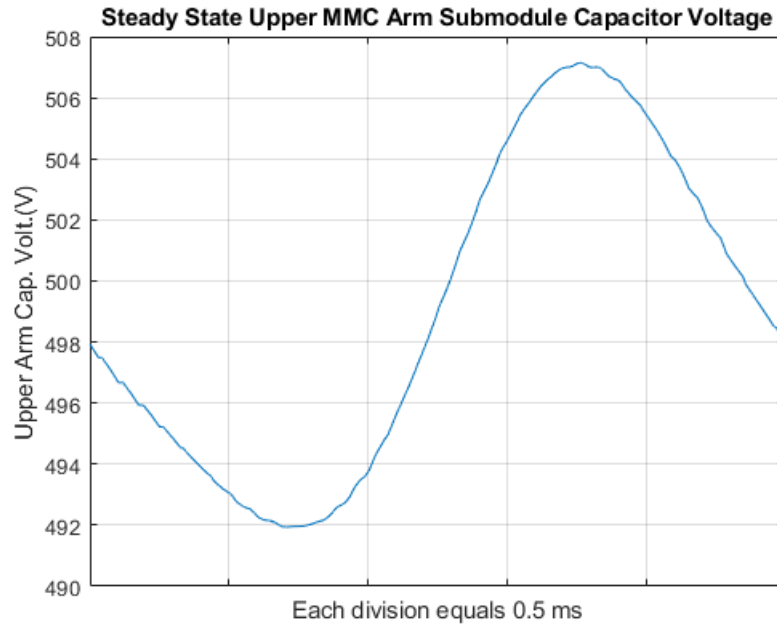


Fig. 3.11. MMC Upper Arm Submodule Capacitor Voltage

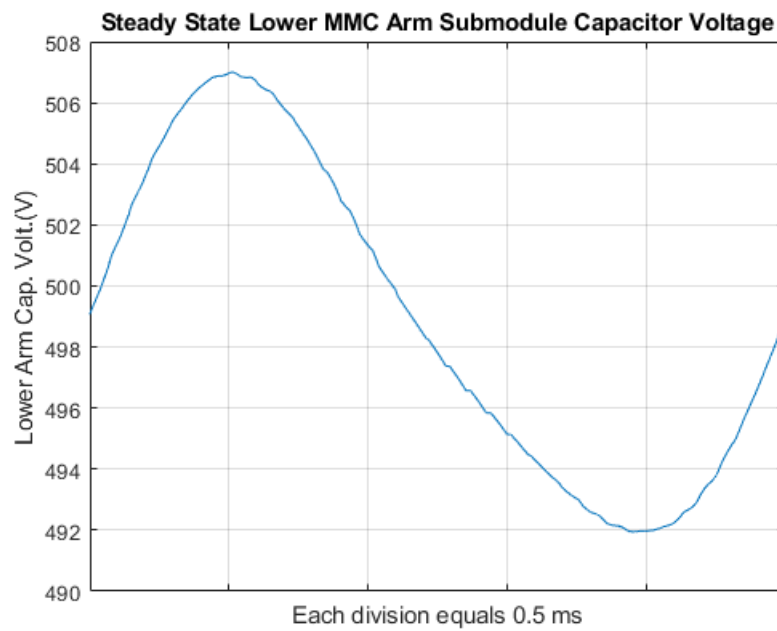


Fig. 3.12. MMC Lower Arm Submodule Capacitor Voltage

4. HIGH-SPEED SIMULATION OF THE PMAC-MMC SYSTEM

The objective of the high-speed simulation is to rapidly estimate steady-state waveforms of the MMC based generator rectifier system. In previous chapter, a detailed model of the system was developed. Though the detailed model can estimate the variables accurately, its computational intensity discourages its use in optimization based design. To overcome slow execution of detailed model of MMC simulations, computationally efficient simulation models of the system have been developed in literature.

In [37], [38], [39] and [40] efficient average-value models of the MMC system are proposed. These models are developed for study of faults or sudden load change. However, these models do not consider the harmonic components in the arm currents required for passive component sizing. Alternatively, [41], [42] and [43] propose fast simulation models for transient studies of MMCs. In [41], detailed dynamics of each MMC capacitor and inductor is modeled. Computational efficient simulation is achieved using average models for balancing control of capacitors and ignoring the detailed switching dynamics of each submodule. Models developed in [42] and [43] include the voltage and current control. While this is useful, a model is still required which can estimate the system waveforms in steady-state without carrying out transient analysis. Fast waveform-level models are still needed which can estimate and produce reasonably accurate steady-state system waveforms which includes switching frequency ripple. Such a model is set forth herein in the context of the generator rectifier system shown in Fig. 3.1.

In the framework of multi-objective optimization of the considered PMAC-MMC system, inputs to the developed high-simulation are parameters of the PMAC generator (such as circuit parameters, speed, core-losses) and MMC (number of submodules,

switching frequency, passive and active device parameters), and its outputs are current and voltage waveforms of the generator and MMC. Appropriate assumptions and simplifications are made in this chapter to reduce the complexity of the solver without major compromises in the accuracy of the waveforms.

For steady-state operation, it can be reasonably assumed that capacitor voltages in an arm are balanced. This assumption will help in reducing the simulation order of the system by modeling all the capacitors in an arm to be represented by a single capacitor. It is also assumed that the MMC is not operated in the over-modulation region during steady-state conditions. For normal operation, over-modulated operation of MMCs is not desired so as to avoid increase in harmonic content and decrease in power quality [44]. During the model formulation, most of the equations will be derived for the $a-$ phase upper MMC arm quantities since the $b-$, $c-$ phases of machine and upper and lower MMC arms exhibit similar behaviour.

In the physical system, and in the detailed simulation model, the second-harmonic component of the arm currents are eliminated using a controller as described in Section 3.4. Hence, it will be assumed that there is no second-harmonic component of the arm currents. It is also assumed that DC bus voltage is constant at the desired value. Using upper case variables to represent DC quantities, in terms of the DC power output P_{dc} and the DC bus voltage V_{dc} , the constant DC load current I_{dc} can be calculated as

$$I_{dc} = \frac{P_{dc}}{V_{dc}} \quad (4.1)$$

4.1 Calculation of Generator Current, and DC and Fundamental Component of MMC Current

The first step in the simulation is to estimate the power loss in the system and the generator currents. To this end, using power balance, the steady-state $q-$ and $d-$ axis currents can be calculated as

$$I_{qs}^r = \frac{-2(P_{go} + P_r)}{3\omega_r \lambda_m} \quad (4.2)$$

$$I_{ds}^r = 0 \quad (4.3)$$

where I_{qs}^r and I_{ds}^r are the steady-state values of q - and d - axis machine currents, and P_{go} is the generator output power and P_r is generator winding losses. In (4.2), it is assumed that PMAC generator core losses (eddy current and hysteresis) primarily act as windage losses, and do not significantly change the I_{qs}^r . Since MMC losses are unknown at this stage, P_{go} is unknown and (4.2) will be solved iteratively using the loss calculation formulations presented in Chapter 2, 5 and 6. In (4.3), it is assumed that DC bus voltage is sufficient for operation without flux weakening so no d - axis current is injected. However, it will be retained as a variable in the interest of generality. The a -phase generator current can be calculated as

$$i_{as} = I_{qs}^r \cos \theta_r + I_{ds}^r \sin \theta_r \quad (4.4)$$

where θ_r is the reference frame angle.

From power balance, the fundamental plus DC component of upper arm currents in the a -phase, $i_{a,up,dc+f}$ is calculated as [29]

$$i_{a,up,dc+f} = -\frac{I_{dc}}{3} + \frac{i_{as}}{2} \quad (4.5)$$

Similarly, for lower arm, $i_{a,low,dc+f}$ can be expressed as

$$i_{a,low,dc+f} = -\frac{I_{dc}}{3} - \frac{i_{as}}{2} \quad (4.6)$$

4.2 MMC AC side Fundamental Converter Voltage

For the calculation of fundamental duty cycle, from (3.35), fundamental component of MMC AC side converter voltage $v_{a,conv}$ is required. Using (3.24), (3.25), (3.33), and assuming steady-state conditions, the steady state q - and d - component of converter voltages are given by

$$V_{q,conv}^r = R_{eq} I_{qs}^r + \omega_r \lambda_m + \omega_r L_{d,eq} I_{ds}^r \quad (4.7)$$

$$V_{d,conv}^r = R_{eq} I_{ds}^r - \omega_r L_{q,eq} I_{qs}^r \quad (4.8)$$

Using the inverse reference frame transformation, the fundamental component of a -phase converter voltage $v_{a,conv}$ can be expressed using (3.34) as

$$v_{a,conv} = V_{q,conv}^r \cos(\theta_r) + V_{d,conv}^r \sin(\theta_r) \quad (4.9)$$

4.3 Capacitor Voltage Ripple Calculations

As mentioned earlier, it is assumed that capacitor voltage has DC, fundamental, and second harmonic components. All other harmonic components are neglected. For the a -phase, the capacitor voltage in upper arm, $v_{a,cap,up}$ and lower arm $v_{a,cap,low}$ are assumed to be of form

$$v_{a,cap,up} = \kappa \frac{V_{dc}}{N} + V_{c1} \cos(\theta_r + \phi_{c1}) + V_{c2} \cos(2\theta_r + \phi_{c2}) \quad (4.10)$$

$$v_{a,cap,low} = \kappa \frac{V_{dc}}{N} - V_{c1} \cos(\theta_r + \phi_{c1}) + V_{c2} \cos(2\theta_r + \phi_{c2}) \quad (4.11)$$

where κ is a factor that addresses the fact that the average capacitor voltage is slightly less than V_{dc}/N .

To derive a value for κ , from KVL in (3.16), the DC bus voltage should be equal to the time average sum of the voltage in upper arm, lower arm and voltage drop in arm inductors. Considering the DC component of voltage and current in each arm, same DC current flows through the upper and lower arm. Since each arm should exchange equal energy in a fundamental cycle, the time average voltage across upper arm and lower arm should be equal to half of DC bus voltage. The factor κ can be calculated using this fact. For the upper arm [45]

$$\overline{v_{a,up} + i_{a,up} R_i} \approx N \overline{\left(\frac{1}{2} - \frac{v_{a,conv}}{V_{dc}} \right)} + \overline{v_{sd,a,up}} - \frac{R_i i_{dc}}{3} \quad (4.12)$$

should be equal to $V_{dc}/2$. In (4.12), $v_{a,conv}$ is the converter voltage as defined in (3.33) and (3.34), and $v_{sd,a,up}$ is equivalent voltage drop across semiconductor devices. The first term in right hand side of (4.12) is approximated arm voltage due to submodule capacitors, second term is contributed by semiconductor forward drops, and third term is contributed by switch and inductor resistive drop across R_i . It should be

noted that since the average current through submodule capacitor should be zero, no contribution from capacitor ESR will be observed in (4.12). Using expressions of converter voltage (4.9), capacitor voltage (4.10), approximated semiconductor forward drop considering only the fundamental component in arm current, κ is calculated as [29]

$$\kappa \approx 1 + \frac{NV_{c1}}{V_{dc}^2} (V_{q,conv}^r \cos(\phi_{c1}) - V_{d,conv}^r \sin(\phi_{c1})) + \frac{2(NR_{hsw} + R_1)}{3R_L} - \frac{2NV_{hsw}}{V_{dc}} \left(\frac{\theta_{rc}}{\pi} - 1 \right) \quad (4.13)$$

where

$$\theta_{rc} = 2 \cos^{-1}(2I_{dc}/(3I_s)) \quad (4.14)$$

$$R_{hsw} = 2 \cdot \max(R_{d,fw}, R_{sw,fw}) \quad (4.15)$$

$$V_{hsw} = 2 \cdot \max(V_{d,fw}, V_{sw,fw}) \quad (4.16)$$

$$I_s = \sqrt{(I_{qs}^r)^2 + (I_{ds}^r)^2} \quad (4.17)$$

and where $R_{d,fw}$ and $R_{sw,fw}$ are equivalent resistive drops and $V_{d,fw}$ and $V_{sw,fw}$ are voltage drops in forward biased semiconductor devices as defined in Chapter 3.

Next, calculation of derivative of capacitor voltages is undertaken. Capacitor voltage derivatives along with (4.10), (4.11) and (4.13) are used in the calculation of capacitor voltage waveform. The change in capacitor charge $\Delta q_{i,a,up}$ for capacitor i in upper arm of phase- a of the MMC between time t and $t + \Delta\tau$ can be calculated as

$$\Delta q_{i,a,up} = s_{i,a,up} i_{a,up} \Delta\tau \quad (4.18)$$

where $\Delta\tau$ is small time interval. The sum of change in capacitor charge can be expressed as

$$\sum_{i=1}^N \Delta q_{i,a,up} = \sum_{i=1}^N s_{i,a,up} i_{a,up} \Delta\tau \quad (4.19)$$

Since it is assumed that all the capacitors in a arm have equal capacitor voltage, it should be that total change in capacitor charge gets equally distributed among all the capacitors in a arm. In other words, it can written that

$$\Delta v_{a,cap,up}/\Delta\tau = \frac{\sum_{i=1}^N \Delta q_{i,a,up}}{NC_{sm}\Delta\tau} \quad (4.20)$$

which, taking $\Delta\tau \rightarrow 0$, yields

$$pv_{a,cap,up} = \frac{\sum_{i=1}^N s_{i,a,up} i_{a,up}}{NC_{sm}} = \frac{\sum_{i=1}^N s_{i,a,up}}{N} \frac{i_{a,up}}{C_{sm}} \quad (4.21)$$

Equation (4.21) yields the general expression in terms of switching signals and arm currents in upper arm.

Assuming that the capacitor voltage is predominantly driven by the DC and fundamental component of duty cycle and arm current

$$\sum_{i=1}^N s_{i,a,up} i_{a,up} \approx Nd_{a,up} i_{a,up} \quad (4.22)$$

which is further approximated using only the DC and fundamental component of duty cycle (from (3.35) and (4.9)) as

$$Nd_{a,up} i_{a,up} \approx N \left(\frac{1}{2} - \frac{v_{a,conv}}{V_{dc}} \right) i_{a,up,dc+f} \quad (4.23)$$

Hence, derivative of $v_{a,cap,up}$ can be approximated using

$$pv_{a,cap,up} \approx \frac{i_{a,up,dc+f}}{C_{sm}} \left(\frac{1}{2} - \frac{v_{a,conv}}{V_{dc}} \right) \quad (4.24)$$

At this stage, derivative of upper arm capacitor voltage can be approximated using expression of $i_{a,up,dc+f}$ from (4.5) and $v_{a,conv}$ from (4.9). Similarly, derivative of lower arm capacitor voltage can be approximated as

$$pv_{a,cap,low} \approx \frac{i_{a,low,dc+f}}{C_{sm}} \left(\frac{1}{2} + \frac{v_{a,conv}}{V_{dc}} \right) \quad (4.25)$$

Taking derivative of (4.10) and equating it to (4.24) yields

$$V_{c1} \cos(\phi_{c1}) = -\frac{I_{ds}^r}{4\omega_r C_{sm}} - \frac{V_{d,conv}^r I_{dc}}{3V_{dc}\omega_r C_{sm}} \quad (4.26)$$

$$V_{c1} \sin(\phi_{c1}) = -\frac{I_{qs}^r}{4\omega_r C_{sm}} - \frac{V_{q,conv}^r I_{dc}}{3V_{dc}\omega_r C_{sm}} \quad (4.27)$$

Similarly, taking derivative of (4.11) and equating it to (4.25) yields

$$V_{c2} \cos(\phi_{c2}) = \frac{I_{qs}^r V_{d,conv}^r + I_{ds}^r V_{q,conv}^r}{8V_{dc}\omega_r C_{sm}} \quad (4.28)$$

$$V_{c2} \sin(\phi_{c2}) = \frac{I_{qs}^r V_{q,conv}^r - I_{ds}^r V_{d,conv}^r}{8V_{dc}\omega_r C_{sm}} \quad (4.29)$$

Substituting (4.13),(4.26) and (4.27) in (4.10) calculates the upper arm capacitor voltage waveform. Similarly, the upper arm capacitor voltage waveform can be calculated. This is a low frequency estimate which includes low-frequency (but not the high-frequency) behavior.

4.4 Submodule Duty Cycle and Switching Signal Calculation

The fundamental component of duty cycle can be calculated using (3.35) and (4.9). To eliminate the second harmonic component MMC arm current, a common mode second harmonic component of converter voltage is injected as shown in Chapter 3. This requires estimation of the second harmonic component of MMC arm voltage. To this end, the second harmonic component of MMC a - phase upper arm voltage $v_{a,up}$, denoted $v_{a,up,2\theta_r}$, can be calculated as

$$v_{a,up,2\theta_r} = N (v_{a,cap,up} d_{a,up}) |_{2\theta_r} + v_{sd,a,up} |_{2\theta_r} \quad (4.30)$$

where $d_{a,up}$ is the a - phase upper arm duty cycle, which, using (3.35), is given as

$$d_{a,up} = \frac{1}{2} - \frac{v_{a,conv}}{V_{dc}} - \frac{v_{2a,conv}}{V_{dc}} \quad (4.31)$$

From the control, $v_{a,up,2\theta_r}$ should be zero. The second harmonic component of converter voltage $v_{2a,conv}$ is assumed to be of the form

$$v_{2a,conv} = V_{2a,conv} \cos(2\theta_r + \phi_{f2}) \quad (4.32)$$

To calculate $V_{2a,conv}$ and ϕ_{f2} such that (4.30), from expressions of capacitor voltage at (4.10), $v_{a,conv}$ in (4.9) and $v_{2a,conv}$ in (4.32), it yields [45]

$$V_{2a,conv} \cos(\phi_{f2}) = \frac{N}{2\kappa} V_{c2} \cos(\phi_{c2}) - \frac{N}{2\kappa} \frac{V_{c1} \cos(\phi_{c1}) V_{q,conv}^r}{V_{dc}} - \frac{N}{2\kappa} \frac{V_{c1} \sin(\phi_{c1}) V_{d,conv}^r}{V_{dc}} + \frac{2NV_{hsw} \sin(2\theta_{rc}) \cos(2\phi_s)}{\pi\kappa} \quad (4.33)$$

$$V_{2a,conv} \sin(\phi_{f2}) = \frac{N}{2\kappa} V_{c2} \sin(\phi_{c2}) + \frac{N}{2\kappa} \frac{V_{c1} \cos(\phi_{c1}) V_{d,conv}^r}{V_{dc}} - \frac{N}{2\kappa} \frac{V_{c1} \sin(\phi_{c1}) V_{q,conv}^r}{V_{dc}} + \frac{2NV_{hsw} \sin(2\theta_{rc}) \sin(2\phi_s)}{\pi\kappa} \quad (4.34)$$

From (4.33) and (4.34), $v_{2a,conv}$ can be calculated in (4.32).

Using fundamental and second harmonic component of converter voltage from (4.9) and (4.32), the duty cycle for upper arm submodules can be calculated using (4.31). Similar calculations can be done for lower arm submodules.

Given the duty cycle for a - phase upper and lower MMC arms, switching signals for the submodules is calculated using the sinusoidal PWM modulation scheme described in Chapter 3, assuming that the capacitors in a MMC arm have balanced voltages.

4.5 Currents in MMC Arm and DC Bus Capacitor

Assuming negligible harmonic voltage drop in the semiconductor devices and the inductor resistance, the total voltage across the upper arm submodules in the a -phase can be expressed as

$$v_{a,up}(t) \approx v_{a,cap,up}(t) \sum_{i=1}^N s_{i,a,up}(t) + v_{sd,a,up}(t) + R_i i_{a,up,dc+f}(t) \quad (4.35)$$

In (4.35), $\sum_{i=1}^N s_{i,a,up}(t)$ is the total number of submodules turned on at an instant t for the upper arm of a -phase, and R_i is the inductor resistance. Semiconductor devices are modeled using ideal devices with device forward biased resistive and voltage drops,

as discussed in Chapter 3. Similarly, for lower arm, total voltage across submodules, $v_{a,low}$, can be calculated as

$$v_{a,low}(t) \approx v_{a,cap,low}(t) \sum_{i=1}^N s_{i,a,low}(t) + v_{sw,a,low}(t) + R_i i_{a,low,dc+f}(t) \quad (4.36)$$

The voltage $v_{a,ul}$ is defined as the voltage drop across the two arm inductors if their resistive drops were represented externally. Using (4.35) and (4.36)

$$v_{a,ul}(t) \approx V_{dc} - v_{a,up} - v_{a,low} + \frac{2R_i I_{dc}}{3} \quad (4.37)$$

Similar equations can be expressed for $b-$, $c-$ phases. Ideally, $v_{x,ul}$, $x \in \{‘a’, ‘b’, ‘c’\}$ should have zero DC component. However, due to the approximations made through the formulation of the simulation and numerical errors, $v_{x,ul}$ will have some small DC component, $\overline{v_{x,ul}}$. To calculate arm currents, this DC component will be subtracted from $v_{x,ul}$. Thus the circulatory component of arm currents $i_{x,ul}$ is governed by

$$\mathbf{L}_1 \mathbf{p} i_{abc,ul} = \mathbf{v}_{abc,ul} - \overline{\mathbf{v}_{abc,ul}} \quad (4.38)$$

Integrating (4.38) with approximate initial condition $i_{a,ul}(0) \approx -\frac{2I_{dc}}{3}$ yields $i_{a,ul}$. The arm currents can be calculated as in $x-$ phase can be calculated as

$$i_{x,up} = \frac{i_{xs} + i_{x,ul}}{2} \quad (4.39)$$

$$i_{x,up} = \frac{-i_{xs} + i_{x,ul}}{2} \quad (4.40)$$

The harmonic component in DC bus capacitor current can be estimated by evaluating the arm currents for remaining $b-$ and $c-$ phases of the MMC. To this end, the estimated harmonic current in DC bus capacitor C_{in} is given by

$$i_{cin,rip} = \left(-I_{dc} - \sum_{x \in \{‘a’, ‘b’, ‘c’\}} \frac{i_{x,ul}}{2} \right) \quad (4.41)$$

4.6 Total Loss Calculation and Convergence

The total MMC losses $P_{l,mmc}$ are calculated as

$$P_{l,mmc} = 6P_i + 6P_{cd,up} \quad (4.42)$$

where P_i is inductor resistive loss, and $P_{cd,up}$ is upper arm semiconductor conduction loss. Semiconductor switching losses, capacitor ESR loss and inductor core losses have not been considered, however, can be included using the models set-forth in Chapters 5 and 6.

The generator output power P_{go} is given by

$$P_{go} = P_{dc} + P_{mmc} \quad (4.43)$$

using which (4.2) is solved until the solution reaches convergence. This completes the high-speed simulation of the MMC system.

To summarize the steps, the simulation begins with calculations of the DC component of the arm current using (4.1). Next, generator current is calculated iteratively using (4.2) - (4.4). In the process, machine and MMC losses are updated. For this, first, the fundamental component of duty cycle is calculated using Section 4.2. Next, using the fundamental component of duty cycle, submodule capacitor voltage waveforms are estimated using equations presented in Section 4.3. Next, using the fundamental converter voltage calculated in Section 4.2, and calculations for common mode second harmonic component of duty cycle presented in Section 4.4, the net submodule duty cycle and switching signals are calculated using modulation scheme presented in Chapter 3 for upper and lower arms. Using the calculated switching signals, MMC arm and DC bus capacitor currents are calculated as presented in Section 4.5. Finally, total MMC losses using (4.42) are calculated. This process is repeated till the solution of P_{go} is reached.

Note that the developed high-speed simulation requires a non-linear solver which utilizes an error criterion defined based on difference in MMC loss estimation between current and previous iteration. The solution is reached if the error falls below a defined threshold. A flow chart of the process is shown in Fig. 4.1. In the simulation, waveforms of machine current, capacitor voltages, arm currents and load current are calculated.

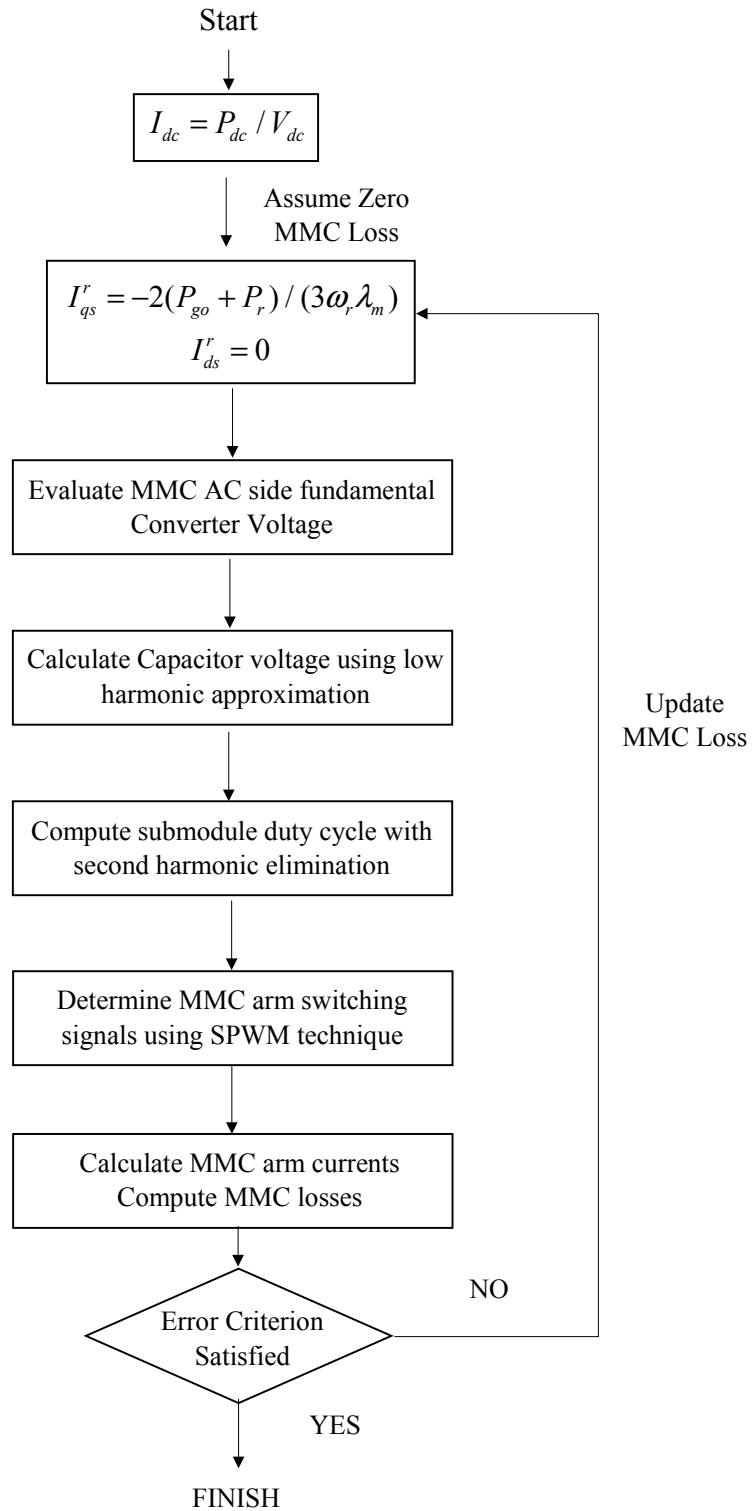


Fig. 4.1. High-Speed Simulation Flow Chart for Generator-Rectifier System

4.7 Comparison between detailed and high-speed simulation model

To verify the high-speed simulation model, a comparison between simulation results from high-speed and detailed simulation model is carried out. Such validation studies illustrate the advantages as well as limitations of the developed high-speed simulation model in estimating the steady state waveforms in the MMC. The computational efficiency of the high-speed simulation in estimation of the variables as compared to a detailed simulation model is also included. Three test cases are considered for the validation.

4.7.1 Case A

A notional low power 37.5 kW generator rectifier system with 750 V DC bus voltage is used. The permanent Magnet AC generator acts as the source for the MMC as shown in Fig. 3.1. The generator has 8 poles with $L_q = L_d = 0.73$ mH, $\lambda_m = 0.23$ Vs and $R_s = 39$ m Ω , and is operated at 2500 rpm. For the first case, the system is operated under full load, with $R_L = 15\Omega$, there are 2 submodules per arm, and the arm self inductance $L_{s1} = 0.1$ mH. The inductor is assumed to have zero resistance and zero mutual coupling between the phases. The submodule capacitance is 1 mF and the switching frequency is 30 kHz. In both the simulation models (detailed and high-speed MMC simulation), , semiconductor devices are modeled as ideal devices with forward voltage and resistance drops. The switch forward voltage drop $V_{sw, fw} = 2.1$ V and the forward resistance $R_{sw, fw} = 5$ m Ω . The diode forward voltage drop $V_{d, fw} = 1.9$ V and the forward resistance $R_{d, fw} = 5$ m Ω . Switching losses are ignored.

Simulink is used for the implementation of the waveform-level model using the ode45 solver with variable time-step between 10^{-8} and 10^{-6} s. The high-speed simulation is implemented on MATLAB. The secant method is used to iteratively solve the q -axis machine current, I_{qs}^r . The integration is carried out with the trapezoidal algorithm with a 0.3μ s time-step. The code is not compiled. Both models are run

on a Quad Core 3.4 GHz CPU based system running Windows 7. Results are shown in Figs. 4.2 - 4.6.

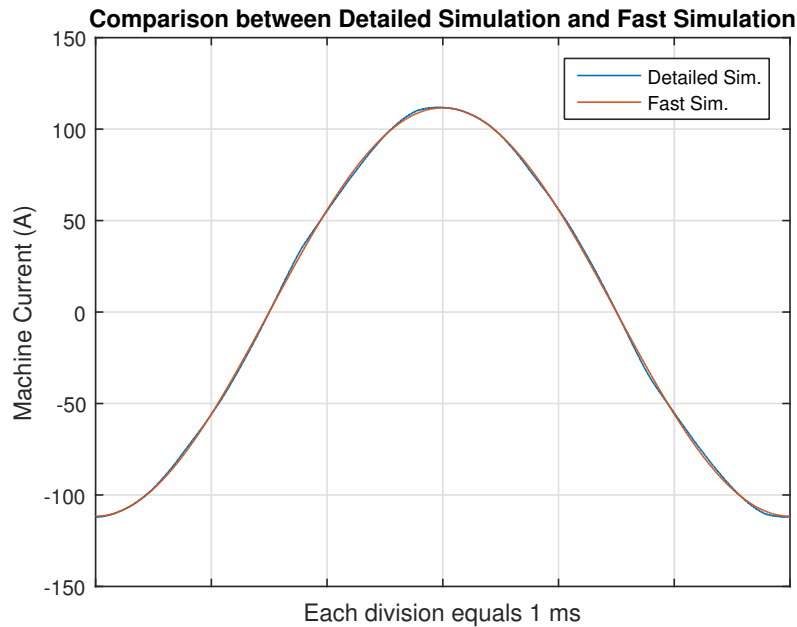


Fig. 4.2. Machine Current Comparison for Case A

As can be seen, the waveforms predictions of the two models are similar. Machine current waveforms from the two predictions match very closely. Similarly, capacitor voltage waveforms are close with 0.3 V difference between voltage ripple predicted by detailed and high-speed model, as can be seen in Figs. 4.5 - 4.6. For upper and lower arm currents, it can be noticed that the detailed model has a substantial sixth harmonic current ripple as compared to the high-speed simulation. The difference between the models can be attributed to the inability of high-speed simulation model to capture details of the control, and numerical approximations made in the high-speed simulation model.

The proposed high-speed simulation model is approximately 503 times faster than the detailed simulation model using identical hardware. It should be noted that the time taken by detailed simulation model is calculated from zero start of the

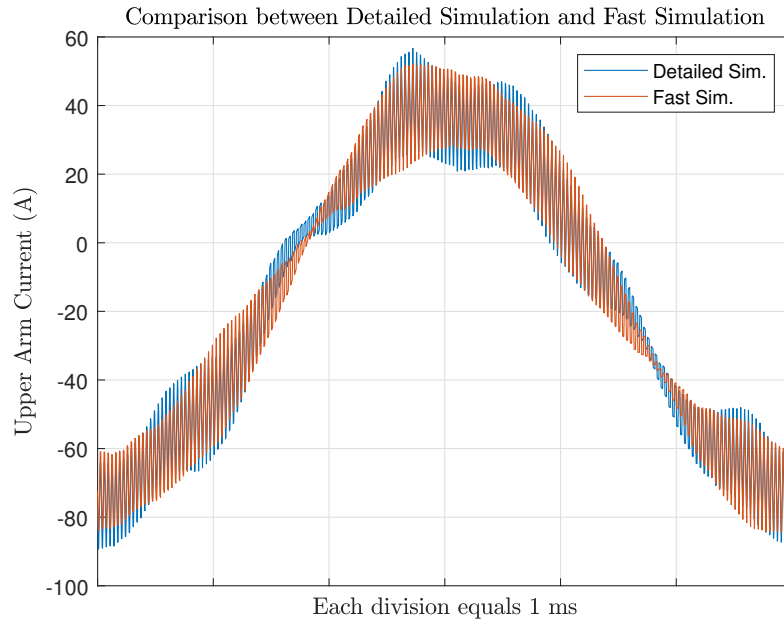


Fig. 4.3. MMC Upper Arm Current Comparison for Case A

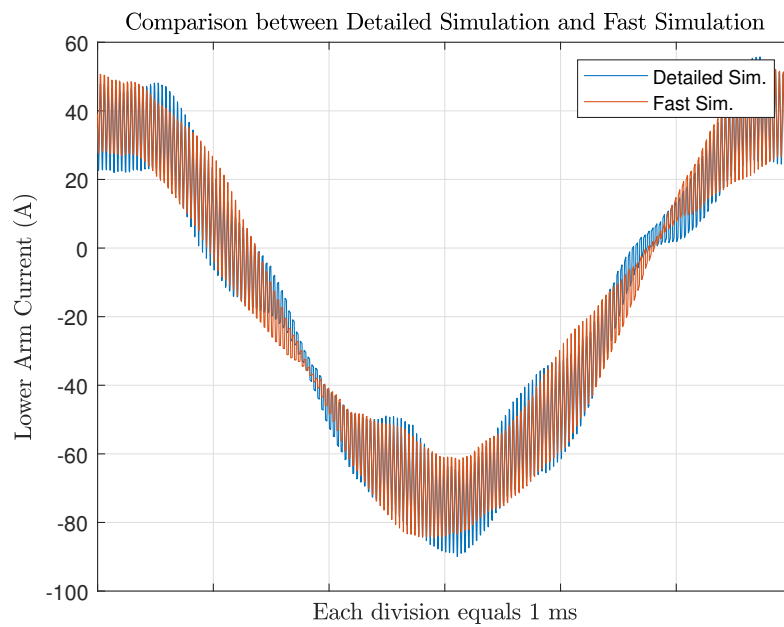


Fig. 4.4. MMC Lower Arm Current Comparison for Case A

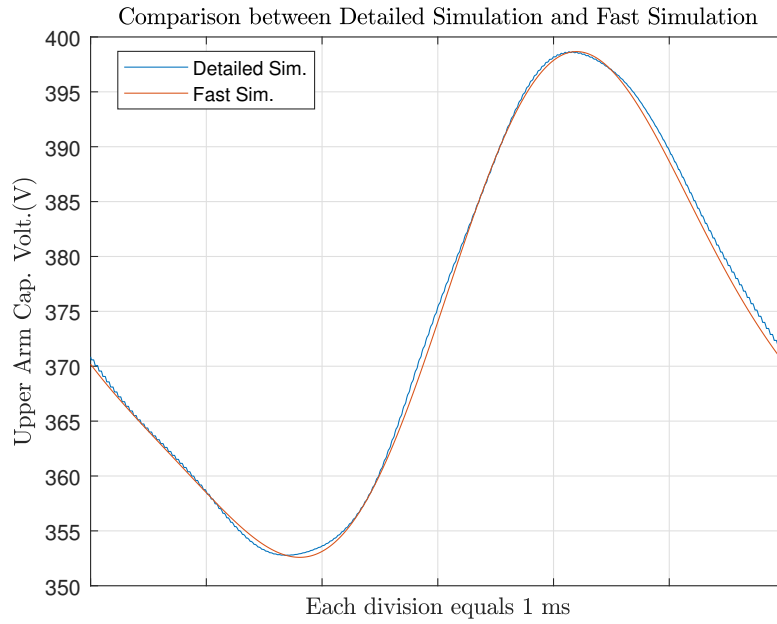


Fig. 4.5. MMC Upper Arm Submodule Capacitor Voltage Comparison for Case A

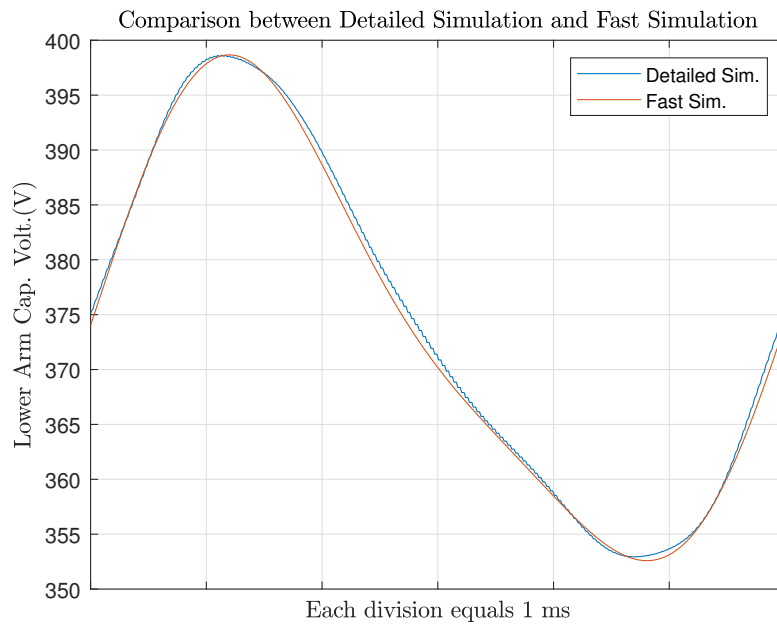


Fig. 4.6. MMC Lower Arm Submodule Capacitor Voltage Comparison for Case A

system to the point where system reaches steady-state. At steady-state, the detailed simulation takes about 0.414 seconds to perform calculations for one time period whereas high-speed simulation takes 0.0345 seconds, which is 12 times faster than detailed model. Total power loss calculated by high-speed simulation model equals 2.82 kW as compared to 2.96 kW calculated by detailed simulation model, which is a 5 % error in estimation of power loss.

4.7.2 Case B

For the second case, the generator and load parameters are kept same as subsection 4.7.1. The system is operated at full load with 4 submodules in each arm. The arm self inductance L_{s1} is increased to 0.4 mH and submodule capacitance is increased to 2 mF. The switching frequency is set to 20 kHz. The switch forward voltage drop $V_{sw, fw} = 1.05V$ and the forward resistance $R_{sw, fw} = 2.5 \text{ m}\Omega$. The diode forward voltage drop $V_{d, fw} = 0.95V$ and the forward resistance $R_{d, fw} = 2.5 \text{ m}\Omega$. All other system parameters are kept same as Case A. Similarly, Simulink algorithm parameters are kept same as first case whereas in high-speed simulation, the time step is set to $0.5 \mu s$. The time step is increased as the switching frequency is lower in Case B as compared to Case A. The same computational hardware is used to carry out the simulation as in Case A. Results are shown in Figures 4.7 - 4.11.

As in Case A, the machine current waveforms match very closely. In this case, it can be observed that the arm currents also match very closely. This is due to relatively high inductance and high submodule count which suppresses the harmonic content in the arm current. The capacitor voltage waveform calculations are similar with 0.1 V difference in voltage ripple calculations. In this case, high-speed simulation is 577 times faster than the detailed model. At steady-state, the detailed simulation takes about 0.42 seconds to perform calculations for one time period whereas high-speed simulation takes 0.0346 seconds, which is 12.1 times faster than detailed model. Total power loss calculated by high-speed simulation model is 2.82 kW as compared to 2.97

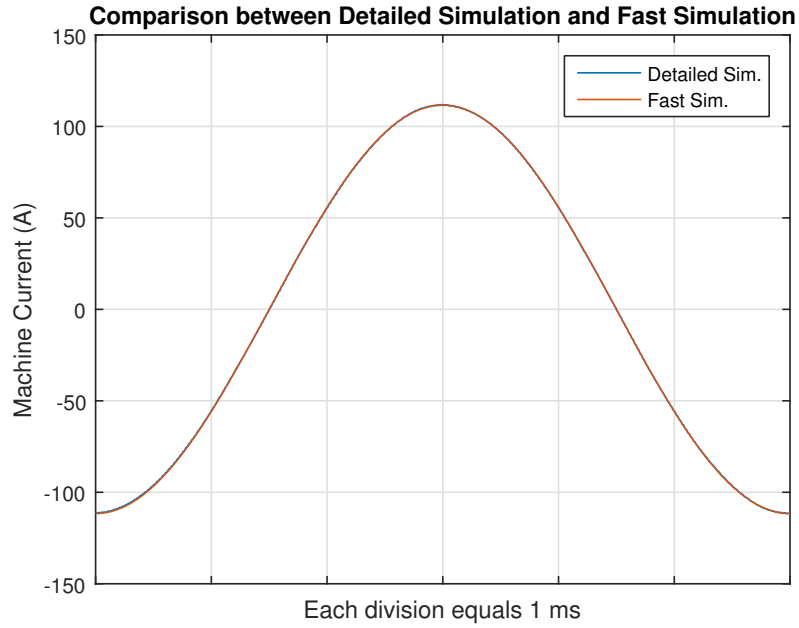


Fig. 4.7. Machine Current Comparison for Case B

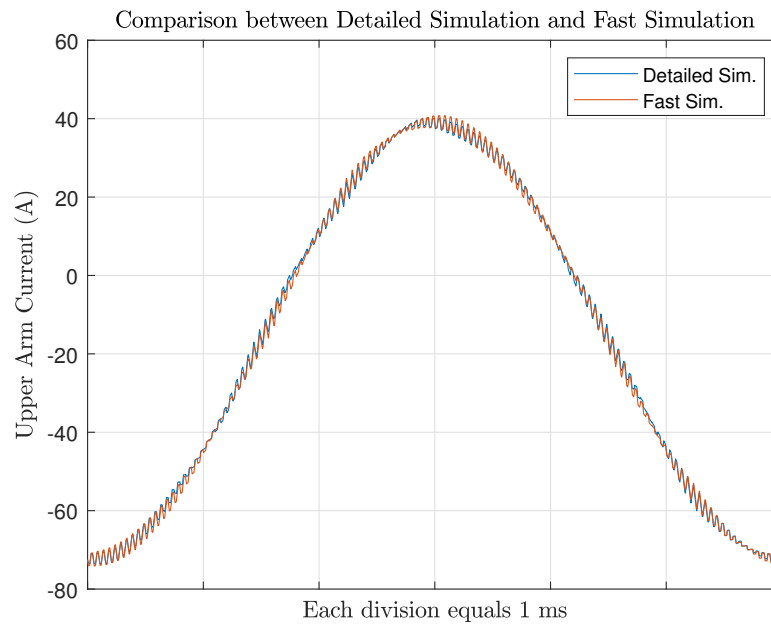


Fig. 4.8. MMC Upper Arm Current Comparison for Case B

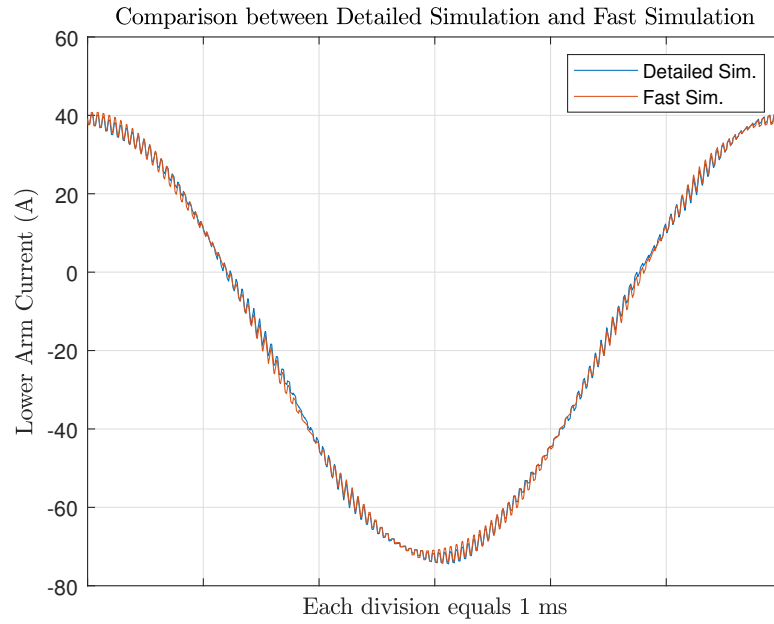


Fig. 4.9. MMC Lower Arm Current Comparison for Case B

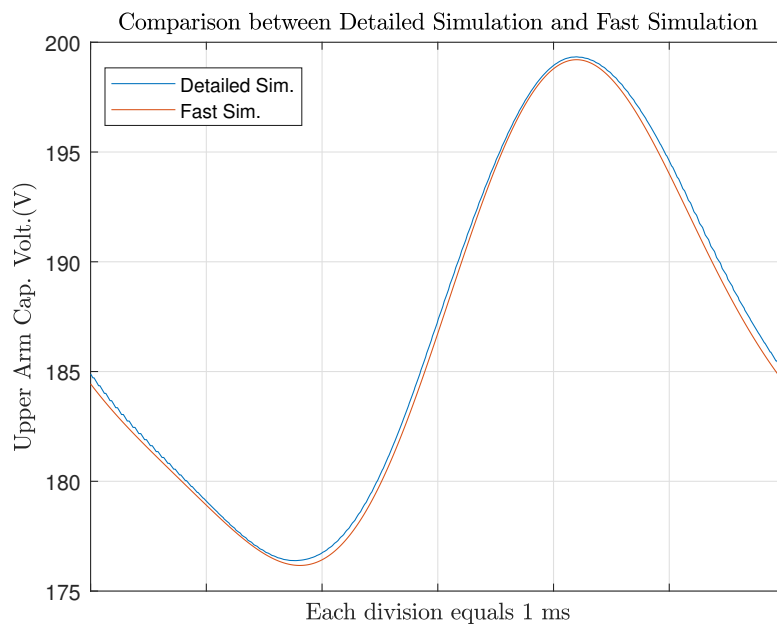


Fig. 4.10. MMC Upper Arm Submodule Capacitor Voltage Comparison for Case B

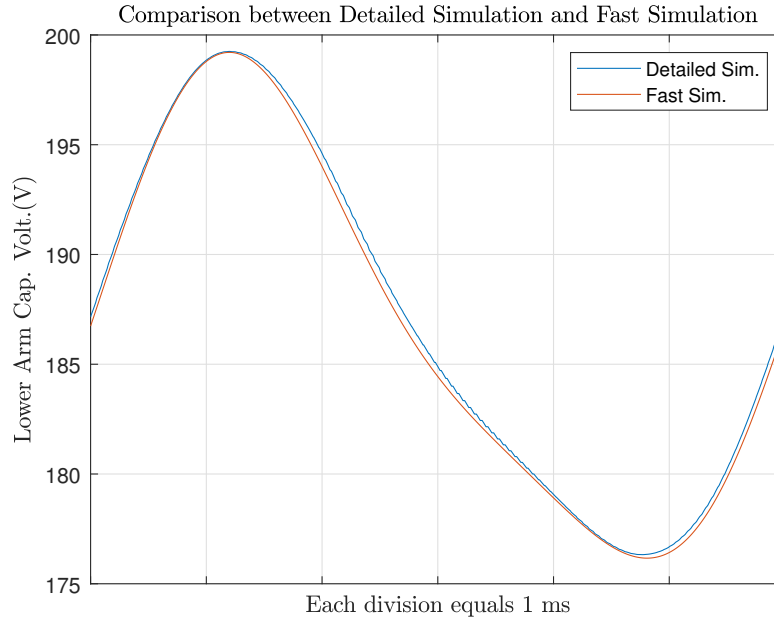


Fig. 4.11. MMC Lower Arm Submodule Capacitor Voltage Comparison for Case B

kW calculated by detailed simulation model, which is a 5 % error in estimation of the power losses.

4.7.3 Case C

In the third case, the system parameters from Section 3.6 are used. The algorithm parameters are kept the same as for the first Case A. The same computational hardware is used as for the previous studies. Results are shown in Figs. 4.12 - 4.16.

Capacitor voltage waveform calculations are still similar with nearly 2 V difference in voltage ripple calculations which is 0.4% of the mean value. The arm currents predicted by the two simulations are similar. Total power loss calculated by high-speed simulation model is 2.79 kW as compared to 2.54 kW calculated by detailed simulation model. The high-speed simulation is nearly 200 times faster than detailed model.

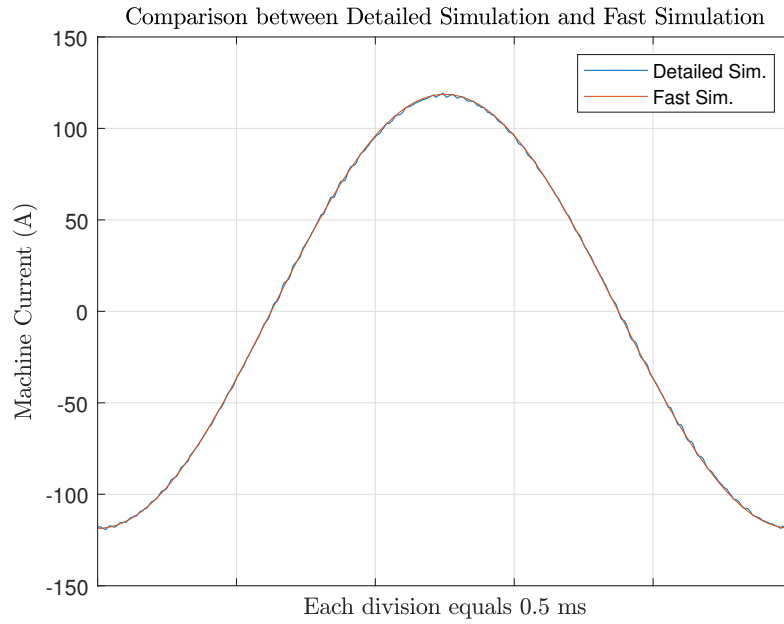


Fig. 4.12. Machine Current Comparison for Case C

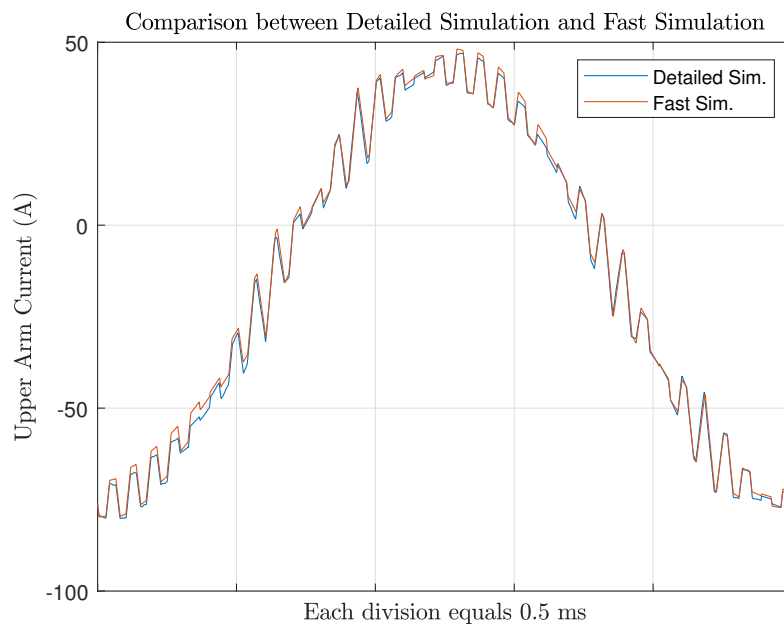


Fig. 4.13. MMC Upper Arm Current Comparison for Case C

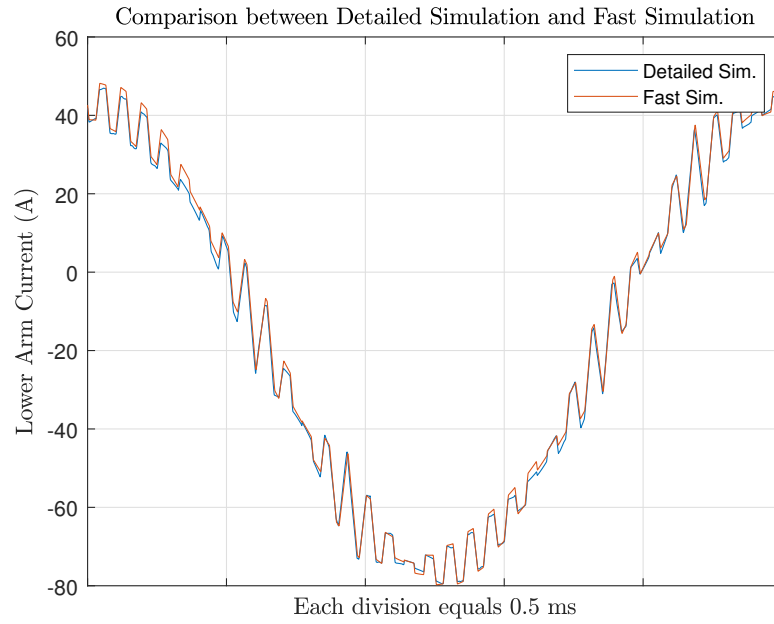


Fig. 4.14. MMC Lower Arm Current Comparison for Case C

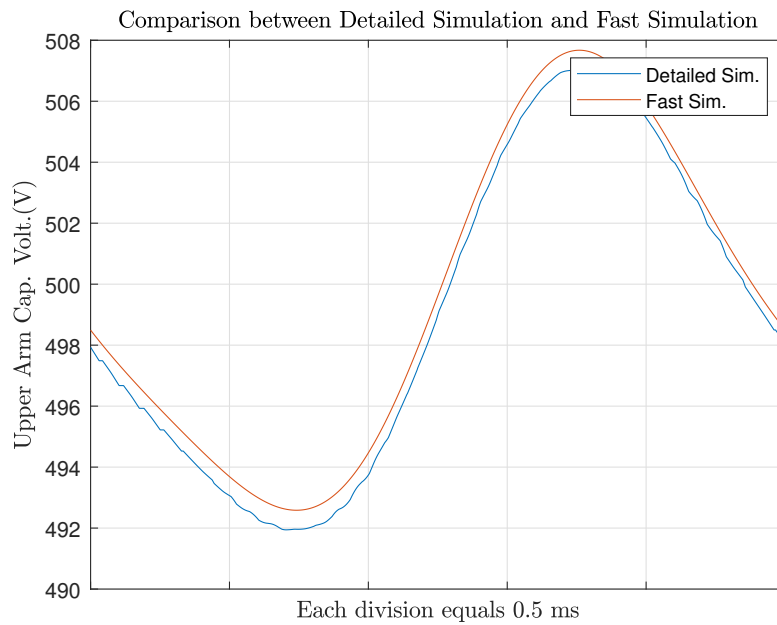


Fig. 4.15. MMC Upper Arm Submodule Capacitor Voltage Comparison for Case C

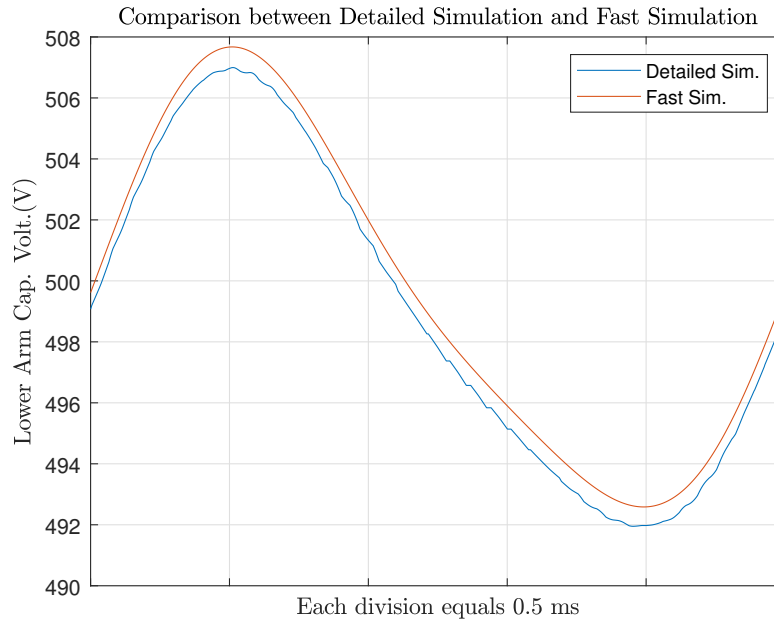


Fig. 4.16. MMC Lower Arm Submodule Capacitor Voltage Comparison for Case C

4.8 Conclusions

In this chapter, a high-speed simulation was presented, and its validation against a detailed simulation model (Chapter 3) has been set forth. It was shown that the simulation is suitable for an optimization environment due to its high-speed estimation of converter waveforms. It was also shown that the waveforms predicted by the high-speed simulation model are consistent with those predicted by the waveform-level model.

These estimated waveforms can be used for loss calculations and to impose system constraints in an optimization based design environment, which will benefit the system designer to explore trade-offs between mass and loss or volume and loss of the MMC components.

5. SUBMODULE POWER LOSSES AND THERMAL MODEL

A metamodel for the electric generator and a simulation model for PMAC-MMC system have been described in previous chapters. In this chapter MMC losses and thermal performance are considered. First, the loss generated in submodule semiconductor devices are modeled. Next, a submodule heat sink is described to dissipate the generated losses and maintain the semiconductor device junction temperatures. Finally, from the loss and heat sink models, a thermal model of the submodule is developed.

The high-speed simulation model utilizes an iterative solver to solve the machine currents, as shown in Fig. 4.1. To create a multi-objective optimization based PMAC-MMC design paradigm, it is realized that the optimization engine can be utilized to solve the loss calculation problem for the MMC, with every iteration of the optimization engine reaching towards the accurate solution of the machine currents. Hence, the non-linear iterative loop described in Chapter 4 can be broken.

Avoidance of an iterative use of the high-speed simulation allows inclusion of more detailed semiconductor and passive device loss calculation models, and in turn a submodule thermal model in design optimization. In next subsections, loss and thermal models for the considered submodule are described.

5.1 MMC Semiconductor Losses

This section describes the semiconductor loss models utilized to find the MMC arm submodule losses. These will be used in subsequent chapters for the development of a formal multi-objective optimization based design paradigm.

5.1.1 Conduction Losses in Semiconductor Devices

Semiconductor devices are characterized using their $I - V$ characteristics. To this end, the voltage drop across a semiconductor device, as a function of its current, is given as

$$V_{cd,\psi}(t) = \alpha_\psi + \beta_\psi I_\psi(t)^{n_\psi} \quad (5.1)$$

where $\psi \in \{‘d’, ‘s’\}$ denotes diode and switch, $V_{cd,\psi}(t)$ is the conducting device voltage drop and I_ψ is the current through the device at time t , and $\alpha_\psi, \beta_\psi, n_\psi$ are fitted parameters found using the device datasheet. The instantaneous conduction power loss in the device $P_{cd,\psi}$ can be expressed

$$P_{cd,\psi}(t) = \alpha_\psi I_\psi(t) + \beta_\psi I_\psi(t)^{n_\psi+1} \quad (5.2)$$

In this work, it is assumed that the dominant conduction losses are due to the DC and fundamental components of the MMC arm current. Table 5.1 and Fig. 5.1 list the device status based on the direction of the current and the submodule ON/OFF status with reference to submodule shown in Fig. 3.2. For submodule OFF state: either the top two or the bottom two devices can be turned ON to bypass the capacitor, which is shown in Table 5.1 as Case 1 and 2, respectively. During the OFF condition, there is always one diode and one switch conducting in a submodule. In Fig. 5.1, submodule OFF condition, red and green colors show alternate paths of conduction based on the devices turned on to bypass the capacitor, as listed in Table 5.1.

Using the device conduction status and switching signal for each submodule, the total conduction losses in an MMC arm can be calculated as the temporal average of the total instantaneous MMC arm conduction loss. Hence the time-average conduction losses in upper a -phase MMC arm can be expressed

$$P_{cd,up} = f_r \int_0^{f_r^{-1}} (N_{sm,up,off}(t)(P_{cd,d}(t) + P_{cd,s}(t)) + N_{sm,up,on}(t)P_{cd,up,on}(t))dt \quad (5.3)$$

Table 5.1.
Semiconductor Device Conduction Status

Submodule Status	Current	Devices Conduct
ON	$i_{sm} > 0$	D1 & D4
	$i_{sm} < 0$	S1 & S4
OFF	$i_{sm} > 0$	Case 1:D1 & S3
		Case 2:S2 & D4
	$i_{sm} < 0$	Case 1:S1 & D3
		Case 2:D2 & S4

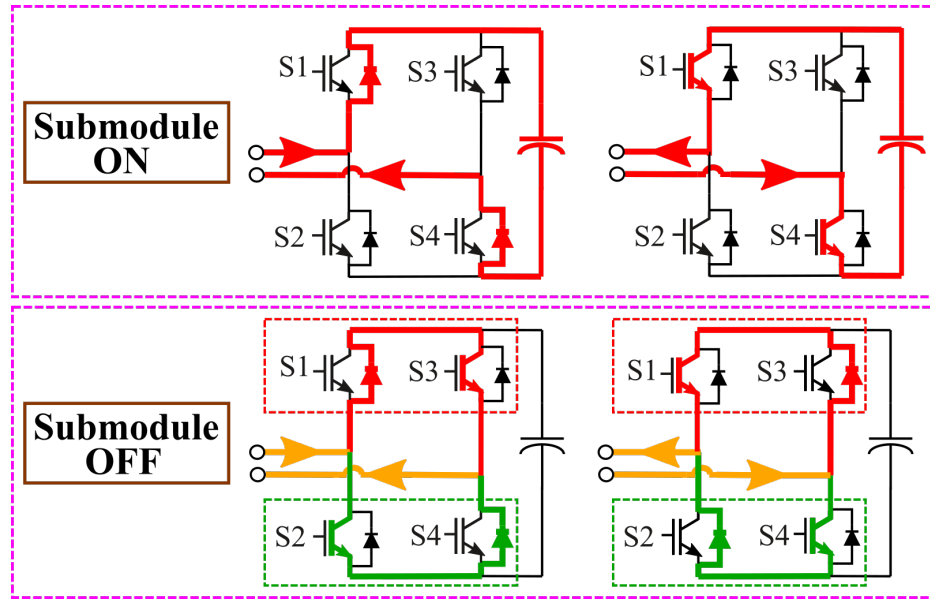


Fig. 5.1. Semiconductor Devices Conduction Status

where

$$P_{cd,up,on}(t) = \begin{cases} 2P_{cd,d}(t) & i_{a,up} > 0 \\ 2P_{cd,sw}(t) & i_{a,up} < 0 \end{cases} \quad (5.4)$$

and where f_r is the fundamental frequency, and $N_{sm,up,off}(t)$ and $N_{sm,up,on}(t)$ are number of submodules turned OFF and ON, respectively, at an instant t in upper

a -phase MMC arm, and $i_{a,up}$ is the MMC arm current. The total MMC conduction losses are calculated as 6 times the losses in the upper a - phase MMC arm.

5.1.2 Switching Losses in Semiconductor Devices

Switching losses in a submodule are based on the device data-sheet switching loss data. It is assumed that an individual semiconductor switching energy loss varies such that [46]

$$E_{sw,\xi} = E_{sw,\xi,r} V_{dc} |i_{sw}| / (N V_{sw,r} I_{sw,r}) \quad (5.5)$$

where

$$\xi \in \{\text{'on'}, \text{'off'}, \text{'rr'}\} \quad (5.6)$$

to denote the switch turn-on loss, switch turn off loss, and diode reverse recovery energy loss, respectively.

In (5.5) $E_{sw,\xi,r}$ is the loss at rated voltage $V_{sw,r}$ and rated current $I_{sw,r}$, and $E_{sw,\xi}$ is the estimated energy loss at submodule DC voltage V_{dc}/N and device current i_{sw} at the switching instant. Using the assumed variation of switching losses in switches, data at rated conditions will be taken from data-sheet and will be normalized by dividing by the rated switch voltage and current at which the switching loss data is provided.

To calculate the MMC switching losses, it is assumed that the switching losses in all the MMC arms are equal, and hence consideration of one phase arm is sufficient. Note that the capacitor voltage balancing technique utilized in MMCs to balance the submodules voltages [6] causes additional switching losses due to turn-on and turn-off of submodules. However, in this work, this additional switching loss is neglected. From Fig. 3.1 and 3.2, the mean DC voltage across the H-bridge is approximately V_{dc}/N . Within a switching cycle, Fig. 5.2 shows the instants where semiconductor device exhibits switching losses. Irrespective of the direction of the current, for one switching period, there will always be one switch that turns on under load, one switch

that turns off under load, one diode that turns on under load and one diode that turns off under load.

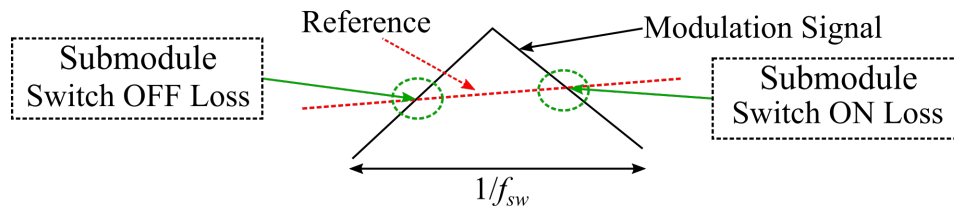


Fig. 5.2. Switching Loss Instants in a Switching Period

Table 5.2 and Fig. 5.3 shows the devices (with respect to Fig. 3.2) which can possibly produce switching ON and OFF losses based on current direction in one switching period. Green and red shaded devices in Fig. 5.3 show possible devices exhibiting switching losses (as shown in Table 5.2). Hence in a switching period, one diode reverse recovery, one switch turn ON and one switch turn OFF losses are generated.

Table 5.2.
Devices exhibiting switching loss in switching cycle

Current at switching event	Turn ON & Turn OFF Loss
$i_{sm} > 0$	Case 1: D1 & S2
	Case 2: S3 & D4
$i_{sm} < 0$	Case 1: S1 & D2
	Case 2: D3 & S4

Neglecting diode turn on energy loss, assuming nearly constant MMC arm current at both instants in a switching cycle, total energy loss can be calculated in a switching time period as

$$E_{sw,k} = (E_{sw,on,r} + E_{sw,off,r} + E_{sw,rr,r}) \frac{V_{dc}|i_{arm}[k]|/N}{V_{sw,r}I_{sw,r}} \quad (5.7)$$

where $E_{sw,k}$ is total switching energy loss in that switching time period; $E_{sw,on,r}$, $E_{sw,off,r}$ and $E_{sw,rr,r}$ are rated switch on, switch off and diode reverse recovery losses

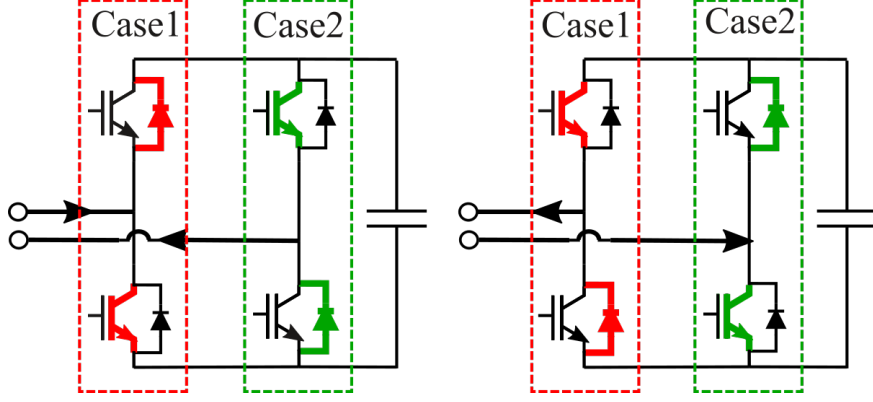


Fig. 5.3. Devices Exhibiting Switching Loss in Switching Period

respectively; and $i_{arm}[k]$ is MMC arm current in that switching time period. Total switching energy in one fundamental can be calculated as

$$E_{sw} = \sum_{k=1}^{N_{scpf_c}} E_{sw,k} = (E_{sw,on,r} + E_{sw,off,r} + E_{sw,rr,r}) \frac{V_{dc}/N}{V_{sw,r} I_{sw,r}} \sum_{k=1}^{N_{scpf_c}} |i_{arm}[k]| \quad (5.8)$$

where N_{scpf_c} is number of switching cycles in one fundamental cycle. N_{scpf_c} is assumed to be an integer. Switching power loss in the fundamental cycle can be calculated as

$$P_{sw} = E_{sw} f_r = E_{swC} N_{scpf_c} f_r \sum_{k=1}^{N_{scpf_c}} \frac{|i_{arm}[k]|}{N_{scpf_c}} \quad (5.9)$$

where

$$E_{swC} = (E_{sw,on,r} + E_{sw,off,r} + E_{sw,rr,r}) \frac{V_{dc}/N}{V_{sw,r} I_{sw,r}} \quad (5.10)$$

Upon close observation of (5.9), the summation is the average value of the absolute value of MMC arm currents. If switching frequency is much higher than the fundamental frequency, (5.9) can be expressed as

$$P_{sw} = E_{sw} f_r = E_{swC} f_{sw} f_r \int_0^{f_r^{-1}} |i_{arm}(t)| dt \quad (5.11)$$

where $f_r \int_0^{f_r^{-1}} |i_{arm}(t)| dt$ is the average of absolute value of arm current. Assuming symmetry, power loss in one MMC arm is calculated by

$$P_{x,up,sw} = E_{swC} f_{sw} f_r \int_0^{f_r^{-1}} |i_{x,up}(t)| dt \quad (5.12)$$

where waveform $i_{x,up}$ is taken from the high-speed simulation model.

5.2 Semiconductor Loss Dissipation in Submodule

The semiconductor device losses must be dissipated to avoid overheating. Hence, the PMAC-MMC design paradigm should include the consideration of the heat sink. Typically, natural or forced convection heat transfer mechanisms are considered for the heat sink design, and heat radiation and conduction are neglected. For high-power applications, relatively higher losses in semiconductor devices are expected, and hence a forced convection heat transfer is appropriate. Hence, forced convection based heat sink is considered in this work.

5.2.1 Forced Convection Heat Sink

A typical parallel plate fin heat sink structure is shown in Fig. 5.4. Air is forced through the fins to increase thermal transfer which reduces heat sink size. The structural parameter of the heat sink are shown in Fig. 5.4 except support plate thickness (shown as bottommost dark grey region) which is b_{pt} . The number of fins is denoted by n .

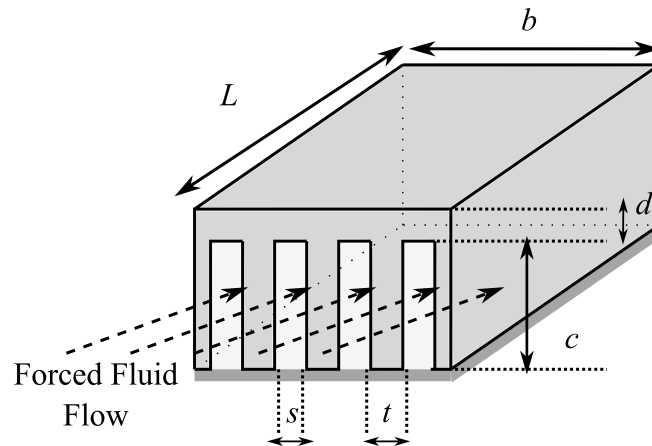


Fig. 5.4. Structure of Parallel Plate Fin Heat Sink

One approach to consider heat sink is by including a detailed analysis of the heat sink to calculate its thermal resistance and mass for every design evaluation. However, this leads to additional computational burden. Another approach is to develop a heat sink metamodel, similar to electric generator metamodel shown in Chapter 2. Metamodel based approach poses a significantly reduced computational burden on a system optimization problem and hence, will be undertaken herein.

It is desired to develop a heat sink metamodel such that the parameters of interest can be calculated for a required heat sink thermal resistance, $R_{th,S-a}$, as a continuous function of $R_{th,S-a}$. Parameters of interest in this work are: a) heat sink mass, M_{hd} , and b) input power to the heat dissipating fan, P_{fan} . This necessitates development of optimal heat sink design method, and use of the numerical results to develop the heat sink metamodel, similar to the procedure shown for generator in Chapter 2.

Primary contribution of this work towards consideration of heat sinks is development of a forced convection heat sink metamodel using heat sink design equations from literature (at [47]) integrated in a multi-objective optimization procedure [7,46]. For convenience, the design equations for the heat sink model are presented next.

Heat Transfer Design Equations and Thermal Resistance

As mentioned, formulation of the heat transfer mechanism described in [47] for the considered problem is utilized to develop the heatsink metamodel. An equivalent thermal circuit per fin gap is shown in Fig. 5.5 [47]. In the figure, $R_{th,d}$, $R_{th,b-a}$, $R_{th,fin}$ and $R_{th,fin-a}$ are equivalent thermal resistances of base plate, base plate to air, fin and fin to air, respectively. $P_{loss,sm}$ is time-average uniformly distributed heat source observed by the heat sink base plate, and a factor of $1/n$ calculates equivalent source per fin gap.

Solving the thermal equivalent circuit, the thermal resistance of heat sink $R_{th,S-a}$ can be expressed as

$$R_{th,S-a} = R_{th,d} + \frac{(R_{th,fin} + R_{th,fin-a})R_{th,b-a}}{n(R_{th,fin} + R_{th,fin-a} + 2R_{th,b-a})} \quad (5.13)$$

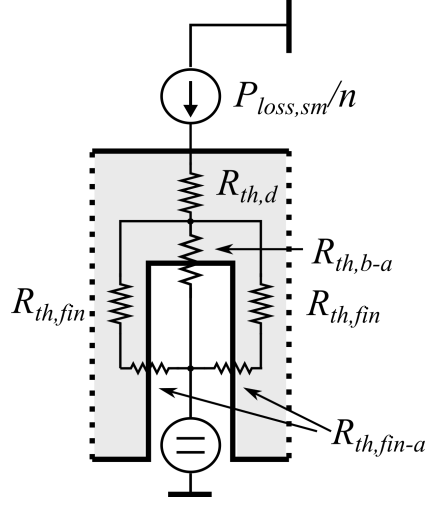


Fig. 5.5. Equivalent Thermal Circuit of Heat Sink per Fin Gap

The equivalent thermal resistance of the convection heat transfer $R_{th,eq}$ is defined as

$$R_{th,eq} = \frac{(R_{th,fin} + R_{th,fin-a})R_{th,b-a}}{n(R_{th,fin} + R_{th,fin-a} + 2R_{th,b-a})} \quad (5.14)$$

Assuming that the flow of the air in heat sink remains laminar, the calculation of the the thermal resistance terms in (5.13) begins with the calculation of the spacing between fins of the heat sink s which can be calculated as

$$s = \frac{b - (n + 1)t}{n} \quad (5.15)$$

The hydraulic diameter of the heat sink d_h is calculated in [47] as

$$d_h = \frac{2sc}{(s + c)} \quad (5.16)$$

The parameters ϵ_h for the heat sink is defined as

$$\epsilon_h = \begin{cases} \frac{c}{s} & s \geq c \\ \frac{s}{c} & s < c \end{cases} \quad (5.17)$$

The friction factor Reynolds product function $fRe_{\sqrt{A}}$ may be expressed

$$fRe_{\sqrt{A}} = \left[\frac{11.8336\dot{V}}{Ln\nu_{fl}} + (fRe_{\sqrt{A},fd})^2 \right]^{0.5} \quad (5.18)$$

with $fRe_{\sqrt{A},fd}$ is the friction factor Reynolds product for fully developed flow given by

$$fRe_{\sqrt{A},fd} = \frac{12}{\sqrt{\epsilon_h}(1 + \epsilon_h) \left[1 - \frac{192}{\pi^5} \epsilon_h \tanh\left(\frac{\pi}{2\epsilon_h}\right) \right]} \quad (5.19)$$

which represents the effect of the boundary layer velocity profile on the mass transfer, as described in [47]. In (5.18), \dot{V} is the volume flow rate and ν_{fl} is the kinematic viscosity of air.

Next, sudden expansion and contraction friction factors, K_{se} and K_{sc} respectively, are calculated as [47]

$$K_{se} = \left(1 - \left(1 - \frac{(n+1)t}{b} \right)^2 \right)^2 \quad (5.20)$$

$$K_{sc} \approx 0.42 \left(1 - \left(1 - \frac{(n+1)t}{b} \right)^2 \right) \quad (5.21)$$

Using conservation of momentum, the pressure drop due to friction-less acceleration of air, $\Delta p_{acc}(\dot{V})$, is given by

$$\Delta p_{acc}(\dot{V}) = \left(\frac{1}{(nsc)^2} - \frac{1}{b^4} \right) \frac{\rho}{2} \dot{V}^2 \quad (5.22)$$

The pressure drop due to heat sink friction $\Delta p_{hs}(\dot{V})$ is calculated as

$$\Delta p_{hs}(\dot{V}) = \left(\frac{n\nu_{fl}\sqrt{cs}}{\dot{V}} \frac{L}{d_h} fRe_{\sqrt{A}}(\dot{V}) + K_{se} + K_{sc} \right) \frac{\rho}{2} \left(\frac{\dot{V}}{nsc} \right)^2 \quad (5.23)$$

Finally, total air pressure drop in the heat sink is given by

$$\Delta p_{tot}(\dot{V}) = \Delta p_{hs}(\dot{V}) + \Delta p_{acc}(\dot{V}) \quad (5.24)$$

This completes the fluid dynamics analysis of the heat sink.

Next, the analysis of heat sink convection heat transfer are presented using [47]. To this end, the uniform wall temperature function $f(\text{Pr})$ for a given Prandtl number Pr is given by

$$f(\text{Pr}) = \frac{0.564}{\left[1 + \left(1.664\text{Pr}^{\frac{1}{6}} \right)^{\frac{9}{2}} \right]^{\frac{2}{9}}} \quad (5.25)$$

Blending parameter m and shape function z^* are defined as

$$m = 2.27 + 1.65\text{Pr}^{\frac{1}{3}} \quad (5.26)$$

$$z^* = \frac{Ln\nu_{fl}}{\text{Pr}\dot{V}} \quad (5.27)$$

Next, the Nusselt number $\text{Nu}_{\sqrt{A}}$, used to calculate average heat transfer coefficient h_{tf} , is given by

$$\text{Nu}_{\sqrt{A}} = \left[\left(\frac{C_4 f(\text{Pr})}{\sqrt{z}} \right)^m + \left(\left\{ \frac{C_1 f \text{Re}_{\sqrt{A}}}{8\sqrt{\pi}\epsilon_h^\gamma} \right\}^5 + \left\{ C_2 C_3 \left(\frac{f \text{Re}_{\sqrt{A}}}{z^*} \right)^{\frac{1}{3}} \right\}^5 \right)^{\frac{m}{5}} \right]^{\frac{1}{m}} \quad (5.28)$$

where $C_1 = 3.24$, $C_2 = 1.5$, $C_3 = 0.409$, $C_4 = 2$ and $\gamma = -0.3$ as given in [47]. The coefficient h_{tf} is calculated as

$$h_{tf} = \frac{\text{Nu}_{\sqrt{A}} \lambda_{fl}}{d_h} \quad (5.29)$$

where λ_{fl} is the thermal conductivity of air.

The heat transfer efficiency of fin is given by

$$\eta_{fin} = \frac{\tanh \left(c \cdot \sqrt{\frac{2h_{tf}(t+L)}{\lambda_{hs}tL}} \right)}{c \cdot \sqrt{\frac{2h_{tf}(t+L)}{\lambda_{hs}tL}}} \quad (5.30)$$

where λ_{hs} is the thermal conductivity of heat sink material.

Finally, the equivalent thermal resistance of convection heat transfer is expressed using [47] as

$$R_{th,eq} = \frac{1}{\rho_{fl} c_{fl} \dot{V} \left(1 - \exp \left(-\frac{h_{tf} n (2cn + s)L}{\rho_{fl} c_{fl} \dot{V}} \right) \right)} \quad (5.31)$$

where ρ_{fl} and c_{fl} are the density and thermal capacitance of air, respectively. The equivalent thermal resistance of the base plate $R_{th,d}$ can be readily expressed as

$$R_{th,d} = \frac{d}{bL\lambda_{hs}} \quad (5.32)$$

using which the total thermal resistance of the heat sink can be calculated.

Solution of Design Equations

The solution of heat sink design equations is a non-linear problem where volume flow rate of air \dot{V} is solved such that the external pressure drop applied by a fan Δp_{fan} equals to pressure drop in heat sink. That is

$$\text{Solve } \left\{ \dot{V} \ni' \left(\Delta p_{tot}(\dot{V}) = \Delta p_{fan}(\dot{V}) \right) \right\} \quad (5.33)$$

For a fan, the pressure drop characteristics as a function of \dot{V} is assumed to be of the form [48]

$$\Delta p_{fan}(\dot{V}) = -\frac{\Delta p_{fan,max}}{\dot{V}_{max}} \dot{V} + \Delta p_{fan,max}, \quad \dot{V} \in [0, \dot{V}_{max}] \quad (5.34)$$

where $\Delta p_{fan,max}$ and \dot{V}_{max} are maximum allowed pressure drop and air flow rate, respectively, for the fan found using fan datasheet. Circular cross-sectional fans are considered in this work. For a given fan diameter, D_f and revolution speed in rpm f_{rpm} , \dot{V}_{max} , $\Delta p_{fan,max}$ and fan power P_{fan} are curve fitted as [48]

$$\dot{V}_{max} = k_{1f} f_{rpm} D_f^3 \quad (5.35)$$

$$\Delta p_{fan,max} = k_{2f} f_{rpm}^2 D_f^2 \quad (5.36)$$

$$P_{fan} = k_{3f} f_{rpm}^3 D_f^5 \quad (5.37)$$

Hence, for a given fan and heat sink geometry, (5.15)-(5.37) have to be simultaneously solved till equality of (5.33) is achieved to calculate the thermal resistance of the heat sink using (5.13), (5.14), (5.31) and (5.32).

Heat Sink Optimization

The development of heat sink metamodel requires optimal heat sink designs as a function of the required thermal resistance. This requires minimum possible thermal resistance for a given mass with available fan power.

Recall that for the heat sink thermal resistance calculation, set of non-linear equations need to be solved. In this work, an optimization based solution scheme will be

utilized. That is, an initial guess of \dot{V} will be guessed, and using the (5.15)-(5.37), the pressure drop applied by fan, $\Delta p_{fan}(\dot{V})$, and the actual heat sink pressure drop, $\Delta p_{tot}(\dot{V})$ are calculated. Next, constraints are imposed such that

$$\dot{V} \leq \dot{V}_{max} \quad (5.38)$$

$$P_{fan} \leq P_{fan,max} \quad (5.39)$$

$$0 \leq \frac{\Delta p_{fan} - \Delta p_{tot}}{\Delta p_{tot}} \leq \alpha_{f,e} \quad (5.40)$$

where $P_{fan,max}$ is the maximum fan power available and $\alpha_{f,e}$ limits the maximum deviation from equality of solution. Equations (5.38) and (5.39) limit the maximum air flow rate and the fan power of the solution, respectively, whereas (5.40) ensures that the pressure drop generated by the fan is greater than the actual pressure drop in heat sink. At the end of the optimization, a minimum heat sink mass achieves the equality of (5.33) to reduce the additional fan mass.

Design variables considered for this optimization are stored in vector \mathbf{T} as

$$\mathbf{T} = [b \quad d \quad L \quad n \quad t \quad \dot{V} \quad f_{rpm}] \quad (5.41)$$

In this formulation, the height of fin c is taken equal to heat sink width b . By design, the diameter of the fan D_f is equal to the width of the heat sink.

Along with (5.38)-(5.40), an additional constraint is imposed on the heat sink geometry so as to achieve feasible designs. It is required that minimum gap between two fins is greater than s_{min} . That is

$$b - (n + 1)t \geq s_{min} \quad (5.42)$$

After all the constraints have been satisfied, heat sink thermal resistance $R_{th,S-a}$ is calculated using (5.13), (5.14), (5.31) and (5.32). Next, mass calculation of the heat dissipation system is undertaken. Mass of the heat sink can be calculated as volume of the material utilized times the mass density. That is,

$$M_{hs} = (tc + (d + b_{pt})(s + t)) nL\rho_{hs} \quad (5.43)$$

Mass of the fan is assumed to vary linearly with its power requirement such as

$$M_{fan} = \frac{P_{fan}}{\rho_{pf}} \quad (5.44)$$

where ρ_{pf} is the constant specific power density in W/kg of the fan. Note that by assuming a linear relation between fan mass and its power requirement, a reduction in fan mass also leads to reduction in its power requirements, and hence minimizes the fan power. That is why fan power is not taken as one of the objective to be minimized.

Total mass of heat dissipation system can be computed as

$$M_{hd} = M_{hs} + M_{fan} \quad (5.45)$$

Finally, the objective/fitness function to be minimized is given by

$$f = \left[R_{th,S-a} \quad M_{hd} \right]^T \quad (5.46)$$

to achieve the optimal heat sink thermal resistance per unit mass.

For the development of heat sink metamodel, the considered design space is shown in Table 5.3. Parameter units have been indicated in the parenthesis. Parameter search space (except fan speed) in Table 5.3 is taken from [46] so as to compare the designed heat sinks to the natural convection heat sinks from [46]. Fan speed limits are found using [48].

Fixed design parameters are presented next. For this formulation, aluminum is taken as the heat sink material. Support plate thickness b_{pt} is taken equal to 2 mm. Minimum channel width s_{min} is taken to be 2 mm from [46]. The material parameters are: $\lambda_{fl} = 0.03$ W/(m K), $\lambda_{hs} = 210$ W/(m K), $\nu_{fl} = 2.1 \cdot 10^{-5}$ m²/s, $\rho_{fl} = 1$ kg/m³, $\rho_{hs} = 2705$ kg/m³, $c_{fl} = 1.01 \cdot 10^3$ J/(kg K) and Prandtl number for air = 0.71. From [47, 48], the fan parameters are found as $k_{1f} = 10^{-3}$, $k_{2f} = 6 \cdot 10^{-4}$ and $k_{3f} = 20 \cdot 10^{-6}$ for fan diameter $D_f \in [40, 200]$ mm, fan speed $f_{rpm} \in [1500, 15000]$ rpm and maximum fan power $P_{fan,max} = 25$ W. Value of $\alpha_{f,e}$ in (5.39) is taken equal to 0.02. The specific power density of the fan ρ_{pm} is taken equal to 0.2 W/g.

Table 5.3.
Heat Sink Design Search Space

Parameter	Minimum	Maximum
b (mm)	50	200
d (mm)	2	10
L (mm)	50	200
n	2	1e3
t (mm)	1	5
\dot{V} (m ³ /s)	10 ⁻¹⁵	1
f_{rpm} (rpm)	1500	15000

At this point, any compatible optimization engine can be utilized. In this work, genetic algorithm based GOSET will be used [7]. The procedure to formulate a compatible fitness function for GOSET is described in [7]. Results of the multi-objective optimization study is shown in Figs. 5.6-5.8.

Fig. 5.6 shows the Pareto-optimal front of the heat sink design, and is compared against natural convection heat sink as shown in 5.6. Fig. 5.7 presents the heat sink dimensions and Fig. 5.8 shows the required fan power for the cooling. For most of the mass range in Fig. 5.6, the forced air cooled works better than natural convection except at mass below 40 g, as shown in zoomed portion of figure. The number of fins used are two in the low mass region between 30-40 g, and width and fin height is limited to lowest possible value of 50 mm, as shown in Fig. 5.7. This means that in this low mass region, using a fan is not optimal as the fin gap is large which causes major portion of the heat to be dissipated via natural convection. In that region, the fan is only adding to the mass of heat dissipation system.

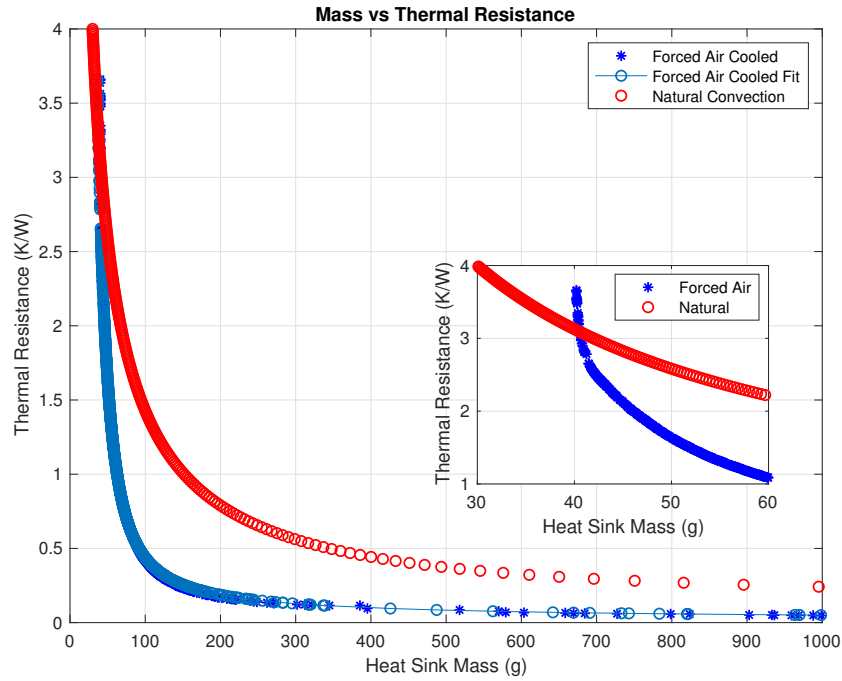


Fig. 5.6. Pareto-optimal Front of the Design

5.2.2 Heat Sink Metamodel

Finally, a heat sink metamodel is used to estimate the heat sink mass (in kg) as a function of thermal resistance. The assumed form is given by:

$$M_{hd,c} = \frac{\alpha_{hs}}{(R_{th,S-a})^{n_{1h}}} + \frac{\beta_{hs}}{(R_{th,S-a})^{n_{2h}}} \quad (5.47)$$

Similarly, the fan power required as a function of thermal resistance is represented using

$$P_{fan,c} = \frac{\alpha_f}{(R_{th,S-a})^{n_{1f}}} + \frac{\beta_f}{(R_{th,S-a})^{n_{2f}}} \quad (5.48)$$

The metamodel parameters representing the data in Fig. 5.6 are shown in Table 5.4. The metamodel estimate of mass and fan power are shown in fit for mass and fan power are shown in Fig. 5.6 and 5.9, respectively.

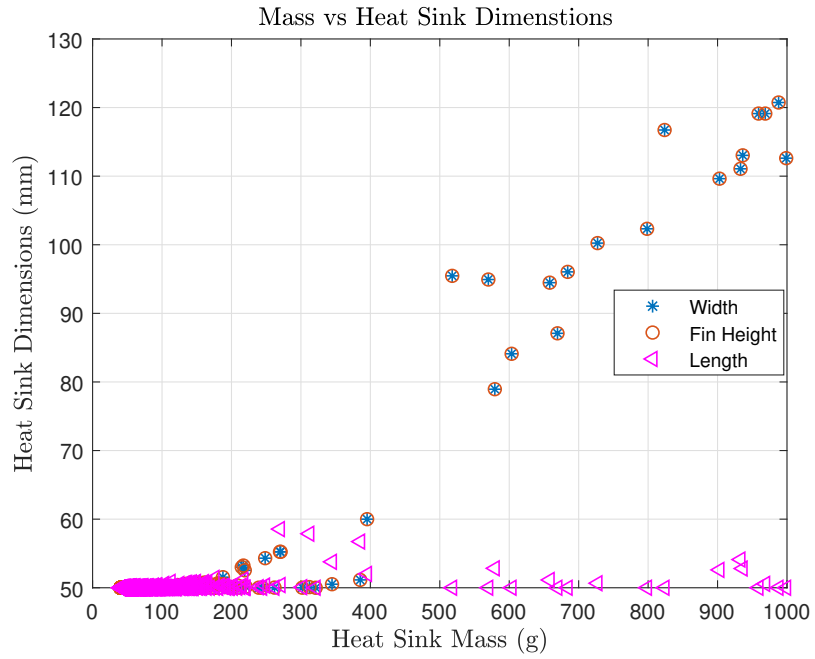


Fig. 5.7. Heat Sink Dimensions vs Heat Sink Mass

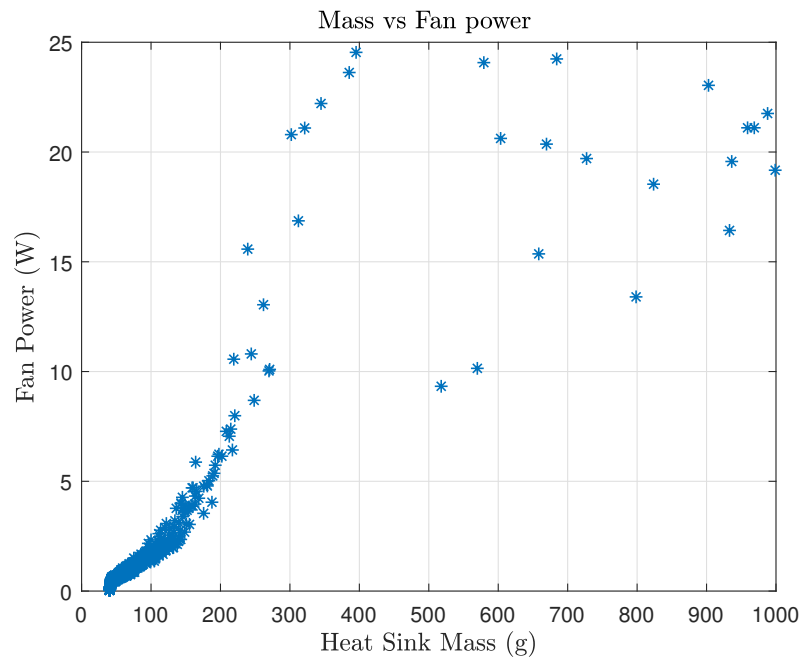


Fig. 5.8. Fan Power vs Heat Sink Mass

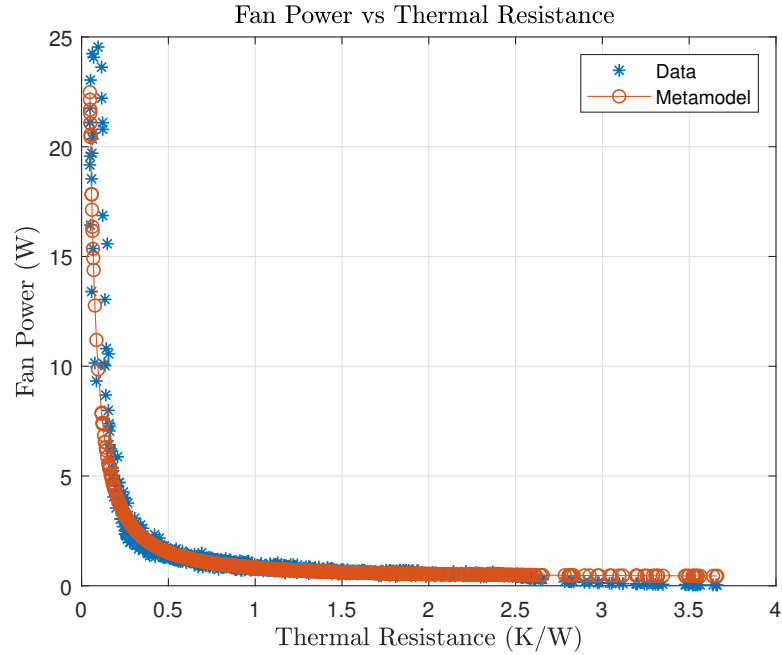


Fig. 5.9. Fan power vs Thermal Resistance

Table 5.4.
Heat Sink Metamodel Parameters

Parameter	Value	Parameter	Value
α_{hs}	$6.33 \cdot 10^{-3}$	n_{1h}	1.63
β_{hs}	$56.28 \cdot 10^{-3}$	n_{2h}	0.36
α_f	0.5645	n_{1f}	1.209
β_f	0.2545	n_{2f}	-0.1992

5.3 Submodule Thermal Model

Using the semiconductor device loss models and heat sink metamodel, a thermal model of the submodule can be developed. This thermal model calculates least required heat sink mass and fan power so as to maintain the junction temperature of the devices under their rated limits.

It is assumed that all the submodule semiconductor devices are placed on a single heat sink with a heat source uniformly spread over the surface. Next, from Tables 5.1 and 5.2, it is observed that for reference submodule in Fig. 3.2, devices $D1$ & $D4$ exhibit similar losses and can be coupled as single heat source. Similarly, the pairs $D2$ & $D3$, $S1$ & $S4$ and $S2$ & $S3$ can be coupled as single source on heat sink. To this end, time and submodule average power loss source using $D1$ & $D4$ for a -phase upper arm submodule can be expressed

$$P_{d14} = \frac{1}{N} \sum_{k=1}^N (P_{cd,D1,k} + P_{sw,D1,k} + P_{cd,D4,k} + P_{sw,D4,k}) \quad (5.49)$$

where $P_{cd,D1,k}$ and $P_{cd,D4,k}$ are total time-average conduction, respectively, and $P_{sw,D1,k}$ and $P_{sw,D4,k}$ are total time-average switching losses, respectively, in diode $D1$ and $D2$ in upper a -phase arm submodule k . Similar expression can be written for other diodes and switches. Based on the assumption, semiconductor loss calculations in Section 5.1, Tables 5.1 & 5.2, and (5.49), a thermal equivalent circuit can be formulated as shown in Fig. 5.10 wherein $R_{th,s-hs}$ and $R_{th,d-hs}$ are thermal resistance between junction to case, and $T_{j,s}$ and $T_{j,d}$ are junction temperatures of switch and diode, respectively. T_{amb} is the ambient temperature. The factor of half in device thermal resistances denotes two loss sources combined in parallel.

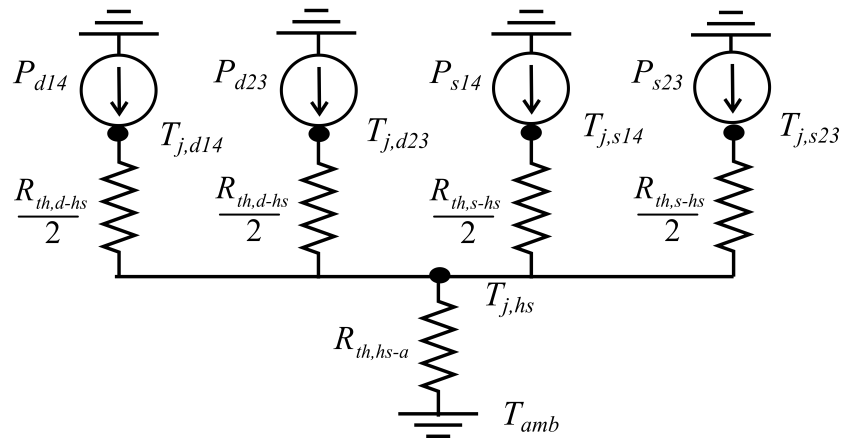


Fig. 5.10. Equivalent Thermal Model Circuit for Submodule

For a given maximum allowed switch and diode junction temperature temperature, $T_{j,s,max}$ and $T_{j,d,max}$, respectively, required thermal resistance $R_{th,hs-a}$ can be calculated as

$$R_{th,hs-a} = \min(R_{hs,\psi\chi}, \psi \in \{‘d’, ‘s’\}, \chi \in \{‘14’, ‘23’\}) \quad (5.50)$$

$$R_{hs,\psi\chi} = \frac{T_{j,\psi,max} - T_{amb} - 0.5P_{\psi\chi}R_{th,\psi-hs}}{(P_{d14} + P_{d23} + P_{s14} + P_{s23})} \quad (5.51)$$

for which minimum required heat sink mass M_{hs} for a submodule can be calculated using metamodel (5.47). Similarly, required submodule fan power $P_{f,hs}$ can be calculated using (5.48). Power consumed by heat sink fans will be accounted in the total system loss in Chapter 7.

This chapter presented the design equations and model/metamodel to be used for submodule loss and mass calculations. Work presented herein will be utilized in subsequent chapters to formulate a global multi-objective optimization problem.

6. PASSIVE DEVICES IN MODULAR MULTILEVEL CONVERTER

The MMC contains submodule capacitors and filter inductors. As described earlier, the filter inductors in the MMC arm reduce harmonic components in the arm currents whereas submodule capacitors act as a DC voltage source for the H-bridge converters. Models described herein will be utilized to calculate passive device loss and mass in each MMC arm.

6.1 Polypropylene Film Capacitor

A polypropylene film capacitor is considered in this work as electrolytic capacitors lose capacitance rapidly with frequency [22], [46]. To this end, the polypropylene capacitor mass is modeled as

$$M_C = \alpha_{cm} C_r (V_{c,r}/(V_{cm}))^{\gamma_{cm}} + \beta_{cm} \quad (6.1)$$

where C_r is the required capacitance, $V_{c,r}$ is the rated capacitor voltage, and $\alpha_{cm}, \beta_{cm}, \gamma_{cm}$ and V_{cm} are model parameters found using capacitor datasheets [49] and curve fitting techniques. Capacitor losses are calculated based on the Equivalent Series Resistance (ESR) of the capacitor. ESR for polypropylene capacitors is modeled as [22]

$$R_{C,esr} = (\alpha_{c,esr,1} (V_{c,esr,1}/V_{c,r})^{\gamma_{c,esr,1}})/C_r + (\alpha_{c,esr,2} (V_{c,esr,2}/V_{c,r})^{\gamma_{c,esr,2}})/C_r + \beta_{c,esr} \quad (6.2)$$

where $\alpha_{c,esr,1}, \alpha_{c,esr,2}, \beta_{c,esr}, \gamma_{c,esr,1}, \gamma_{c,esr,2}, V_{c,esr,1}$ and $V_{c,esr,2}$ are capacitor ESR model parameters based on capacitor datasheets.

For an MMC containing N submodules with capacitance C_{sm} and rated voltage $V_{c,r,sm}$

$$V_{c,r,sm} = \frac{V_{dc}}{N} \quad (6.3)$$

the individual submodule capacitor mass and ESR can be calculated using (6.1) and (6.2), respectively. From Chapters 3 and 4, it is known that all the capacitors in one phase arm of MMC observe similar voltage variation, and hence the same current waveforms. To calculate total time-average capacitor ESR loss in one MMC arm, the average loss is calculated for one submodule and the result is multiplied by number of submodules N . Similarly, capacitor mass for one submodule is calculated, and is multiplied by N to calculate the total capacitor mass in one MMC arm.

Hence, from (4.21), the ESR power losses in the a -phase upper arm submodule capacitors are computed using MMC submodule switching and current waveforms as

$$P_{C_{sm,esr}} = \frac{NR_{C_{sm,esr}}}{T} \int_0^T \sum_{i=1}^N \left(\frac{s_{i,a,up}(t)i_{a,up}(t)}{N} \right)^2 dt \quad (6.4)$$

where T is the fundamental time period, and $R_{C_{sm,esr}}$ is the submodule capacitor ESR.

For the DC bus capacitor of capacitance C_{in} in Fig. 3.1, the ESR $R_{C_{in}}$ and the mass $M_{C_{in}}$ can be estimated using polypropylene capacitor model as presented in (6.1) and (6.2) with $V_{c,r} = V_{dc}$. The total bus capacitor power losses due to the harmonic current component can be calculated using (4.41) as

$$P_{C_{in,esr}} = \frac{N_{cb}R_{C_{b,esr}}}{T} \int_0^T i_{cin,rip}(t)^2 dt \quad (6.5)$$

To achieve an anticipated capacitor life-time, the ESR losses must be bounded [22]. To this end, a thermal model of capacitor is utilized to calculate the change in capacitor temperature for the generated ESR losses. The change in capacitor temperature ΔT_c for ESR loss $P_{c,esr}$ is given by

$$\Delta T_c = R_{th,c-a} P_{c,esr} \quad (6.6)$$

where $R_{th,c-a}$ is the thermal resistance between the capacitor package and the ambient environment. For the capacitor series considered in the notional system, $R_{th,c-a}$ is modeled as [22]

$$R_{th,c-a} = 1/[\alpha_{g,c}(V_{c,r}/V_{bg})C_r^{\alpha_{g,a}} + \alpha_{g,c}(V_{c,r}/V_{bg})C_r^{\alpha_{g,a}} + \beta_{g,c}(V_{bg}/V_{c,r})C_r^{\beta_{g,a}} + \beta_{g,c}(V_{bg}/V_{c,r})C_r^{\beta_{g,a}}] \quad (6.7)$$

Using the calculated capacitor losses for submodule and DC bus, the change in temperature can be calculated using (6.7). Finally, constraints will be imposed on the optimization problem to limit the maximum change in submodule and DC bus capacitor temperature to achieve the desired lifetime.

In Chapter 7, a notional case study will be set forth. The capacitor model parameters for the notional example are obtained by curve fitting the data set forth for the VISHAY MKP1848C capacitor series [49]. The resulting capacitor model parameters are listed in Appendix B.

6.2 MMC Arm Inductor

As mentioned during the introduction of this research, it is desired to include the contribution of inductor mass and loss to the PMAC-MMC. The MMC arm inductor can substantially change the size of MMC. A high value of inductance leads to reduced harmonics in the arm currents and reduced harmonic losses. However, high inductance value can lead to a large and massive inductor. Typically arm inductors of each phase legs are independent. Herein, the impact of coupled inductors to reduce the inductor size is also considered.

Three-phase coupled inductors have been widely utilized for filtering in 3-phase systems [50, 51], impeding any differential mode harmonics in current. It is desired to investigate the performance of such coupled inductors in an MMC.

Referring to Chapter 3 equation (3.16), the circulating component of MMC arm current relates to the circulating arm voltage as

$$\begin{bmatrix} L_{s,i} & L_{m,i} & L_{m,i} \\ L_{m,i} & L_{s,i} & L_{m,i} \\ L_{m,i} & L_{m,i} & L_{s,i} \end{bmatrix} \mathbf{p}\mathbf{i}_{abc,ul} = \begin{bmatrix} v_{dc} \\ v_{dc} \\ v_{dc} \end{bmatrix} - (\mathbf{v}_{abc,up} + \mathbf{v}_{abc,low} + R_1 \mathbf{i}_{abc,ul}) \quad (6.8)$$

Applying rotor reference frame transformation \mathbf{K}_s^r to (6.8) using (3.5)-(3.8)

$$\begin{bmatrix} L_{q,i} & 0 & 0 \\ 0 & L_{d,i} & 0 \\ 0 & 0 & L_{0,i} \end{bmatrix} \mathbf{p}\mathbf{i}_{qd0,ul}^r = \begin{bmatrix} -\omega_r L_{d,i} i_{d,ul}^r \\ \omega_r L_{q,i} i_{q,ul}^r \\ v_{dc} \end{bmatrix} - (\mathbf{v}_{qd0,up}^r + \mathbf{v}_{qd0,low}^r + R_1 \mathbf{i}_{qd0,ul}^r) \quad (6.9)$$

where

$$L_{q,i} = L_{d,i} = L_{s,i} - L_{m,i} \quad (6.10)$$

$$L_{0,i} = L_{s,i} + 2L_{m,i} \quad (6.11)$$

and where $\mathbf{i}_{qd0,ul}$ is sum of $qd0$ upper and lower arm currents.

A typical 3-phase coupled inductor with small leakage inductance has mutual coupling between phases such that [50, 51]

$$L_{m,i} = -\frac{1}{2}L_{s,i} \quad (6.12)$$

Using (6.12) with (6.9)-(6.11), it can be readily observed that such 3-phase coupled inductors provide zero (or very little, considering leakage) inductance to the zero-sequence component of the current and the 3-phase inductor will be unable to filter any common-mode component in circulatory currents in the MMC arms.

To demonstrate the effect of using a 3-phase coupled inductor, a test study is undertaken with parameters from Chapter 3 Section 3.6. The MMC parameters are kept same except the arm inductor which is replaced with a symmetrical 3-phase Y-core inductor [51] with $L_{s,i}$ is 0.24 mH and $L_{m,i}$ is $-0.45L_{s,i}$ mH, such that $L_{q,i}$ and $L_{d,i}$ are 0.36 mH to match with self inductance from Section 3.6 study. However $L_{0,i}$, which is equal to $24 \mu H > 0$ (from (6.11)), is kept non-zero for stability reasons (as will be soon observed). A detailed waveform-level simulation is repeated to show the effects of the additional mutual coupling on common mode circulating current. Results from the simulation are shown in Figs. 6.1 and 6.2.

Comparing the Figs. 6.1 and 6.2 with Figs. 3.8 and 3.9, respectively, it is evident that even though the machine current is fairly similar in both the results, the common mode circulatory component of MMC arm current is substantially larger in Fig.

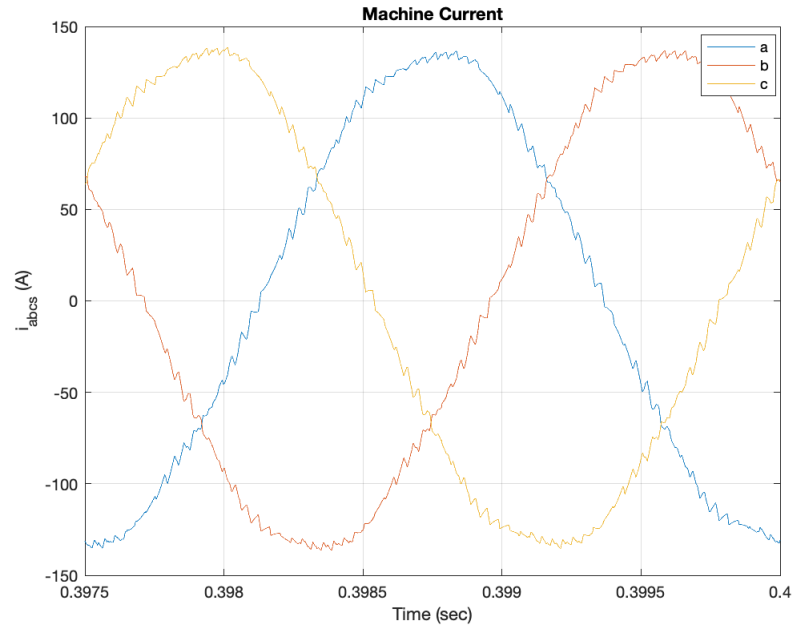


Fig. 6.1. MMC Machine Current for Modified Study from Chapter 3

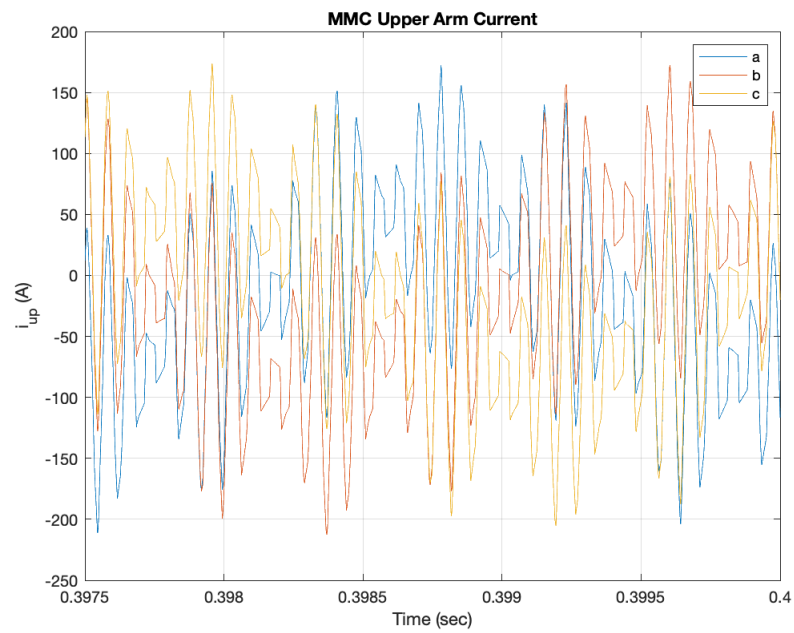


Fig. 6.2. MMC Upper Arm Current for Modified Study from Chapter 3

6.2 which confirms the aforementioned concern about low common mode inductance provided by coupled 3-phase inductor topologies. Using this conclusion, in this work, 3-phase inductor topologies (such as 3-phase symmetrical Y-core inductors) will not be further considered for the MMC and only single-phase inductor topologies will be studied.

Two different inductor topologies are considered in this work. They are: permanent magnet based single phase EE-core (denoted as EE-PMI in subsequent sections) and single phase EE-core. Studies will be conducted in subsequent chapter to compare the mentioned inductors for MMC optimization to compare the two topologies for the considered application. Next, the inductors, their geometry and analysis are described.

6.2.1 Permanent Magnet based E-E core Inductor

Studies in Chapter 3 and 4 indicate that the arm currents in the MMC contain DC component. Usually, this DC component in arm current is disadvantageous from a magnetic core perspective, it keeps a constant DC flux bias in the core and reduces the amplitude of AC flux in the core which can be used to avoid core saturation. This may lead to a larger magnetic core size and heavy inductors, as presented in [52, 53].

To overcome limitations due to DC flux, Permanent Magnet Inductors (PMI) have been proposed in literature for DC-DC converter applications [52, 53]. PMIs reduce the DC flux in the magnetic core by introducing a counter DC flux using a permanent magnet, thereby reducing the overall DC flux in the core. The inductor is designed such that at all required load conditions (including no-load), the core flux density is below the saturation level while simultaneously reducing the effect of DC component of winding flux to magnetic core. In this work, it is desired to include such PM based inductors as a filter to determine if they offer any advantages over standard inductor in MMC systems .

One of the design topology to introduce the permanent magnet is shown in Fig. 6.3 where the magnet flux is introduced in the main (center leg) flux path [52]. Though this PMI structure removes the DC bias from core, the permanent magnet also adds unnecessary airgap to main flux path. To avoid this, [52,53] present a flap based PMI where the permanent magnet is not added directly to the main flux path but on side legs which prevents additional airgap due to magnet as well as cancels the DC flux bias created by the winding current. The considered EE-core inductor in this work for MMC is based on similar design topology.

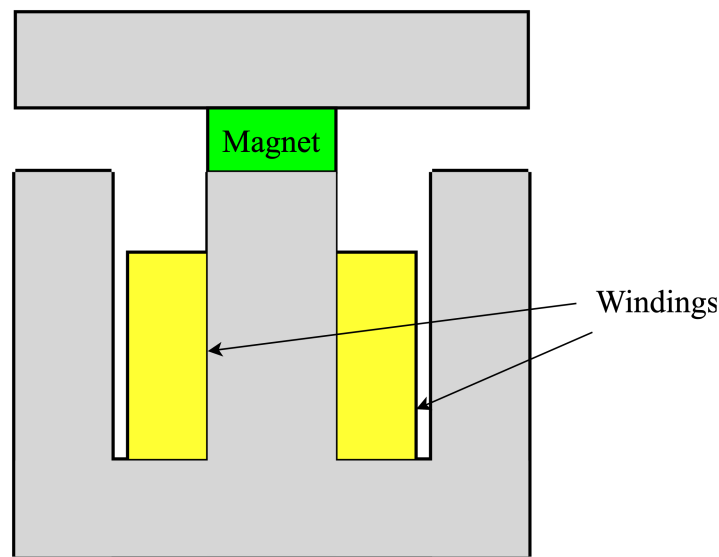


Fig. 6.3. EI-core PMI geometry

The nanocrystalline soft magnetic material based core, FINEMET, is investigated in this work as core material in a PMI [54]. FINEMET FT3-M based core has high relative permeability ($\sim 4 \cdot 10^4 - 6 \cdot 10^5$), low electrical conductivity, and $\sim 1.2 - 1.4$ T peak flux density limit for material saturation [54] which makes it a very good candidate for to be used as core material for inductors to be utilized in MMC applications. The core material is available as tape, shown in Fig. 6.4 [54], and hence cannot be cut into laminations/sheets. Hence, an E-E core geometry is considered, as shown in Fig. 6.5, manufactured using four U-cores of FINEMET material.



Fig. 6.4. Nanocrystalline Core Material [54]

In the EE-PMI geometry shown in Fig. 6.5, the magnetization direction of magnet (shown as green) is arranged such that they create a net flux opposing the DC flux generated by the windings (shown as yellow). To complete the path for magnet flux, two laminated steel plates are attached on each side of the EE-PMI. Note that the steel lamination direction is along the width of the inductor such that the flux through it is never orthogonal. The geometrical parameters of the inductor are shown in Fig.6.5 except the length of core (into the plane of paper) which is l_c . Note that the center leg air gap g_c is kept significantly less than the end leg air gap g_e to avoid undesired short circuiting of the magnet flux across the air gap at end legs. It is desired that most of the PM flux crosses through the center leg.

For this considered PMI topology, next, it is desired to calculate the flux linkage with respect to the current in the winding, so as to calculate the inductance of by the inductor. Typically Finite Element Analysis (FEA) and/or Magnetic Equivalent Circuit (MEC) based solution scheme is utilized for such calculations [7]. However, FEA based methods are computationally time consuming as compared to MEC based

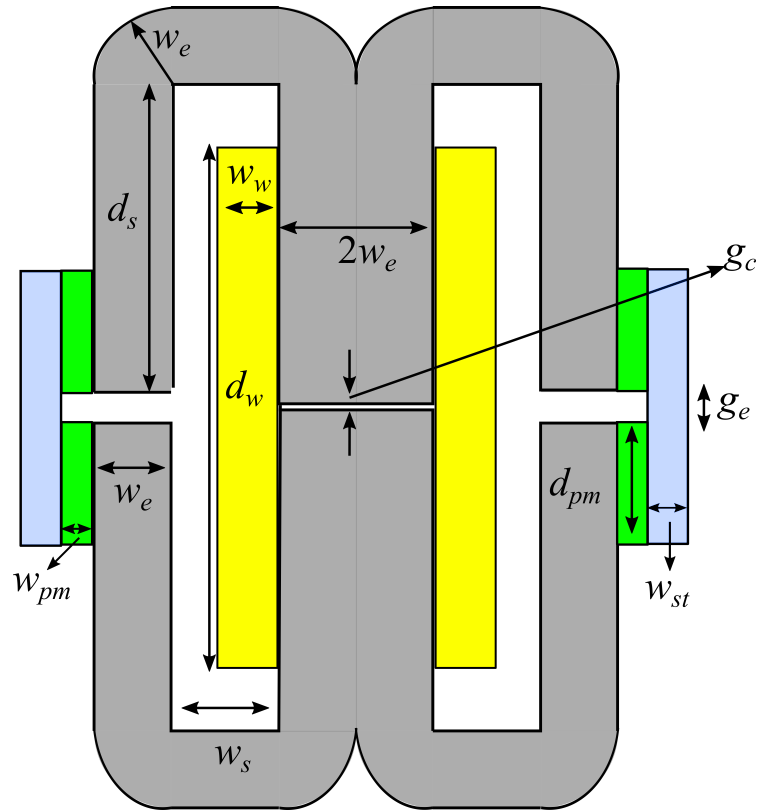


Fig. 6.5. FINEMET based EE-core PMI geometry

solution [7], and hence MEC of the inductor will be utilized. In an MEC based solution, reluctance/permeance circuit of the inductor is constructed, and is solved for flux in the circuit with the winding MMF as the source.

In a Magnetic Equivalent Circuit (MEC), magnetic permeance in-terms of flux in branch b and MMF across it, is defined as

$$\Phi_b = P_b F_b \quad (6.13)$$

where Φ_b and P_b are the flux and permeances of the magnetic branch b , respectively, and F_b is the MMF across the branch. To this end, the MEC for the EE-PMI geometry is shown in Fig. 6.6. In the shown MEC, permeance P_1, P_2, P_4, P_6, P_8 and P_9 are core branch permeances, P_3 is horizontal slot leakage permeance, P_5 is equivalent permeance across permanent magnet, and P_7 and P_{10} are airgap permeances. Note that the MEC has symmetry across the center leg, however, for convenience the full

MEC is shown herein although the MEC solver utilizes its symmetry to speed-up the calculations.

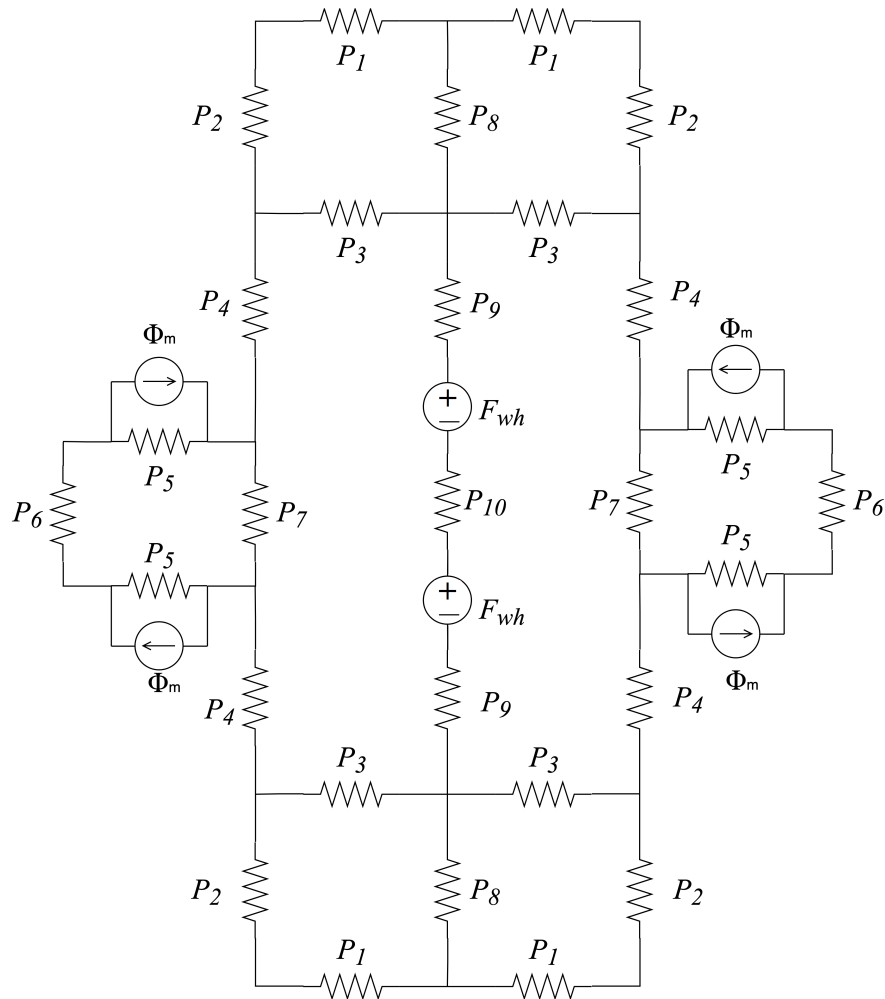


Fig. 6.6. EE-PMI Magnetic Equivalent Circuit

Using (6.13), the core branch permeance $P_{br,j}$ as a function of branch flux can be expressed as

$$P_{br,j}(\Phi_{br,j}) = \frac{A_{br,j} \mu_B(\Phi_{br,j}/A_{br,j})}{l_{br,j}} \quad (6.14)$$

where $A_{br,j}$ and $l_{br,j}$ are the cross-sectional area and magnetic path length, respectively, of the branch j and $\mu_B(\Phi_{br,j}/A_{br,j})$ is the magnetic permeability of the material in terms of the flux $\Phi_{br,j}$. This accounts for the non-linearity of the core material. Using (6.14), the core branch permeances can be readily expressed using length and area

of respective branches provided in Table 6.1 wherein length parameter y_h is defined and calculated in (6.26) and (6.27).

Table 6.1.
Core Branch Permeance Parameters

Permeance	Length	Area
P_1	$w_s + \frac{\pi w_e}{2}$	$w_e l_c$
P_2	y_h	$w_e l_c$
P_4	$d_s - y_h$	$w_e l_c$
P_6	$g_e + d_{pm}$	$w_{st} l_c$
P_8	y_h	$2w_e l_c$
P_9	$d_s - y_h + \frac{g_e - g_c}{2}$	$2w_e l_c$

Next, fringing permeance is undertaken. Based on inductor geometry, two broad possibilities for fringing path consideration at end leg airgap exist: 1) path shown as p_{f1} , and 2) path shown as p_{f3} in Fig. 6.7. For the fringing flux paths p_{f1} the calculation is straightforward and has been derived in [7, 50–53], using which the fringing flux can be expressed as

$$P_{f1}(l, w, g) = \frac{\mu_0 l}{\pi} \ln \left(1 + \frac{\pi w}{g} \right) \quad (6.15)$$

where l is the length of the core into the page. Similarly, fringing permeance for path p_{f4} , denoted P_{f4} can be expressed using (6.15).

Simialrly, for fringing path p_{f2} , permeance P_{f2} can be expressed, assuming relative permeability of magnet to be nearly 1, as

$$P_{f2}(l, w_m, g) \approx \frac{\mu_0 l}{\pi} \ln \left(1 + \frac{2w_m}{g} \right) \quad (6.16)$$

with $\max(r_1)$ in Fig. 6.7 calculated as

$$\max(r_1) = \frac{2w_{pm}}{\pi} \quad (6.17)$$

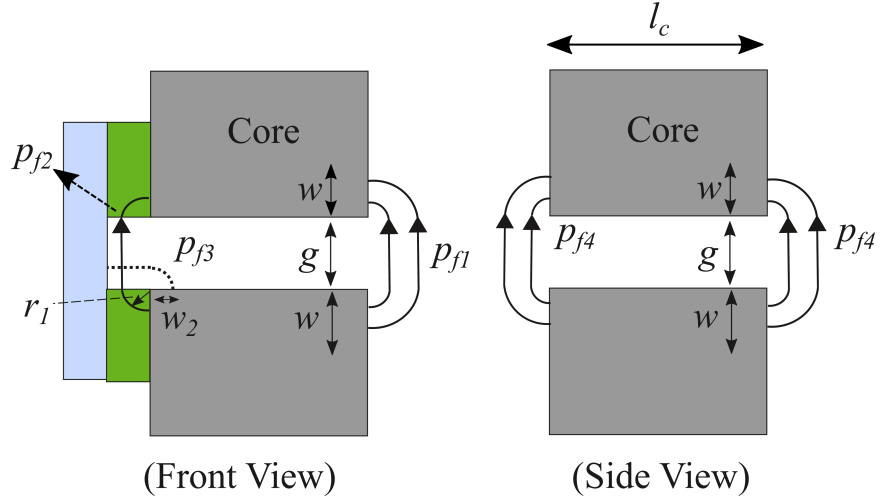


Fig. 6.7. Air Gap Fringing Paths in EE-PMI

Next, fringing across magnet shown as path p_{f3} can be calculated using [7] as

$$P_{f3}(l, w) \approx \frac{2\mu_0 l}{\pi} \ln \left(1 + \frac{\pi w}{2w_{pm}} \right) \quad (6.18)$$

Similarly, fringing flux path permeance across magnet at the front and back face of the EE-core inductor can be expressed using (6.15) as

$$P_{f5}(w) = \frac{\mu_0 d_{pm}}{\pi} \ln \left(1 + \frac{\pi w}{w_{pm}} \right) \quad (6.19)$$

Permeance of center leg air gap is summation of direct permeance and fringing flux around the center arm. Hence

$$P_{10} = \mu_0 \frac{2w_e l_c}{g_c} + 2P_{f1}(l_c, \min(w_s, d_s/2), g_c) + 2P_{f1}(2w_e, d_s/2, g_c) \quad (6.20)$$

Similarly, end leg air gap permeance P_7 can be expressed as

$$P_7 = \mu_0 \frac{w_e l_c}{g_e} + P_{f1}(l_c, \min(w_s, d_s/2), g_e) + 2P_{f1}(w_e, d_s/2, g_e) + P_{f2}(l_c, g_e) \quad (6.21)$$

where w_{st} is the width of steel. Finally, equivalent magnet permeance P_5 is given as

$$P_5 = \mu_m \frac{d_{pm} l_c}{w_{pm}} + P_{f3}(l_c, \min(g_e, w_e/2)) + 2P_{f5}(\min(w_e/2, w_{st})) \quad (6.22)$$

which is sum of magnet permeance and fringing permeance around magnet (in and out of the plane of paper).

Next, leakage flux permeance is considered. Only horizontal flux leakage is considered as shown in Fig. 6.8, and vertical slot leakage and end turn leakages are not considered in this formulation. To this end, using Ampere's law, the MMF drop across the winding slot as a function of defined distance y in Fig. 6.8 is approximated as

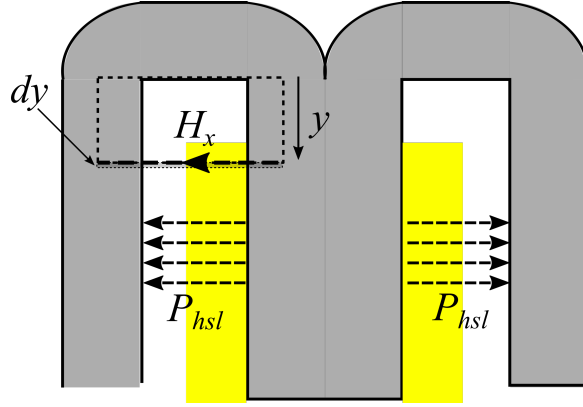


Fig. 6.8. Horizontal Flux Leakage in EE-PMI

$$H_x w_s \approx \begin{cases} 0 & 0 \leq y \leq d_s - \frac{d_w}{2} \\ \frac{N_t i_{ee}}{d_w} \cdot (y - (d_s - d_w/2)) & d_s - \frac{d_w}{2} < y \leq d_s \end{cases} \quad (6.23)$$

where N_t is the number of turns in winding and i_{ee} is the current through it. Using (6.23), the total leakage flux density can be calculated. Finally, the horizontal leakage flux associated with upper half of the winding can be expressed

$$\Phi_{hsl,t} = \int B_{hsl} ds = \mu_0 l_c \frac{N_t i_{ee}}{w_s d_w} \int_{d_s - d_w/2}^{d_s} \left(y - (d_s - \frac{d_w}{2}) \right) dy = \mu_0 l_c \frac{N_t i_{ee}}{2w_s} \left(\frac{d_w}{4} \right) \quad (6.24)$$

using which P_{hsl} or P_3 in MEC can be expressed as

$$P_3 \approx \frac{\mu_0 l_c d_w}{4w_s} \quad (6.25)$$

The length along y , y_h , upto which half of the horizontal leakage flux goes through winding can be calculated using

$$\mu_0 l_c \frac{N_t i_{ee}}{w_s d_w} \int_{d_s - d_w/2}^{y_h} \left(y - \left(d_s - \frac{d_w}{2} \right) \right) dy = \mu_0 l_c \frac{N_t i_{ee}}{4w_s} \left(\frac{d_w}{4} \right) \quad (6.26)$$

which yields

$$y_h = \left(d_s - \frac{d_w}{2} \right) + \frac{d_w}{2\sqrt{2}} \quad (6.27)$$

The length y_h will be used to place the P_3 in MEC of the inductor.

The constant flux Φ_m by magnet shown in MEC is calculated as

$$\Phi_m = d_{pm} l_c B_r \quad (6.28)$$

where B_r is the residual flux density of the magnet. Finally, the MMF source generated by winding, F_w , is given by

$$F_w = N_t i_{ee} \quad (6.29)$$

using which half MMF source can be calculated as

$$F_{wh} = \frac{F_w}{2} \quad (6.30)$$

This completes all the required parameters for the MEC in Fig. 6.6.

For the core, as discussed, FINEMET FT3-M has been selected. The core material parameters are presented in Appendix C. Material parameters for steel and magnet are taken from [7]. The MEC is solved using the MEC Toolbox described in [7,51]. As mentioned earlier, symmetry in MEC circuit shown in Fig. 6.6 is utilized in the MEC solver to reduce the the number of mesh and branch elements [7]. FEA validation of the inductor MEC is shown in Appendix D.

Volume and Mass

For the formulation of optimization function, volume, mass and loss calculations will be required for the inductor. An ideal conductor packing in the winding is shown in Fig. 6.9 wherein the conductor radius is r_w .

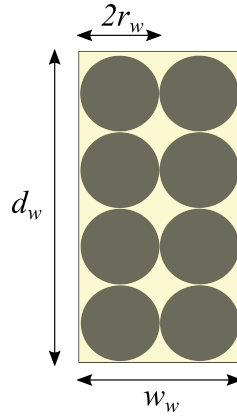


Fig. 6.9. Ideal Conductor Packing in the Winding

Based on the ideal conductor packing, the width and depth of the winding are assumed to be

$$w_w = 2N_{wt}r_wk_b \quad (6.31)$$

and

$$d_w = 2N_{dt}r_wk_b \quad (6.32)$$

where N_{wt} and N_{dt} are the number of conductors along the width and depth of the winding, respectively, and $k_b > 1$ is a factor to denote larger winding size than ideal and represents under-utilization of winding space. The total number of conductors, N_t can be calculated as the product of N_{wt} and N_{dt} . The packing factor $k_{pf,E}$ is computed as

$$k_{pf,E} = \frac{N_t w_{ac}}{w_w d_w k_b^2} \quad (6.33)$$

Next, the total height h_E , width w_E and length l_E of the PMI can be readily calculated as

$$h_E = 2w_e + 2d_s + g_e \quad (6.34)$$

$$w_E = 2(w_{st} + w_{pm} + 2w_e + w_s) \quad (6.35)$$

$$l_E = l_c + 2w_w \quad (6.36)$$

Using the calculated dimensions, the volume of cuboid circumscribing the PMI can be calculated. The aspect ratio of the PMI $a_{sr,E}$ can be defined as ratio of largest to smallest dimension, that is

$$a_{sr,E} = \frac{\max(h_E, w_E, l_E)}{\min(h_E, w_E, l_E)} \quad (6.37)$$

Next, the volume of core $V_{cr,E}$ can be calculated as

$$V_{cr,E} = 2l_c w_e (\pi w_e + 4d_s + (g_e - g_c)) \quad (6.38)$$

The volume of the coil region $V_{cl,E}$ is given by [7]

$$V_{cl,E} = d_w w_w (\pi w_w + 2(l_c + 2w_w)) \quad (6.39)$$

The volume of conductor $V_{cd,E}$ is computed as

$$V_{cd,E} = k_{pf,E} V_{cl,E} \quad (6.40)$$

The volume of the permanent magnet can be expressed using

$$V_{pm,E} = 4l_c d_{pm} w_{pm} \quad (6.41)$$

Lastly, the volume of steel laminations is given as

$$V_{st,E} = 2l_c w_{st} (2d_{pm} + g_e) \quad (6.42)$$

Given the volumes of componets used in the PMI, their respective masses can be calculated as product of their mass densities with their respective volume. Hence,

$$M_{cr,E} = \rho_{cr} V_{cr,E} \quad (6.43)$$

$$M_{cd,E} = \rho_{cd} V_{cd,E} \quad (6.44)$$

$$M_{pm,E} = \rho_{pm} V_{pm,E} \quad (6.45)$$

$$M_{st,E} = \rho_{st} V_{st,E} \quad (6.46)$$

where $M_{cr,E}$, $M_{cd,E}$, $M_{pm,E}$ and $M_{st,E}$ are the mass, and ρ_{cr} , ρ_{cd} , ρ_{pm} and ρ_{st} are densities of core, conductor, permanent magnet and flap, respectively. Their material data

is provided in [7]. Core material parameters are presented in Table C. PM material data is taken from [7].

Similar to generator metamodel, the calculated mass does not include the structural mass, and will be referred as electrical mass of the inductor. Total electrical mass of the EE-PMI $M_{t,ee}$ can be expressed as

$$M_{t,ee} = M_{cr,E} + M_{cd,E} + M_{pm,E} + M_{st,E} \quad (6.47)$$

Inductance

The incremental inductance L_{inc} of the inductor at winding current i_{ee} is calculated as

$$L_{inc}(i_{ee}) = \frac{\lambda(i_{ee} + \delta i_{ee}) - \lambda(i_{ee})}{\delta i_{ee}} \quad (6.48)$$

where λ is the flux linkage of the winding, and δi_{ee} is small incremental current (of order 10^{-3} A). Incremental inductance is evaluated at multiple current operating points of interest. For the high-speed simulation of MMC, the value of inductance utilized will be

$$L_{s,i} = \min_{i_{ee}}(L_{inc}(i_{ee})) \quad (6.49)$$

A constraint will be imposed in the design optimization on the ratio of maximum to minimum incremental inductance so that the inductor behave linearly for normal operation.

Loss Calculation

Next, inductor losses are considered. In terms of the coil volume, the inductor resistance can be calculated as [7]

$$R_{cd,E} = \frac{V_{cd,E} N_t^2}{\sigma_c k_{pf,E} w_w^2 d_w^2} \quad (6.50)$$

where σ_c is the conductivity of the material. Using (6.50) average resistive power loss in inductor $P_{L,r,ee}$ can be calculated using inductor current waveform from the high-speed simulation.

Next, core losses in the inductor are considered. A straight-forward approach to calculate the core loss is by computing flux density in core at each time-instant in the converter current waveform, and utilize empirical core loss models to compute core losses. Though simple, this approach adds extensive computational burden to optimization based design methods due to the presence of switching harmonics in the current waveform as the solution of MEC requires an iterative solver for magnetically non-linear core materials [7].

As an alternative, a hybrid core loss calculation method is proposed. In this method, an assumption is made that the DC and fundamental component of inductor current primarily determine the flux and flux density levels in the core. Using this assumption, the MEC is solved for smaller set of sample points in the domain of the MMC arm current waveform consisting of the DC and fundamental component. In the inductor current waveform, n_t equally spaced sample current points are taken as

$$i_{ee}[k] = i_{dc,ee} - i_{s,ee} + \frac{2i_{s,ee}}{n_t - 1}(k - 1), \quad k \in \{‘1’, ‘2’, \dots, ‘n_t’\} \quad (6.51)$$

where $i_{dc,ee}$ is the DC component and $i_{s,ee}$ is the amplitude of fundamental component of current in the inductor.

After solving the MEC at each current level, the hysteresis loss density in branch j due to fundamental component of flux density can be calculated using the Steinmetz Model [7] as

$$P_{c,ld,j,h} = k_h \left(\frac{f_r}{f_b} \right)^{\alpha_h} \left(\frac{\Delta B_{j,pk}}{2B_b} \right)^{\beta_h} \quad (6.52)$$

where k_h , α_h and β_h are the hysteresis loss model parameters, f_b and B_b are the base frequency and flux density, respectively, f_r is the fundamental frequency, and $\Delta B_{j,pk}$ is the absolute value of difference of minimum and maximum flux density at branch j in the core. Note that in case of PMI, due the presence of constant magnet flux in the core, the accuracy of the hysteresis loss calculation using (6.52) may be problematic. However, for the FINEMET material that will be used in the notional design example at Chapter 7, a high degree of inaccuracy can be tolerated since the contribution of $P_{c,ld,j,h}$ is very small to total loss. Similarly, low frequency eddy current losses can be

neglected. The effect of harmonic component of MMC arm current on core saturation is ignored. Using this assumption, the MEC can be solved at significantly reduced time instants in MMC waveform.

Although the low frequency core losses will be modest, high-frequency eddy current losses may be significant. To this end, it will be assumed that for normal operating conditions, the flux is a affine function of current since constraints will be placed on the design to insure magnetic linearity. With this assumption, the following approach is undertaken: Consider branch j in the MEC. At current sample k , the flux density $B_j[k]$ can be solved for MMC inductor current $i[k]$ using the method described above. The coefficient $\psi_{B,j}[k]$ for branch j is defined as

$$\psi_{B,j}[k] = \frac{\Delta B_{j,k}}{\Delta i_{j,k}}, \quad k \in \{ '1', '2', \dots, 'n_t - 1' \} \quad (6.53)$$

where

$$\Delta B_{j,k} = B_j[k + 1] - B_j[k] \quad (6.54)$$

$$\Delta i_{ee,k} = i_{ee}[k + 1] - i_{ee}[k] \quad (6.55)$$

A least squared solution of $\psi_{B,j}[k]$, denoted $\Psi_{B,j}$ can be calculated as

$$\Psi_{B,j} = \frac{[\psi_{B,j}][\Delta i_{ee,k}]^T}{[\Delta i_{ee,k}][\Delta i_{ee,k}]^T} \quad (6.56)$$

which is a constant with time for the given branch j . Using $\Psi_{B,j}$, harmonic component of flux density for harmonic component in arm inductor current can be estimated. Suppose the κ_f harmonic component of current has amplitude $i_{\kappa f}$, the amplitude of κ_f harmonic flux density harmonic of flux density in branch j , $B_{j,\kappa f}$, can be calculated as

$$B_{j,\kappa f} = \Psi_{B,j} i_{\kappa f} \quad (6.57)$$

Similar process can be repeated for other branches and current harmonics of interest in MEC. The input of such calculations will be amplitudes of MMC arm harmonic currents and the output will be the amplitudes of harmonic flux densities in different MEC branches.

From the calculated harmonic flux density amplitudes in the inductor for current harmonics of interest, the total eddy current core density in branch j is assumed to be [7, 51–53]

$$P_{c,ld,j,e} = k_{e,hf} \sum_{\kappa_f=\kappa_{f,min}}^{\kappa_{f,max}} f_{\kappa_f}^{\alpha_{ehf}} B_{j,\kappa_f}^{\beta_{ehf}} \quad (6.58)$$

where $\kappa_{f,min}$ and $\kappa_{f,max}$ are the minimum and maximum harmonics of interest, f_{κ_f} is the frequency (in Hz) of κ_f harmonic, and $k_{e,hf}$, α_{ehf} and β_{ehf} are the eddy loss parameters.

Total core loss density in the branch j of the inductor is given by

$$P_{c,ld,j} = P_{c,ld,j,h} + P_{c,ld,j,e} \quad (6.59)$$

using which core losses in the branch j , $P_{c,j}$, can be calculated as product of $P_{c,ld,j}$ and its volume. Core losses in other branches of the inductor can be similarly computed. The total core loss $P_{L,c,ee}$ is the sum of core losses in all the inductor branches.

The total power loss in the inductor $P_{L,ee}$ is given by

$$P_{L,ee} = P_{L,r,ee} + P_{L,c,ee} \quad (6.60)$$

Magnet losses are not considered for this work. Skin and proximity effect losses have been neglected.

6.2.2 Standard EE-core Inductor

A standard EE-core inductor topology, based on EE-PMI except magnets, is selected. The inductor structure is shown in Fig. 6.10. In this inductor, center leg air gap g_c is kept equal to end leg air gap g_e . The analysis of this inductor is similar except the side leg air gap permeances where the center leg airgap based analysis is used. Loss, mass and inductance analysis is similar to the EE-PMI.

MEC of the standard EE-core inductor is shown in Fig.6.11. In the MEC, the core permeances P_1, P_2, P_4 and P_9 are found using (6.14) and Table 6.1. The horizontal leakage permeance P_3 is found using (6.25), and air gap permeance P_{10} is found using

(6.20). MMF sources in Fig. 6.11 F_{wh} are given by (6.29)-(6.30). The MEC is solved using MEC Toolbox as described earlier. This MEC will be used in next chapter to compare with the EE-PMI in system design optimization.

Similar to EE-PMI, the mass of the inductor is calculated as summation of core and conductor from (6.43), (6.44). The total inductor mass is given by

$$M_{t,ep} = M_{cr,E} + M_{cd,E} \quad (6.61)$$

The resistance of the EE-core inductor can be calculated by (6.50). Similarly, core losses are computed using (6.59). The total power loss $P_{L,ee}$ is calculated as sum of core and resistive losses. Finally, using MEC solution, incremental inductance of the EE-core inductor is calculated using (6.48). FEA validation of the inductor MEC is shown in Appendix D.

This completes the formulation of the design equations for the proposed passive components. The models/equations presented in this chapter for capacitor and inductor will be used in next chapter for the development of a formal multi-objective optimization problem.

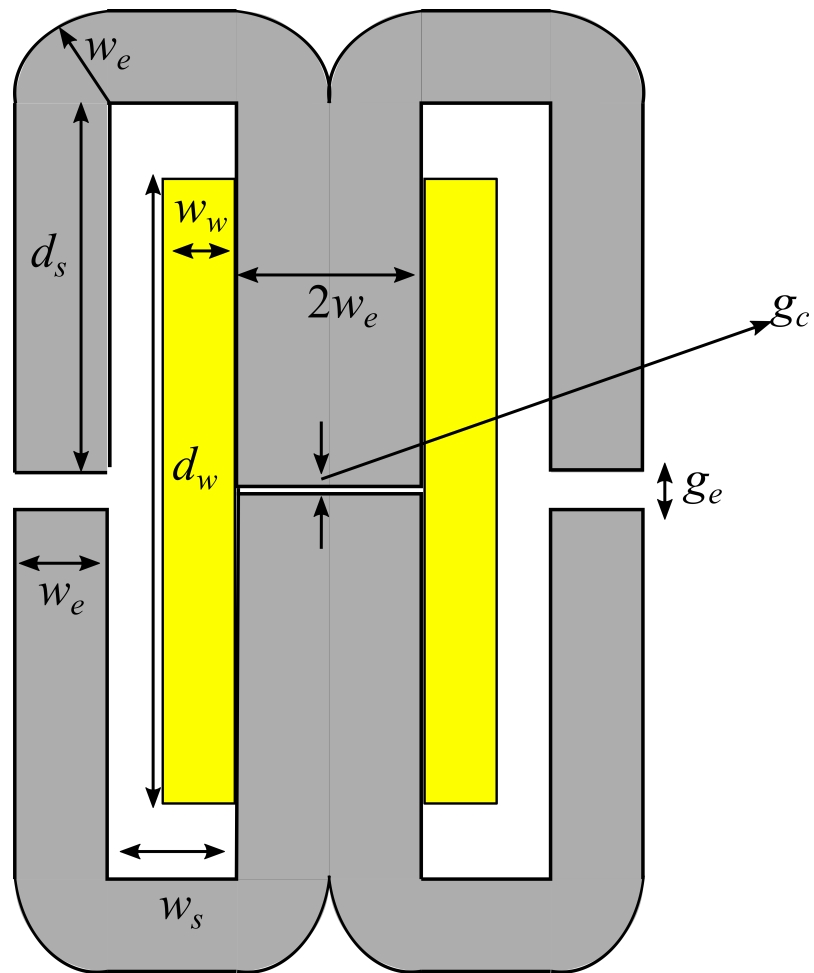


Fig. 6.10. EE-core Inductor Geometry

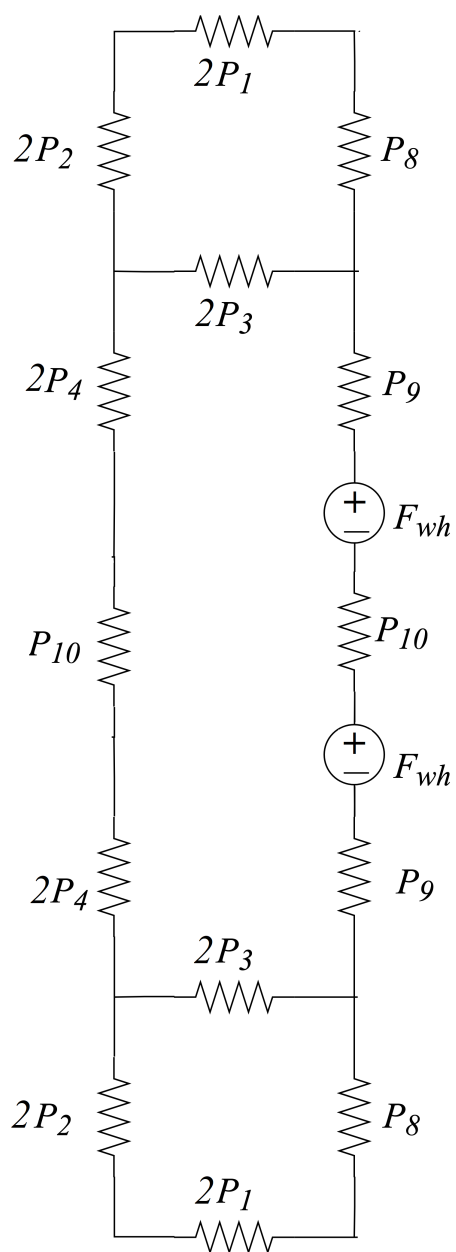


Fig. 6.11. Standard EE-core Inductor MEC

7. MULTI-OBJECTIVE OPTIMIZATION OF MMC BASED GENERATOR-RECTIFIER SYSTEM

In the introduction of this dissertation, the shortcomings of existing design methods for the PMAC-MMC system were described. The component design and simulation models required to formulate a fitness function were discussed in Chapters 2-6. These included a generator metamodel, a high-speed MMC simulation model, a semiconductor conduction and switching loss model, a heat sink metamodel, arm inductor models, and a submodule capacitor model.

To start the formulation of a multi-objective optimization problem, first, it is required to define the objectives to be satisfied for the design optimization. Next, system constraints must be defined. The third and the last challenge faced relates to how the constraints and objectives will be implemented so as to formulate the design process as a multi-objective optimization problem.

This chapter is divided in following sections: First, the formulation of the design problem is set forth in Section 7.1. This section describes the design space, design metrics, and the design constraints considered. Next, case studies of the system design using the proposed design paradigm is set forth in Section 7.2.

7.1 Design Problem Formulation

The design problem will be formulated as a multi-objective optimization problem in which the system design metrics of interest will be minimized subject to a variety of constraints. With the two inductor topologies, the optimization problem will be solved twice, separately, to compare the EE-PMI against a standard EE-core inductor for the MMC arm. The purpose of the comparison is to determine whether the PMI offers any advantage over standard inductor in an MMC application.

7.1.1 Design Space

To begin the formulation of a design problem, it is important to be able to identify the design variables. The design space contains all the free variables which can be selected by the designer. For the considered design problem, the design variables are stored in design variable vector $\boldsymbol{\theta}$ given by

$$\boldsymbol{\theta} = \left[\rho_{TM} \quad \omega_{rpm} \quad \alpha_{ns1} \quad P_{l,mmc,est} \quad C_{sm} \quad N \quad N_{scpf} \quad C_{in} \quad \boldsymbol{\theta}_L \right]^T \quad (7.1)$$

where $P_{l,mmc,est}$ is the estimated MMC loss, C_{sm} is the submodule capacitance, N is number of submodules, N_{scpf} is number of switching cycles per fundamental cycle (effectively setting the switching frequency), and C_{in} is the DC bus capacitance. The generator metamodel requires 4 parameters: specific torque density ρ_{TM} , generator speed in rpm ω_{rpm} , DC bus utilization factor α_{ns1} , and estimated generator terminal power output $P_{go,est}$. For a given DC power requirement P_{dc} , $P_{go,est}$ can computed as

$$P_{go,est} = P_{dc} + P_{l,mmc,est} \quad (7.2)$$

In this analysis, it is assumed that the switching frequency of the converter is an integer multiple of the frequency of the fundamental component of voltage/current. Hence

$$f_{sw} = N_{cpf} f_r \quad (7.3)$$

The vector $\boldsymbol{\theta}_L$ contains parameters of inductor used in each leg. Based on the inductor geometry, $\boldsymbol{\theta}_L$ is given by

$$\boldsymbol{\theta}_L = \begin{cases} \boldsymbol{\theta}_{L,EE,P} & \text{EE-Core PMI} \\ \boldsymbol{\theta}_{L,EE} & \text{EE-Core} \end{cases} \quad (7.4)$$

For the EE-PMI, $\boldsymbol{\theta}_{L,EE,P}$ can be expressed as

$$\boldsymbol{\theta}_{L,EE,P} = [l_c \quad w_e \quad g_e \quad w_{ac} \quad w_{pm} \quad d_{pm} \quad N_{dt} \quad N_{wt}] \quad (7.5)$$

where w_{ac} is the cross-sectional area of the conductor used in the PMI. To reduce the number of design variables, it is assumed that the ratios w_{sf} and d_{sf} defined as

$$w_{sf} = \frac{w_s}{w_w} \quad (7.6)$$

and

$$d_{sf} = \frac{2d_s}{d_w} \quad (7.7)$$

are fixed a-priori. Similarly, the magnet material is also fixed.

Similarly, for the standard EE-core, the design variable vector is given by

$$\boldsymbol{\theta}_{L,EE} = [l_c \quad w_e \quad g_e \quad w_{ac} \quad N_{dt} \quad N_{wt}] \quad (7.8)$$

The EE-core inductor center leg air gap g_c is taken equal to end leg air gap g_e .

As discussed earlier, the high-speed simulation developed in Chapter 4 requires an iterative solver to compute the machine q - axis current. Similar to the heat sink optimization shown in Chapter 5, during the development of the fitness function for the PMAC-MMC system, it was realized that the iterative solver for the system currents is not necessary as the optimization engine can solve for the required q - axis current whilst optimizing the system if appropriate constraints and design metrics are imposed. That is why P_{go} is a design variable. Neglecting windage losses, for PMAC generator, q - axis current can be calculated using (4.2) [7]

$$I_{qs}^r = -2(P_{go} + P_r)/(3\omega_r\lambda_m) \quad (7.9)$$

where P_r is generator resistive loss calculated using generator metamodel. It is assumed that generator core losses (eddy current and hysteresis) primarily act as windage losses in the sense that they primarily add to the prime mover torque, and do not significantly change I_{qs}^r .

In addition to the design variables, fixed design parameters will be defined. These are contained in the structure \mathbf{D} , described as

$$\mathbf{D} = \left[\mathbf{M}_{PM} \quad \mathbf{C}_{SM} \quad \mathbf{L}_M \quad \mathbf{S}_{sw} \quad \mathbf{H}_{hs} \quad V_{dc} \quad P_{dc} \right]^T \quad (7.10)$$

where \mathbf{M}_{PM} is a structure containing PMAC metamodel parameters, structure \mathbf{C}_{SM} contains capacitor parameters, structure \mathbf{L}_M contains inductor parameters, structure \mathbf{S}_{sw} contains semiconductor device parameters, \mathbf{H}_{hs} contains heat sink metamodel parameters, V_{dc} and P_{dc} are DC bus voltage and power load, respectively.

Metamodel parameters are available at [31]. Three different power electronic switches have been considered in Appendix A [55–57]. Device parameters were obtained from the respective datasheets. Capacitor model parameters are shown in Appendix B [49]. Heat sink metamodel parameters are presented in Table 5.4.

In the inductor design optimization, the conductor and end leg flap materials of the EE-PMI are fixed to Aluminum and FINEMET, respectively. Similarly, permanent magnet material is fixed at NdFeB N35. Clearly, the magnet type could have been added as a design parameter. The inductor material parameters are presented in Appendix C. Other design fixed parameters are shown in Table 7.1.

7.1.2 Design Constraints

To ensure proper and desired operation of the MMC, constraints will be imposed on the design. It is convenient to define less-than-or-equal-to and greater-than-or-equal-to functions as [7]

$$\text{lte}(x, x_{mx}) = \begin{cases} 1 & x \leq x_{mx} \\ \frac{1}{1 + x - x_{mx}} & x > x_{mx} \end{cases} \quad (7.11)$$

$$\text{gte}(x, x_{mn}) = \begin{cases} 1 & x \geq x_{mn} \\ \frac{1}{1 + x_{mn} - x} & x < x_{mn} \end{cases} \quad (7.12)$$

Next, constraints will be formulated for the proper operation of the system. Starting from the generator metamodel, constraint on generator rms current density $J_{rms,g}$ is imposed

$$c_1 = \text{lte}(J_{rms,g}, J_{max}) \quad (7.13)$$

where J_{max} is the maximum limit of current density. Next, a constraint is imposed on the generator rotor tip speed $S_{r,tip}$ such that

$$c_2 = \text{lte}(S_{r,tip}, S_{r,tip,max}) \quad (7.14)$$

where $S_{r,tip,max}$ is the maximum allowed tip speed of the rotor.

Table 7.1.
Fixed Design Parameters

Parameter	Value
Submodule capacitor ripple factor $\alpha_{v,sm}$	0.05
DC bus capacitor ripple factor $\alpha_{v,bus}$	0.001
Arm current factor $\alpha_{i,rip}$	1.07
Max. inductor & generator current density J_{max}	10 A/mm ²
Max. rotor tip speed $S_{r,tip,max}$	250 m/s
Max. junction temperature $T_{j,max}$	100°C
Ambient temperature T_{amb}	25°C
Max. switching frequency $f_{sw,max}$	50 kHz
Ambient temperature	25 °C
Max. allowed capacitor temperature $T_{c,max}$	70 °C
Min. submodule heat sink $R_{th,hsa,min}$	0.2 K/W
EE-PMI g_c	1 μ m
Max. inductor aspect ratio $a_{E,max}$	10
EE-core w_{sf}	1.1
EE-core d_{sf}	1.1
Max. to min. incremental inductance ratio $\alpha_{l,c}$	1.2
Max. allowed counter flux in PM $\alpha_{H,max}$	0.75
Inductor winding factor k_b	1.2
Max. magnet depth factor k_{pm}	0.5
Min. inductor center to upper leg flux ratio $\alpha_{\Phi,rat}$	90%
Data points taken in fundamental period for MEC n_t	8

The next set of constraints are applied on the inductor design model using the DC and fundamental component of MMC arm current. A constraint is applied to the geometrical aspect ratio of the inductor such that

$$c_3 = \text{lte}(a_{sr,E}, a_{E,max}) \quad (7.15)$$

where $a_{E,max}$ is the maximum allowed geometrical aspect ratio. Next, a constraint on convergence of non-linear MEC solution is applied such that the MEC solution exists [7]. That is

$$c_4 = \text{conv}(\text{MEC}) \quad (7.16)$$

where $\text{conv}(\text{MEC})$ denotes the convergence of the MEC [7]. Next, to limit the horizontal slot leakage flux, a constraint on ratio of flux through top branch to center leg is imposed

$$c_5 = \text{gte} \left(\min \left(\frac{\Phi_{top}}{\Phi_{mid}}, \alpha_{\Phi, \text{rat}} \right) \right) \quad (7.17)$$

where Φ_{top} and Φ_{mid} are the flux in top/bottom most and source MEC branch of inductor, a $\alpha_{\Phi, \text{rat}}$ is the minimum required flux ratio between center leg and ‘U’ region of the EE-core.

A constraint is imposed on maximum value of core incremental inductance, so as to avoid hard saturation of the core, as

$$c_6 = \text{lte} \left(\max_{i_{ee}}(L_{inc}(i_{ee})), \alpha_{l,c} \min_{i_{ee}}(L_{inc}(i_{ee})) \right) \quad (7.18)$$

where $L_{inc}(i_{ee})$ is the incremental inductor at current i_{ee} of the inductor, and $\alpha_{l,c}$ is factor to limit the ratio of maximum to minimum incremental inductance. In case of EE-PMI, another constraint is imposed at no load current such that

$$c_7 = \text{lte} (B_{pk,0}, B_{c,lim}) \quad (7.19)$$

where $B_{pk,0}$ peak flux density in core at no load current, and $B_{c,lim}$ is the maximum material limit on the flux density.

To avoid demagnetization of permanent magnet in EE-PMI, constraint on magnet flux intensity H_{mag} is imposed as

$$c_8 = \text{gte} (\min(H_{mag}), \alpha_{H,max} H_{lim,mag}) \quad (7.20)$$

where $H_{ci,mag}$ is the minimum field intensity before demagnetization in pm. Note that H_{mag} and $H_{lim,mag}$ are negative quantities.

Finally, a constraint on geometry of magnet is imposed for EE-PMI as

$$c_9 = \text{lte}(\max(d_{pm}, k_{pm}d_s)) \quad (7.21)$$

so as to limit the magnet size as compared to d_s . This completes constraints imposed on inductor design. Note that for standard EE-core inductor, constraints c_7 , c_8 and c_9 are not imposed.

The next set of constraints are imposed relate to MMC operation. A constraint on submodule capacitor voltage ripple is imposed for which maximum voltage ripple $v_{c,rip,max}$ is calculated as

$$v_{c,rip,max} = \max((v_{a,cap,up})_{pk-pk}, (v_{a,cap,low})_{pk-pk}) \quad (7.22)$$

where $(v_{a,cap,up})_{pk-pk}$ and $(v_{a,cap,low})_{pk-pk}$ are peak-to-peak amplitude of upper and lower capacitor voltages, respectively. Using (7.22) constraint c_{10} is formulated as

$$c_{10} = \text{lte}\left(v_{c,rip,max}, \alpha_{v,sm} \frac{V_{dc}}{N}\right) \quad (7.23)$$

where $\alpha_{v,rip}$ is the factor used to specify the voltage ripple limit. Next, a constraint on maximum submodule capacitor temperature change is imposed such that

$$c_{11} = \text{lte}(\Delta T_{c,sm}, T_{c,max} - T_{amb}) \quad (7.24)$$

where $\Delta T_{c,sm}$ is change in submodule capacitor temperature, $T_{c,max}$ is maximum rated temperature, and T_{amb} is the ambient temperature.

For the DC bus capacitor, the harmonic voltage can be estimated using (4.41) as

$$v_{cin,rip,h}(t) = \frac{1}{c_{in}} \int_0^t i_{cin,rip}(\tau) d\tau \quad (7.25)$$

using which a constraint on the ripple voltage is formulated as

$$c_{12} = \text{lte}(\max(v_{cin,rip,h}) - \min(v_{cin,rip,h}), \alpha_{v,bus} V_{dc}) \quad (7.26)$$

A constraint on DC bus capacitor temperature change $\Delta T_{c,b}$ is imposed in accordance with

$$c_{13} = \text{lte}(\Delta T_{c,b}, T_{c,max} - T_{amb}) \quad (7.27)$$

In Chapter 4, it was assumed that MMC never operates in the over-modulated region. To ensure this requirement, a constraint on maximum absolute value of duty cycle is imposed. The maximum of absolute value of duty cycles, d_{max} , is calculated as

$$d_{max} = \max(\|d_{a,up}\|_{\infty}, \|d_{a,low}\|_{\infty}) \quad (7.28)$$

Using (7.28), constraint c_{14} is imposed as

$$c_{14} = \text{lte}(d_{max}, 1) \quad (7.29)$$

Next, a constraint on pk-pk amplitude of upper and lower arm currents is imposed such that it is less than or equal to $\alpha_{i,rip}I_s$, where I_s is peak amplitude of fundamental component of machine current. The maximum ripple current $i_{rip,max}$ is defined as

$$i_{rip,max} = \max((i_{a,up})_{pk-pk}, (i_{a,low})_{pk-pk}) \quad (7.30)$$

using which the constraint is formulated as

$$c_{15} = \text{lte}(i_{rip,max}, \alpha_{i,rip}I_s) \quad (7.31)$$

Next, as with the generator, the maximum current density in the arm inductor is limited using constraint c_{16} as

$$c_{16} = \text{lte}(\max(|J_{a,up}|), J_{max}) \quad (7.32)$$

where $J_{a,up}$ is the current densities in a - phase upper MMC arm inductor. The next constraint on MMC operation limits the maximum switching frequency of operation to $f_{sw,max}$, as

$$c_{17} = \text{lte}(f_{sw}, f_{sw,max}) \quad (7.33)$$

Note that the limit on switching frequency does not come from the limitation on thermal heat dissipation capability but rather due to the limitation of semiconductor device switching speed. Semiconductor devices have manufacturer specified limits on maximum switching rate and $f_{sw,max}$ takes this into the consideration.

The next constraint related to the heatsink. For the heatsink, the minimum possible heat sink thermal resistance is limited as

$$c_{18} = \text{gte}(R_{th,hs-a}, R_{th,hs-a,min}) \quad (7.34)$$

where $R_{th,hs-a,min}$ is minimum possible heat thermal resistance of the heat sink for the metamodel to retain validity.

The estimated input mechanical power to the system can be computed as sum of estimated generator terminal power output $P_{go,est}$ and generator losses, that is

$$P_{in,est} = P_{go,est} + P_r + P_e + P_h \quad (7.35)$$

Finally, constraint c_{19} is imposed so that the estimated input power is greater than the actual input power, i.e.

$$c_{19} = \text{gte}(P_{in,est}, P_{loss} + P_{dc}) \quad (7.36)$$

The minimization of mass and loss applies optimization pressure to reduce $P_{in,est}$ until it reduces to $P_{dc} + P_{loss}$. Further details on this constraint is provided in subsection 7.1.3.

With this, required constraints have been formulated. Note that for EE-core inductor (without magnet), any constraint involving magnet design is removed from the design optimization. With formulated constraints, design metrics of interest are defined in the following subsection.

7.1.3 Design Metrics

As described in the first chapter, mass and loss are the two metrics of interest. The mass calculation is the first undertaken. As discussed in previous chapters, electrical mass are calculated for generator using metamodel procedure described in Chapter 2, heat sink and semiconductor device package using Chapter 5 and [55–57], and capacitor and inductor using Chapter 6. The total mass, electrical plus structural, of the system can be expressed as

$$M_t = x_{m1}M_{ge} + 6x_{m2}(N(M_{hd} + M_{sdp}) + M_L + NM_{Csm} + M_{Cin}) \quad (7.37)$$

where

$$M_L = \begin{cases} M_{t,ee} & \text{EE-PMI} \\ M_{t,ee} & \text{EE-core Inductor} \end{cases} \quad (7.38)$$

and where M_{ge} is generator mass, M_{hd} is heat dissipation system mass, M_{sdp} is the semiconductor device package mass, M_{Csm} and M_{Cin} are submodule and bus capacitor mass, respectively, M_L is inductor mass, and factor x_{m1} and x_{m2} accounts for the structural, case and cabinet mass for generator and MMC, respectively. In this work x_{m1} and x_{m2} are taken equal to 1. A factor of 6 is multiplied in MMC mass to account for each arm (there are 6 such arms). N is multiplied to submodule capacitor and heat sink mass to account for N submodules in each arm.

Next, the system loss calculation is considered. Generator resistive and core losses are calculated using the metamodel presented in Chapter 2 for specified P_{go} using (2.62). MMC semiconductor conduction ($P_{cd,up}$) and switching ($P_{sw,up}$) losses are computed using high-speed simulation from Chapter 4 and semiconductor loss models from Chapter 5. For the required heatsink, the fan power to the heatsink, P_{fan} , is considered as system loss, and is determined using (5.48). Submodule and DC bus capacitor ESR losses, $P_{Csm,esr}$ and $P_{Cin,esr}$ respectively, are computed using (6.4)-(6.5). Finally, inductor losses P_L are computed as sum of resistive losses and core losses (using (6.60)) for a - phase upper MMC arm. Total system losses are calculated as

$$P_{loss} = [P_r + P_e + P_h] + (6P_L + 6P_{Csm,esr} + 6P_{cd,up} + 6P_{sw,up} + 6NP_{fan} + P_{Cin,esr}) \quad (7.39)$$

In (7.39), similar to mass calculation, factor of 6 is multiplied to account for 6 MMC arms, and a factor of N accounts for N submodules in an MMC arm.

Inductor loss P_L is given by

$$P_L = \begin{cases} P_{L,ee} & \text{EE-PMI} \\ P_{L,ee} & \text{EE-core Inductor} \end{cases} \quad (7.40)$$

Total generator and MMC losses, P_{gl} and $P_{l,mmc}$ respectively, can be expressed as

$$P_{gl} = P_r + P_c + P_h \quad (7.41)$$

$$P_{l,mmc} = 6P_L + 6P_{Csm,esr} + 6P_{cd,up} + 6P_{sw,up} + 6NP_{fan} + P_{Cin,esr} \quad (7.42)$$

Total mechanical input power to the generator rectifier system can be expressed

$$P_{in} = P_{loss} + P_{dc} \quad (7.43)$$

Note that an estimation of MMC power losses and generator terminal power output is required to calculate the metamodel parameters, without which the high-speed simulation cannot be conducted. To introduce optimization pressure to reduce the error between estimated losses and actual losses, a system loss design metric is defined as

$$P_{lsq} = P_{loss} + \kappa_{pl}(P_{l,mmc,est} - P_{l,mmc})^2 \quad (7.44)$$

such that the design metric P_{lsq} varies as square of error in estimation of MMC loss. In (7.44), κ_{pl} is factor used to weigh the square of error in loss estimation, and is taken as 0.5 in this design paradigm. Using P_{lsq} as design metric along with c_{19} not only minimizes actual system losses (using P_{loss}) but minimizes the error in loss estimation. Recall that constraint c_{19} (7.36) ensures $P_{in,est} > P_{in}$. With this, the calculation of design metrics is complete. Next, design fitness will be formulated for optimizing the system.

7.1.4 Design Fitness

As suggested in [7], the fitness function will be defined as

$$f = \begin{cases} \epsilon \begin{bmatrix} 1 & 1 \end{bmatrix}^T \left(\frac{C_S - N_C}{N_C} \right) & C_S < C_I \\ \begin{bmatrix} 1 & 1 \end{bmatrix}^T \left[\frac{1}{M_t} \quad \frac{1}{P_{lsq}} \right] & C_S = C_I \end{cases} \quad (7.45)$$

where

$$C_s = \sum_{i=1}^{c_t} c_i \quad (7.46)$$

and where N_C , C_S and C_I represent the number of constraints, the number of constraints satisfied, and number of constraints imposed during the evaluation of the objective function, ϵ is a small positive number of the order 10^{-10} , and c_t is total number of constraints. If all the constraints are not satisfied, the objective function will yield a small negative number. Otherwise, the inverse of the metrics will be calculated. To speed-up the optimization process, evaluation of constraints will be checked using Table 7.2. If any constraint fails to satisfy in the initial design steps

Table 7.2.
Constraint Test

```

if  $C_S < C_I$ 
     $f = \epsilon \begin{bmatrix} 1 & 1 \end{bmatrix}^T \left( \frac{C_S - N_C}{N_C} \right)$ 
return
end

```

of the optimization problem, the optimization engine will stop the evaluation of the design and will move to next design. Note that this constraint check is not done after every constraint, but rather after computational intensive constraints, as documented in the Pseudo-Code shown in Table 7.3.

Table 7.3.
Pseudo-code for Calculation of the Fitness Function

1. Initialization and assign parameter vector
 - Semiconductor device rating selection
 - Determine semiconductor parameters
 - Calculate constant DC load current
2. Initialize electric generator metamodel

- Determine machine parameters for $P_{go,est}$ using (2.62)
- Determine electrical frequency using poles and ω_{rm}
- Calculate f_{sw} (using (7.3))
- Find generator circuit parameters using N_{s1} (2.68)
- Estimate machine currents using (7.9)
- Impose machine current density constraint c_1 (7.13)
- Limit rotor tip speed using c_2 (7.14)
3. Determine inductor dimensions using parameter vector
 - Calculate aspect ratio and impose constraint c_3 (7.15)
 - Compute core and winding volume and mass using (6.31)-(6.47)
 - Find winding resistance from (6.50)
 4. Determine DC and fundamental MMC current (4.5)-(4.6)
 - Solve the inductor MEC using (6.13)-(6.30), (6.51)
 - Impose constraint c_4 (7.16)
 - Compute flux density and L_{inc} (6.48)
 - Impose constraints c_5 and c_6 (7.17)-(7.18)
 - For EE-PMI: Solve MEC at no load , compute B, H_{mag}
 - Impose constraint c_7, c_8 and c_9 (7.19)-(7.21)
 - Find core loss density using (6.52)-(6.59)
 - Use Table 7.2 to test constraints
 5. Generate level shifted triangle waveforms
 - Calculate MMC $v_{a,conv}$ using (4.7) – (4.9)
 - Compute capacitor voltage (4.10) – (4.13), (4.26) – (4.29)
 - Determine duty cycle from (4.30) – (4.34)
 - Evaluate submodule switching signals using SPWM
 - Find MMC arm and DC bus capacitor currents (4.35) – (4.41)
 - Compute capacitor mass, ESR loss and ΔT_c (6.1)-(6.7)
 - Evaluate constraints $c_{10} - c_{17}$ on MMC (7.23)-(7.33)
 - Use Table 7.2 to test constraints

6. Calculate $P_{cd,up}$ using Table 5.1 and (5.1) – (5.4)
 Determine $P_{sw,up}$ using Table 5.2 and (5.5), (5.11)
 Determine submodule thermal model Fig. 5.10
 Impose constraint c_{18} on heat sink (7.34)
 Calculate P_{fan} and M_{hd} using (5.47)-(5.48)
 Determine inductor resistive losses using (6.50)
 Calculate inductor core loss (6.59)
 7. Determine system mass using (7.37)
 Compute total system loss using (7.39)
 Find P_{in} and $P_{in,est}$ using (7.35),(7.43)
 Impose constraint c_{19} (7.36)
 Use Table 7.2 to test constraints
 8. Evaluate power loss design metric using (7.44)
 Compute fitness function from (7.45)
- Return

7.2 PMAC-MMC Design Studies

In this section, case studies to demonstrate the functionality of the proposed design paradigm are presented. The notional system has a 5 kV DC bus with $P_{dc} = 1$ MW constant load. Two cases of design space involving EE-core and EE-PMI are considered and set forth in Table 7.4 and 7.5, respectively. The third column in the design space tables represents the gene encoding [58]. Parameters with “log” encoding are varied logarithmically and “lin” encoding are varied linearly [58]. Gene N , N_{wt} and N_{dt} are encoded logarithmically and rounded to an integer in the fitness function.

The parameter space for generator speed and specific torque density is found using [29]. DC bus utilization factor α_{ns1} is assumed to be between 0.5 and 1, where value of α_{ns1} limits the generator line-line peak voltage as compared to available DC bus voltage as shown in (2.68). Minimum and maximum limits on estimated MMC loss,

capacitance, inductor airgap and number of conductors are set after trial and error. Minimum and maximum limits on submodule count are based on the semiconductor voltage ratings. The minimum limit on N_{scpf} is found to limit minimum possible switching harmonics and adequately control capacitor voltages in a arm for practical operation operation of the MMC. The parameter domain for inductor dimensions such as core length, core width and magnet dimensions are difficult to intuit and so a large domain is used. Limits on w_{ac} are found using conductor data provided in [7].

Table 7.4.
Design Space for Case (a): EE-core Inductor

	Parameter	Description	Enc.	Min.	Max.
1	ω_{rm}	Generator Speed (rpm)	log	1000	8000
2	ρ_{TM}	Specific Torque Density (Nm/kg)	log	1	20
3	$P_{l,mmc,est}$	Estimated MMC Loss (W)	log	1	$5 \cdot 10^4$
4	α_{ns1}	Generator DC bus Utilization Factor	log	0.5	1
5	C_{sm}	Submodule Capacitance (F)	log	10^{-4}	$5 \cdot 10^3$
6	N	Number Of Submodules	log	4	14
7	N_{scpf}	Switching Cycles In Fundamental Cycle	lin	14	300
8	C_{in}	DC Bus Capacitance (F)	log	10^{-4}	$5 \cdot 10^3$
9	l_c	Length of Inductor Core (m)	log	10^{-3}	0.5
10	w_e	Width of Inductor End Leg (m)	log	10^{-3}	0.2
11	g_e	Inductor End Leg Airgap (m)	log	10^{-4}	10^{-2}
12	w_{ac}	Wire Cross-sectional Area (m^{-2})	log	10^{-9}	10^{-3}
13	N_{wt}	Conductors Along Inductor Width	log	1	10^2
14	N_{dt}	Conductors Along Inductor Depth	log	1	10^2

The fitness function presented in (7.45) will be maximized using Genetic Algorithm System Engineering Tool (GOSET) [58]. GOSET inherently maximizes the objective function and hence inverse of the metrics to be minimized is taken as vector-valued

Table 7.5.
Design Space for Case (b): EE-PMI

	Parameter	Description	Enc.	Min.	Max.
1	ω_{rm}	Generator Speed (rpm)	log	1000	8000
2	ρ_{TM}	Specific Torque Density (Nm/kg)	log	1	20
3	$P_{l,mmc,est}$	Estimated MMC Loss (W)	log	1	$5 \cdot 10^4$
4	α_{ns1}	Generator DC bus Utilization Factor	log	0.5	1
5	C_{sm}	Submodule Capacitance (F)	log	10^{-4}	$5 \cdot 10^3$
6	N	Number Of Submodules	log	4	14
7	N_{scpf_c}	Switching Cycles In Fundamental Cycle	lin	14	300
8	C_{in}	DC Bus Capacitance (F)	log	10^{-4}	$5 \cdot 10^3$
9	l_c	Length of Inductor Core (m)	log	10^{-3}	1
10	w_e	Width of Inductor End Leg (m)	log	10^{-3}	0.5
11	g_e	Inductor End Leg Airgap (m)	log	10^{-4}	10^{-2}
12	w_{ac}	Wire Cross-sectional Area (m^{-2})	log	10^{-9}	10^{-3}
13	w_{pm}	Width of Magnet Width (m)	log	10^{-3}	0.1
14	d_{pm}	Magnet Depth (m)	log	10^{-3}	0.1
15	N_{wt}	Conductor No. Along Inductor Width	log	1	10^2
16	N_{dt}	Conductor No. Along Inductor Depth	log	1	10^2

fitness, as shown in (7.45). For the optimization, population size of 2200 with 4500 number of generations is selected. For each case (EE-core and EE-PMI), the design optimization is run multiple times to demonstrate convergence using objective function based on Pseudo-code presented in Table 7.3. Results from the optimization runs are presented in the next subsection.

7.2.1 Optimization Results

The optimization study results will now be set forth. First, comparison of system optimization study results for Case (a) and (b) are shown in Fig. 7.1. From the loss vs mass comparison in Fig 7.1, it can be observed that the design results between multiple studies match closely. It is also noted that both Case (a) and (b) reached to similar designs which have system losses between 20-34 kW for designs with mass between 200 and 2000 kg. A substantial gain in performance due to utilization of the PMI is not observed in Fig 7.1.

To compare the system design parameters, study 3 from Case (a) (standard EE-core inductor) and study 1 from Case (b) (EE-PMI) are considered. For these studies, normalized parameter distribution for Case (a) and (b) are shown in Figs. 7.2 and 7.3 respectively. In the figures, the parameter distribution of each parameter is presented in the final generation for ranges normalized with respect to minimum and maximum limits (with respect to Tables 7.4 and 7.5). The horizontal coordinate of each parameter in its window shows its rank from worst design on the left to best design on the right with respect to system mass, and the vertical coordinate shows its position with respect to minimum and maximum parameter limits.

Next, various system parameters are presented in Figs. 7.4- 7.11 and compared. From Fig. 7.4-7.11 the variation in PMAC torque density, electrical frequency, MMC arm inductance, switching frequency, submodule capacitance, number of submodules, and DC bus capacitance respectively, with total system mass can be seen. It is interesting to note that the value of arm inductance and submodule capacitance do not vary monotonically with total mass. At low mass designs in EE-core case, a large value of arm inductance in Fig. 7.8 is observed at 400 kg due to low number of submodules (nearly 6) as seen in Fig. 7.9 and lower switching frequency (Fig. 7.7) which requires higher inductance to impede the high switching harmonic current. Similarly, for PMI designs, a jump in inductance is observed at 600 kg with a corresponding change in number of submodules. For lower mass designs, the switching frequency rises close

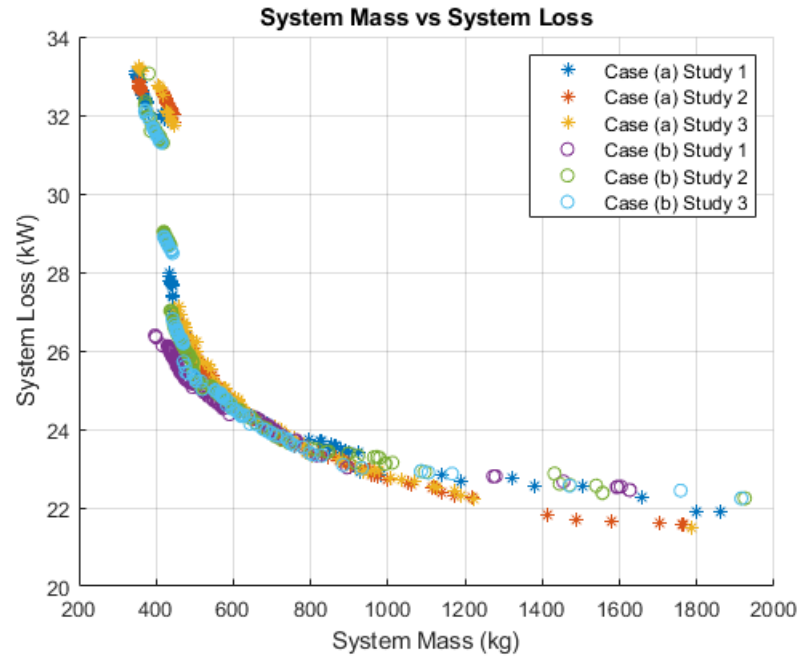


Fig. 7.1. System Loss vs Mass

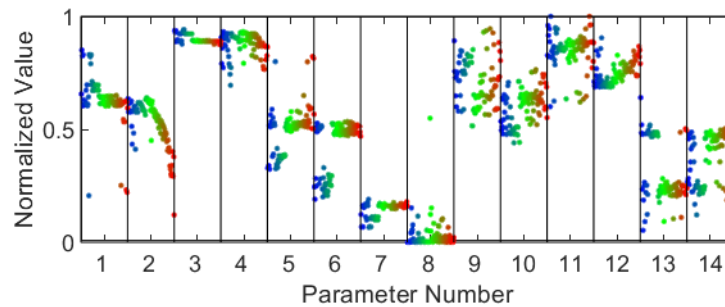


Fig. 7.2. Case (a): Standard EE-core MMC Parameter Distribution

to the maximum limit, as seen in Fig. 7.7. The generator q -axis current is shown in Fig. 7.11. The error in MMC loss estimation remained less than 0.002% in these studies.

System losses for the Case (a) and (b) are shown in Fig. 7.12-7.13, where it can be observed that system losses are comprised primarily of semiconductor losses. Fig. 7.14 and 7.15 presents individual component mass vs total system mass for Case (a)

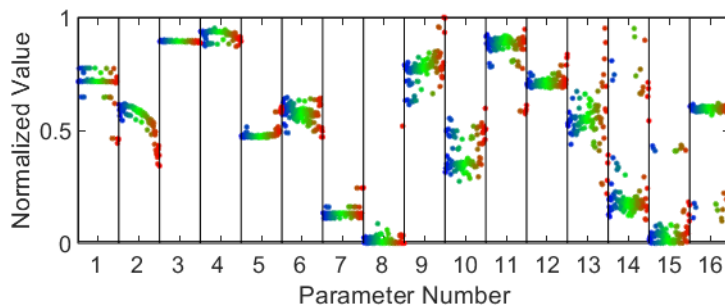


Fig. 7.3. Case (b): Standard EE-PMI MMC Parameter Distribution

and (b), respectively, and it can be seen that generator mass is the dominant part of total mass. In Fig. 7.14, it is noticed that heat sink mass decreases with increasing system mass. This is due to reduction in semiconductor losses, and hence requiring less heat sink to dissipate the generated heat.

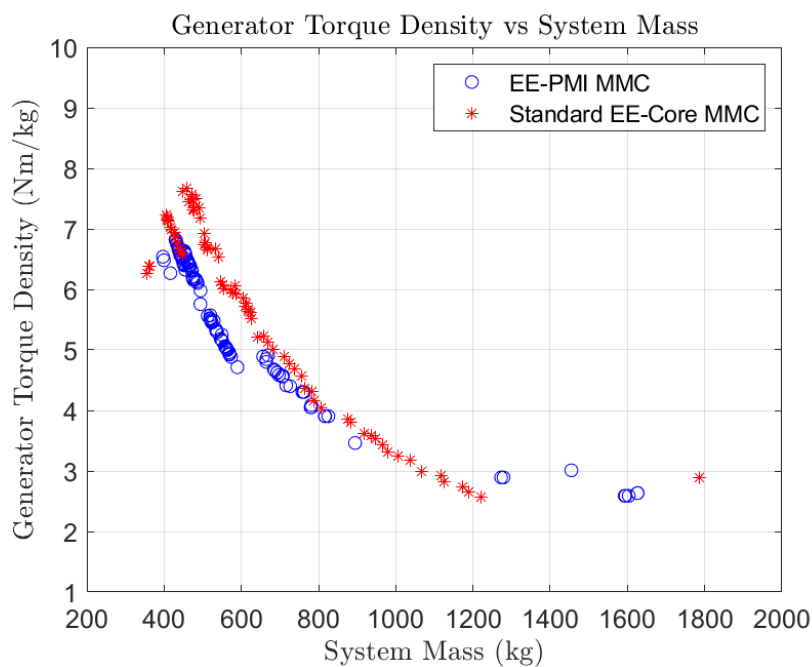


Fig. 7.4. Generator Specific Torque Density

As noted earlier, the EE-PMI does not significantly affect the system design metrics, and hence only design results for Case (a) with standard EE-core inductor will

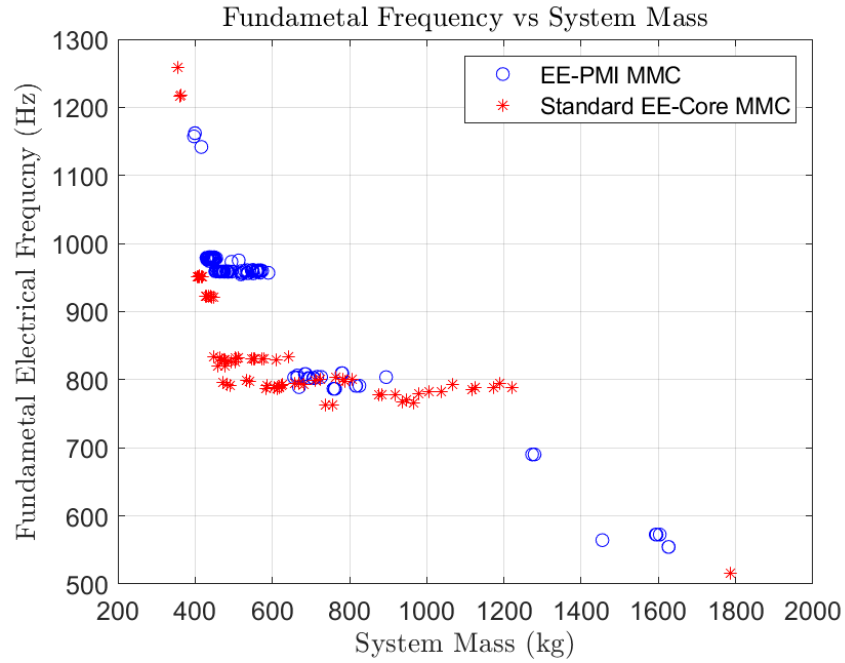


Fig. 7.5. Electrical Fundamental Frequency

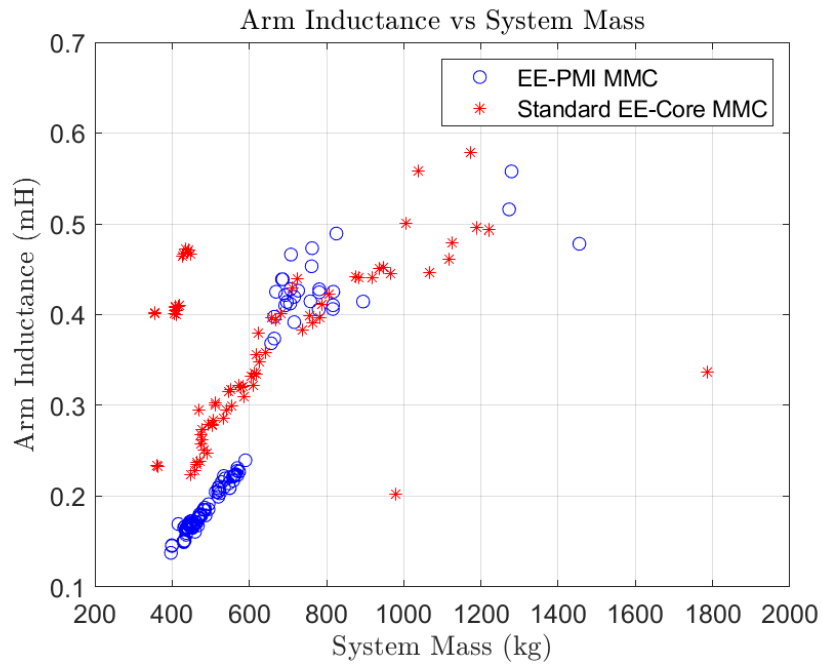


Fig. 7.6. MMC Arm Inductance

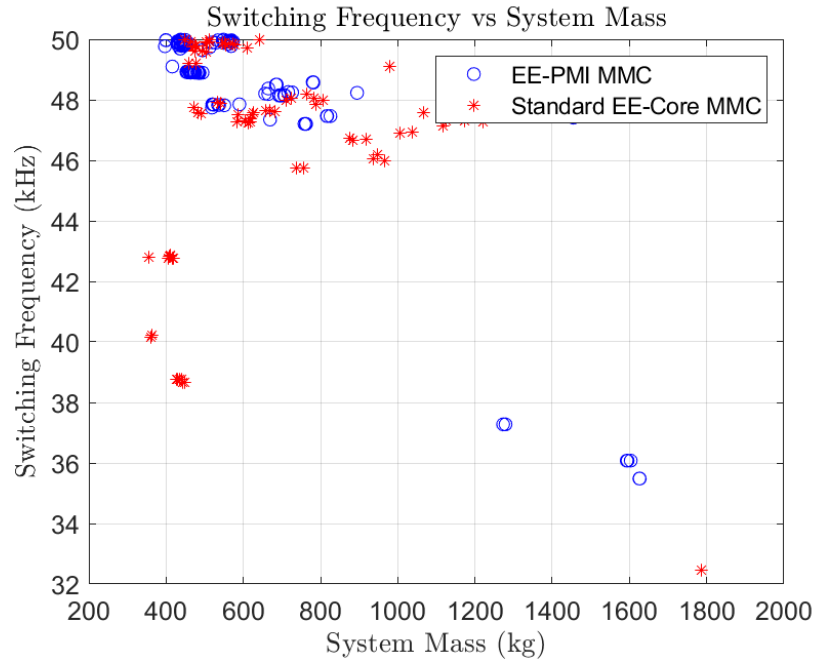


Fig. 7.7. Switching Frequency

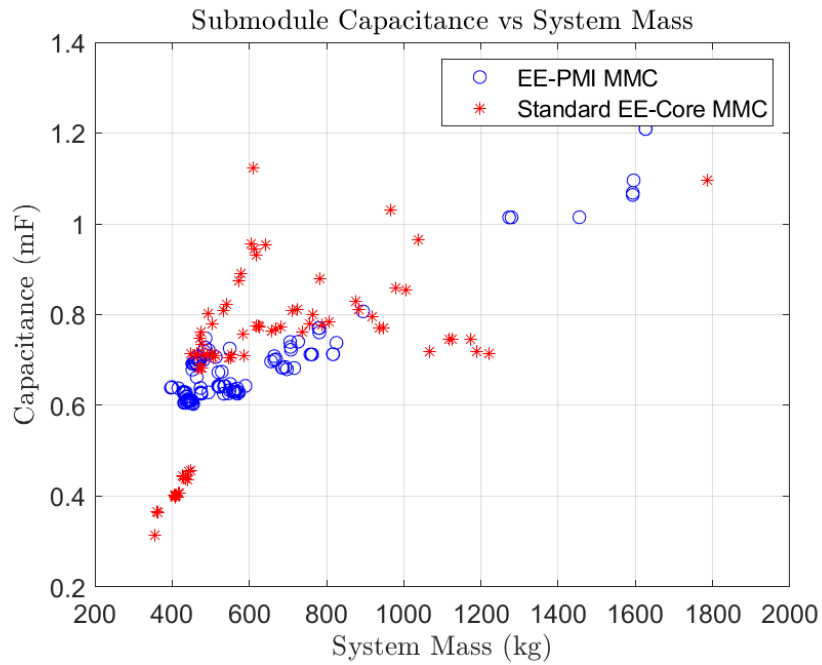


Fig. 7.8. Submodule Capacitance

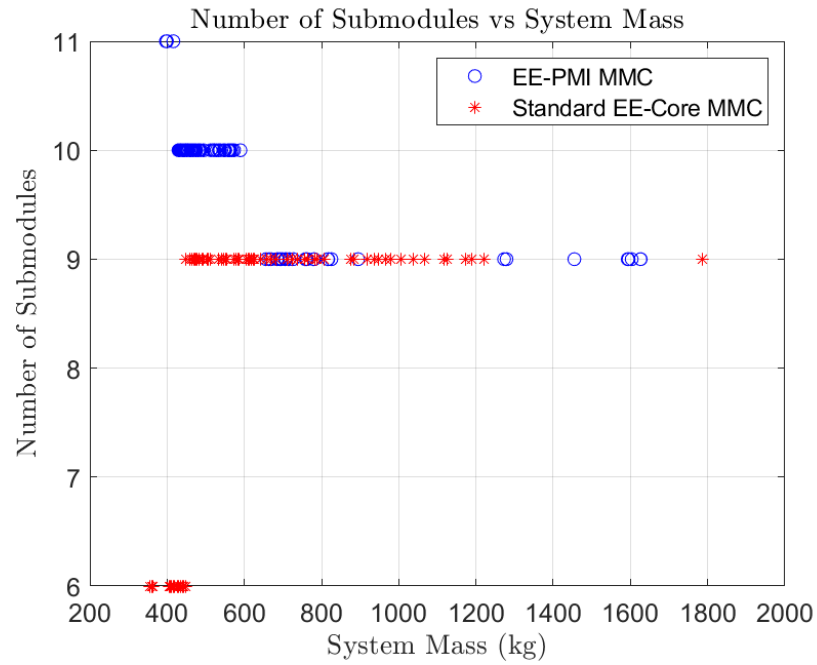


Fig. 7.9. Number of submodules

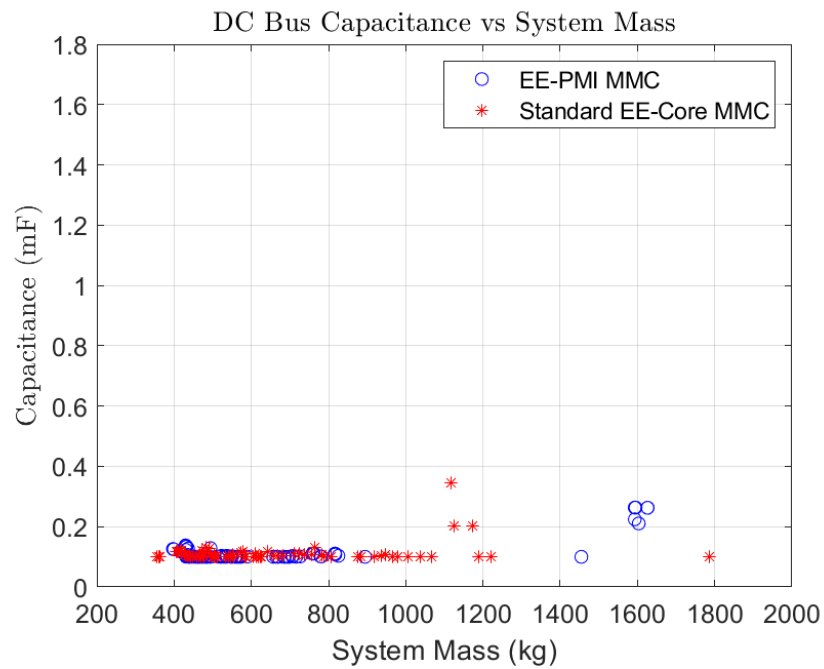


Fig. 7.10. DC Bus Capacitance

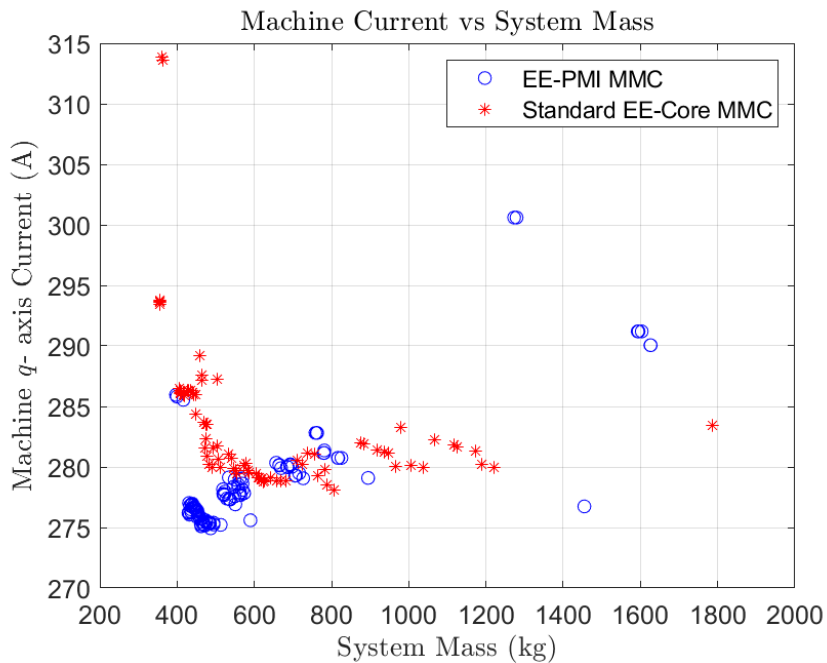
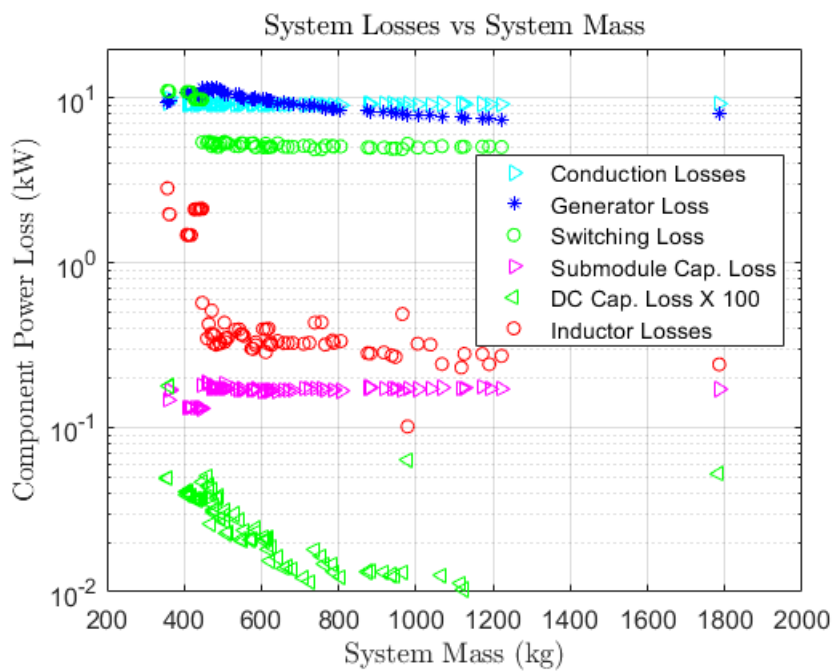
Fig. 7.11. Generator q -axis Current

Fig. 7.12. Case (a): System Component Loss

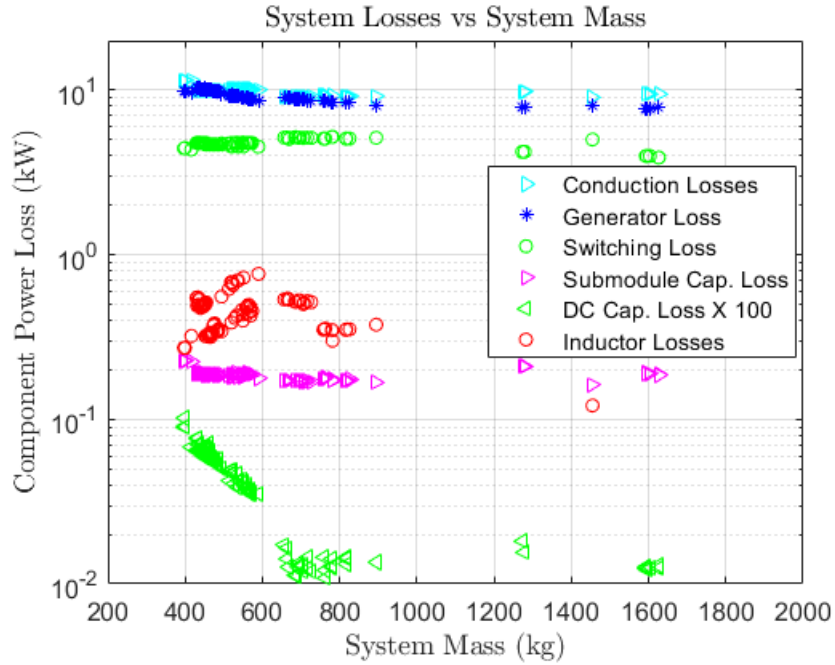


Fig. 7.13. Case (b): System Component Loss

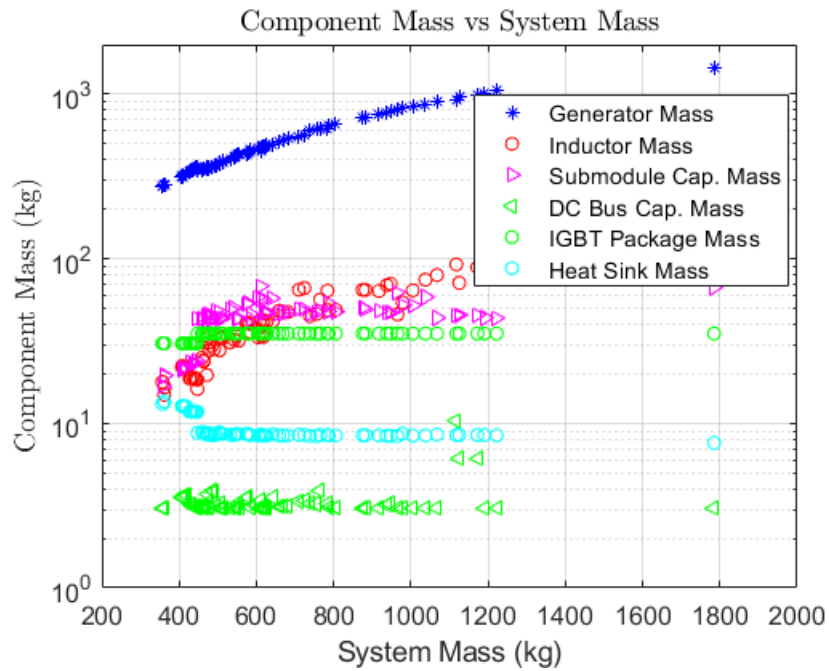


Fig. 7.14. Case (a): System Component Mass

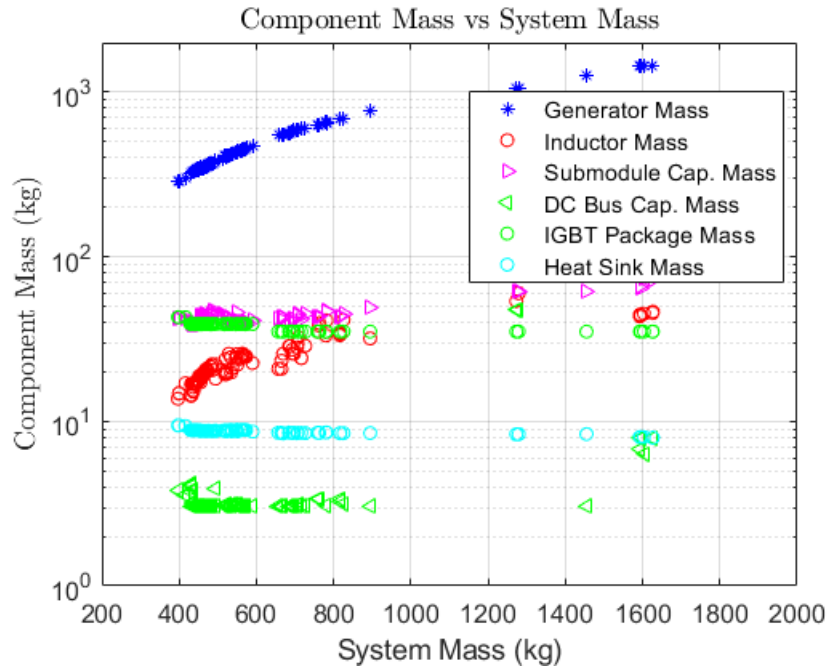


Fig. 7.15. Case (b): System Component Mass

be further discussed. Design parameters for Case (a) are shown in Table 7.6 for a design at system mass of 604 kg.

To validate the high-speed simulation, waveform-level model simulation (presented in Chapter 3) is carried out with parameters in Table 7.6. Comparison of waveforms from detailed simulation model is compared with high-speed simulation and is shown in Figs. 7.16-7.20. Generator, MMC upper arm and MMC lower arm currents shown in Figs. 7.16-7.18, respectively, match very closely. Submodule capacitor voltage variation is presented in Figs. 7.19-7.20 where it can be seen that the voltage ripple computed by detailed simulation model is 19.6 V as compared to 19.92 V in high-speed simulation.

Thus, the multi-objective optimization based design of a generator-rectifier system is complete. Complete mathematical formulation is shown along with detailed explanation of the formulated constraints and metrics used in the formulation.

Table 7.6.
Case (a) Design Results at 604 kg

Parameter	Value	Parameter	Value
PMAC Mass	466 kg	PMAC ρ_{TM}	5.86 Nm/kg
PMAC Resistive Loss	4.61 kW	PMAC Core Losses	5.27 kW
PMAC J_{pk}	7.72 A/mm ²	PMAC R_s	0.0372 Ω
PMAC L_q & L_d	275 μ H	PMAC λ_m	0.491 Vs
Number of Poles	26	Machine Speed	3639 rpm
Electrical Frequency	788.45 Hz	Machine Tip speed	165 m/s
EE-core w_e	26.2 mm	EE-core g_e & g_c	5.5 mm
EE-core l_c	55.5 mm	EE-core w_s	31.1 mm
EE-core d_s	46.65 mm	EE-core N_w	3
EE-core N_d	9	EE-core w_{ac}	48.44 mm ²
EE-core R_i	4.62 m Ω	EE-core L_{si}	0.33 mH
Each Inductor Power Loss	65.6 W	Each Inductor Mass	5.57 kg
Submodule Count	9	Switching Frequency	47.31 kHz
C_{sm}	0.96 mF	C_{in}	0.11 mF
M_{Csm}	1.07 kg	M_{Cin}	3.04 kg
Submodule Cap. ESR	2.26 m Ω	DC Bus Cap ESR	4.22 m Ω
Submodule Cap. $\Delta T_{c,sm}$	2.22 $^{\circ}$ C	DC Bus Cap ESR $\Delta T_{c,b}$	0.2 $^{\circ}$ C
$P_{cd,up}$	1.53 kW	$P_{sw,up}$	0.839 kW
Req. Heatsink $R_{th,S-a}$	0.25 K/W	Each heat sink M_{hd}	156 g
Each heat sink P_{fan}	3.3 W	Each submodule M_{sdp}	0.65 kg
Sub. Cap. volt. ripple	19.92 V	Sub. cap. rms current	36.99 A
Total MMC Mass	137.95 kg	Total MMC Loss	14.93 kW

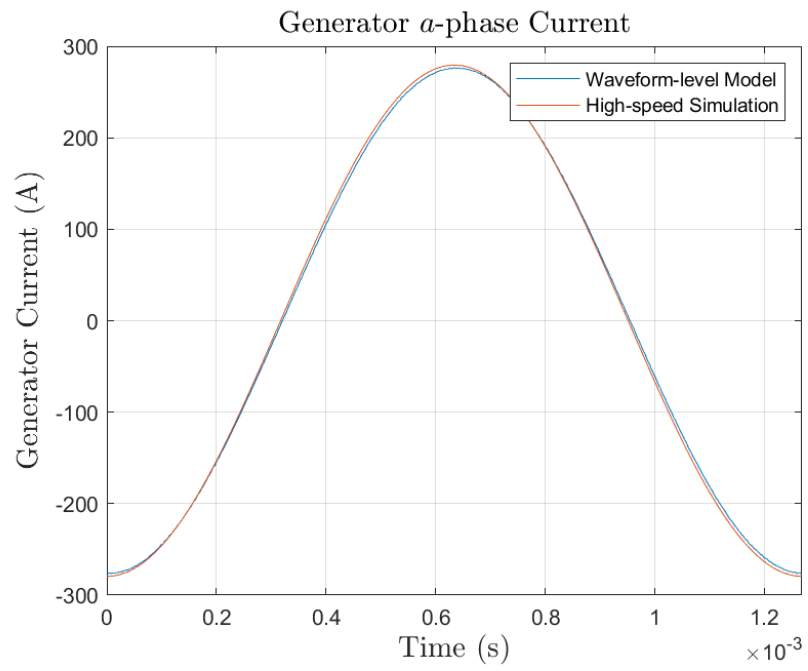


Fig. 7.16. Generator Current

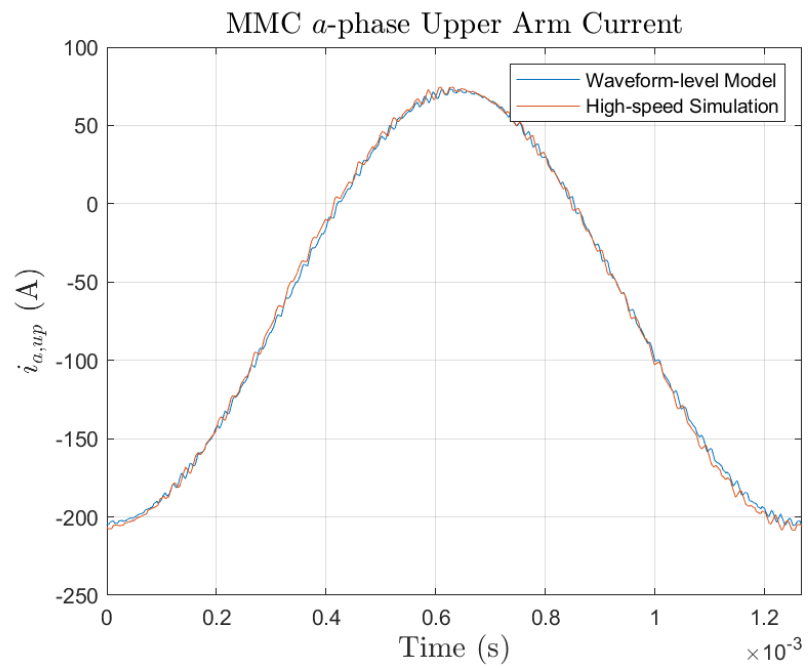


Fig. 7.17. MMC Upper Arm Current

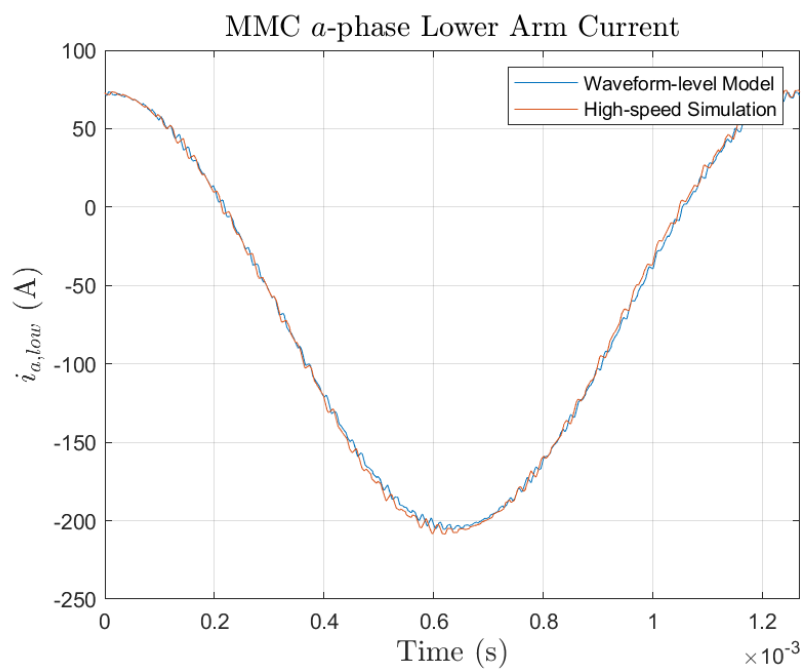


Fig. 7.18. MMC Lower Arm Current

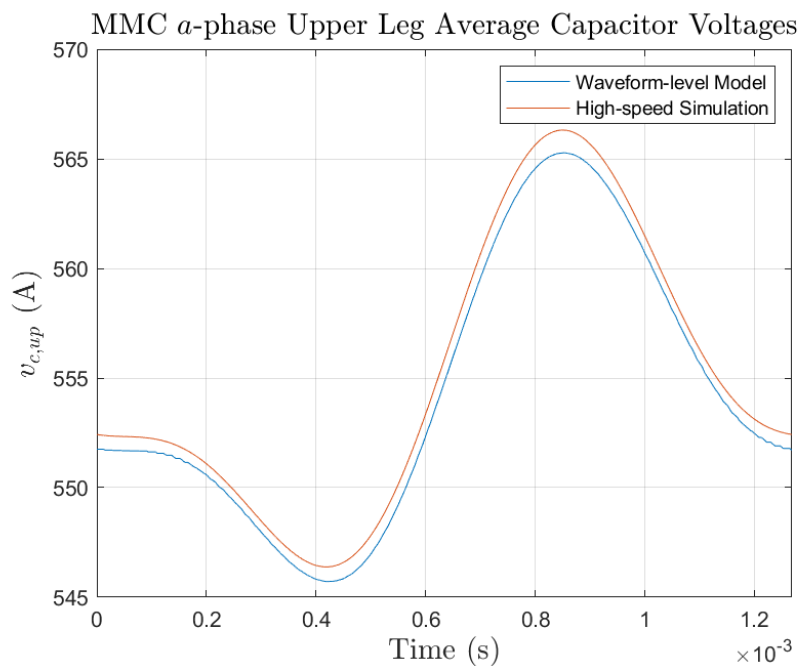


Fig. 7.19. MMC Upper Arm Submodule Capacitor Voltage Ripple

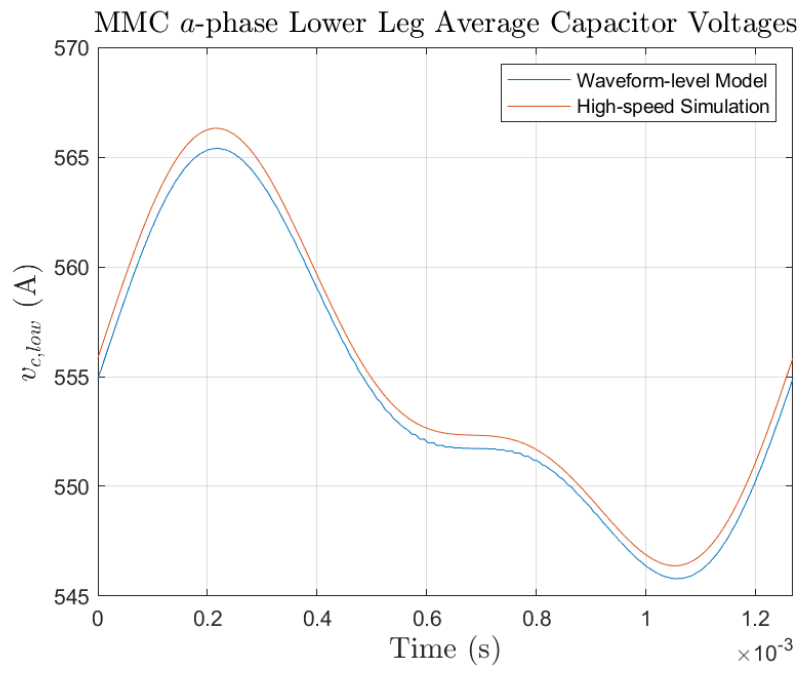


Fig. 7.20. MMC Lower Arm Submodule Capacitor Voltage Ripple

8. CONCLUSIONS AND FUTURE WORK

In this work, a design paradigm for a Modular Multilevel Converter based generator rectifier system is set forth. The proposed design methodology poses the design problem as a multi-objective optimization problem which optimizes the metrics of interest while satisfying the design constraints. A case study was conducted, and the design results were presented, including the operating waveforms. These were validated using a detailed waveform level simulation.

The major contributions of this work are: (a) the development of steady-state MMC high-speed simulation for its use in optimization tool, (b) inclusion of a PMAC generator in the design optimization using a metamodel based approach, (c) development of air cooled heat sink metamodel and MMC submodule thermal model, (d) consideration of different MMC arm inductor topologies, and finally, (e) development of optimization based design paradigm for the PMAC-MMC system utilizing the considered component models.

It is noted that the MMC, though contains multiple submodules at operates at high switching frequency, does not exhibit large semiconductor switching power losses. This is because of the fact that each submodule is not switched at every switching cycle. That is why the observed heat sink mass for the 1 MW MMC are relatively small. Consideration of semiconductor loss models and thermal model helped to achieve this result.

Permanent magnet based inductor and a standard inductor were considered for the MMC. Studies indicate that due to large fundamental component of current in MMC arms as compared to the DC component, PMI do no offer a large advantage to the system designs, and the trend in system mass vs loss is very close. During the design optimization, it is observed that the generator contributes to the largest portion to the system mass. Hence the multi-objective optimization engine has difficulties in

reducing mass of the component which do not contribute significantly to the system design, for example, arm inductor.

There are couple of areas for improvement in future for the development PMAC-MMC design optimization. The first area of improvement would be the consideration of multiple operating points for the system design. Though this seems trivial, due to usage of generator metamodel, an appropriate selection method of generator will be required. That is, appropriate generator power rating for given variation of load needs to be determined so that the generator is not under-utilized, remains in safe operating conditions and does not observe over-heating. This leads to the consideration of generator thermal behaviour in the generator metamodel which will help in predicting generator performance under short-term overloaded conditions, if required. On the MMC side, improvements in high-speed simulation are suggested by including advanced modulation schemes, and consideration of generator current switching harmonics.

REFERENCES

REFERENCES

- [1] R. M. N. Chaudhuri, B. Chaudhuri and A. Yazdani, *Multi-terminal Direct-Current Grids: Modeling, Analysis, and Control*. Wiley-IEEE Press, 2014.
- [2] C. Ng and P. McKeever, “Next generation hvdc network for offshore renewable energy industry,” in *10th IET International Conference on AC and DC Power Transmission (ACDC 2012)*, Dec 2012, pp. 1–7.
- [3] R. Soman, M. M. Steurer, T. A. Toshon, M. O. Faruque, and R. M. Cuzner, “Size and weight computation of mvdc power equipment in architectures developed using the smart ship systems design environment,” *IEEE Journal of Emerging and Selected Topics in Power Electronics*, vol. 5, no. 1, pp. 40–50, March 2017.
- [4] N. Doerry, “Next generation integrated power systems (ngips) for the future fleet,” in *Proc. IEEE Electr. Ship Technol. Symp. (ESTS)*, April 2009.
- [5] B. Wu and M. Narimani, *High-power converters and AC drives*. John Wiley & Sons, 2017.
- [6] S. Debnath *et al.*, “Operation, control, and applications of the modular multilevel converter: A review,” *IEEE Trans. Power Electron.*, vol. 30, no. 1, pp. 37–53, Jan 2015.
- [7] S. D. Sudhoff, *Power Magnetic Devices: A Multi-Objective Design Approach*. Wiley-IEEE Press, 2014.
- [8] Y. Li and F. Wang, “Arm inductance selection principle for modular multilevel converters with circulating current suppressing control,” in *2013 Twenty-Eighth Annual IEEE Applied Power Electronics Conference and Exposition (APEC)*, March 2013, pp. 1321–1325.
- [9] Q. Tu *et al.*, “Parameter design principle of the arm inductor in modular multilevel converter based hvdc,” in *2010 International Conference on Power System Technology*, Oct 2010, pp. 1–6.
- [10] L. M. Cunico, G. Lambert, R. P. Dacol, S. V. G. Oliveira, and Y. R. de Novaes, “Parameters design for modular multilevel converter (mmc),” in *2013 Brazilian Power Electronics Conference*, Oct 2013, pp. 264–270.
- [11] Y. Tang, L. Ran, O. Alatise, and P. Mawby, “Capacitor selection for modular multilevel converter,” *IEEE Trans. Ind. Apl.*, vol. 52, no. 4, pp. 3279–3293, July 2016.
- [12] J. Kolb, F. Kammerer, and M. Braun, “Dimensioning and design of a modular multilevel converter for drive applications,” in *2012 15th International Power Electronics and Motion Control Conference (EPE/PEMC)*, Sept 2012, pp. LS1a-1.1-1-LS1a-1.1-8.

- [13] H. Brnklaui, A. Gensior, and S. Bernet, "Submodule capacitor dimensioning for modular multilevel converters," *IEEE Trans. Ind. Appl.*, vol. 50, no. 3, pp. 1915–1923, May 2014.
- [14] A. J. Far, M. Hajian, D. Jovcic, and Y. Audichya, "Optimal design of high power mmc-based lcl dc/dc converter," in *2016 IEEE Power and Energy Society General Meeting (PESGM)*, July 2016, pp. 1–5.
- [15] A. A. J. Far, M. Hajian, D. Jovcic, and Y. Audichya, "High-power modular multilevel converter optimal design for dc/dc converter applications," *IET Power Electronics*, vol. 9, no. 2, pp. 247–255, 2016.
- [16] M. Karami and R. M. Cuzner, "Optimal sizing of modular multi-level converters designed for shipboard applications," in *2017 IEEE Electric Ship Technologies Symposium (ESTS)*, Aug 2017, pp. 605–611.
- [17] S. Am, P. Lefranc, D. Frey, and M. Ibrahim, "A generic virtual prototyping tool for multilevel modular converters (mmcs)," in *IECON 2015 - 41st Annual Conference of the IEEE Industrial Electronics Society*, Nov 2015, pp. 001 489–001 494.
- [18] A. A. Hillers, "Modular multilevel converters (mmcs) for grid-connected energy storage systems based on split batteries (sbess)," Ph.D. dissertation, ETH Zurich, 2018.
- [19] M. Bash, S. Pekarek, S. Sudhoff, J. Whitmore, and M. Frantzen, "A comparison of permanent magnet and wound rotor synchronous machines for portable power generation," in *2010 Power and Energy Conference At Illinois (PECI)*, Feb 2010, pp. 1–6.
- [20] O. Laldin, S. D. Sudhoff, and S. Pekarek, "Analysis and design of hybrid machines for dc generation," *IEEE Transactions on Energy Conversion*, vol. 30, no. 3, pp. 1192–1199, Sep. 2015.
- [21] P. R. O'Regan, R. Wang, and S. D. Pekarek, "Design of synchronous machines for dc power generation," in *2015 IEEE International Electric Machines Drives Conference (IEMDC)*, May 2015, pp. 1665–1670.
- [22] B. Zhang, S. Sudhoff, S. Pekarek, and J. Neely, "Optimization of a wide bandgap based generation system," in *2017 IEEE Electric Ship Technologies Symposium (ESTS)*, Aug 2017, pp. 620–628.
- [23] V. B. Honsinger, "Sizing equations for electrical machinery," *IEEE Transactions on Energy Conversion*, vol. EC-2, no. 1, pp. 116–121, March 1987.
- [24] Surong Huang, Jian Luo, F. Leonardi, and T. A. Lipo, "A general approach to sizing and power density equations for comparison of electrical machines," *IEEE Transactions on Industry Applications*, vol. 34, no. 1, pp. 92–97, Jan 1998.
- [25] F. Marignetti, M. A. Darmani, and S. M. Mirimani, "Electromagnetic sizing of axial-field flux switching permanent magnet machine," in *IECON 2016 - 42nd Annual Conference of the IEEE Industrial Electronics Society*, Oct 2016, pp. 1624–1628.

- [26] S. Vaschetto, A. Tenconi, and G. Bramerdorfer, "Sizing procedure of surface mounted pm machines for fast analytical evaluations," in *2017 IEEE International Electric Machines and Drives Conference (IEMDC)*, May 2017, pp. 1–8.
- [27] A. Tessarolo and M. Bortolozzi, "A sizing equation for slotless surface-mounted radially-magnetized permanent-magnet machines," in *2016 XXII International Conference on Electrical Machines (ICEM)*, Sep. 2016, pp. 1264–1269.
- [28] S. Stipetic, D. Zarko, and M. Popescu, "Ultra-fast axial and radial scaling of synchronous permanent magnet machines," *IET Electric Power Applications*, vol. 10, no. 7, pp. 658–666, 2016.
- [29] S. D. Sudhoff and R. Sahu, "Metamodeling of rotating electric machinery," *IEEE Trans. Energy Convers.*, vol. 33, no. 3, pp. 1058–1071, Sep. 2018.
- [30] S. D. Sudhoff, G. M. Shane, and H. Suryanarayana, "Magnetic-equivalent-circuit-based scaling laws for low-frequency magnetic devices," *IEEE Trans. Energy Convers.*, vol. 28, no. 3, pp. 746–755, Sept 2013.
- [31] R. Sahu, "Electric generator metamodel," 2019. [Online]. Available: <http://dx.doi.org/10.21227/wzwn-t754>
- [32] P. C. Krause, O. Wasynczuk, S. D. Sudhoff, and S. Pekarek, *Analysis of Electric Machinery and Drive Systems*. Wiley-IEEE Press, 2013.
- [33] M. Steurer, M. Bosworth, D. Soto, S. D. Sudhoff, S. D. Pekarek, R. Swanson, J. Herbst, S. Pish, A. Gattozzi, D. Wardell, M. Flynn, and T. Fikse, "Analysis of experimental rapid power transfer and fault performance in dc naval power systems," in *2015 IEEE Electric Ship Technologies Symposium (ESTS)*, June 2015, pp. 433–440.
- [34] B. Bahrani, S. Debnath, and M. Saeedifard, "Circulating current suppression of the modular multilevel converter in a double-frequency rotating reference frame," *IEEE Trans. Power Electron.*, vol. 31, no. 1, pp. 783–792, Jan 2016.
- [35] E. Canak, M. Carrasco, and F. Mancilla-David, "Modeling and control of a grid-connected small-scale windmill system using a pulse width modulated modular multilevel converter," in *2014 North American Power Symposium (NAPS)*, Sept 2014, pp. 1–6.
- [36] M. Saeedifard and R. Iravani, "Dynamic performance of a modular multilevel back-to-back hvdc system," *IEEE Trans. on Power Delivery*, vol. 25, no. 4, pp. 2903–2912, Oct 2010.
- [37] D. Shu, C. Zhang, X. Yu, and Q. Jiang, "A two-stage efficient model of modular multilevel converter for electromagnetic transient simulation," in *2016 18th European Conference on Power Electronics and Applications (EPE'16 ECCE Europe)*, Sept 2016, pp. 1–10.
- [38] J. Xu, A. M. Gole, and C. Zhao, "The use of averaged-value model of modular multilevel converter in dc grid," *IEEE Trans. on Power Delivery*, vol. 30, no. 2, pp. 519–528, April 2015.
- [39] H. Yang, Y. Dong, W. Li, and X. He, "Average-value model of modular multilevel converters considering capacitor voltage ripple," *IEEE Trans. on Power Delivery*, vol. 32, no. 2, pp. 723–732, April 2017.

- [40] A. Beddard, C. E. Sheridan, M. Barnes, and T. C. Green, "Improved accuracy average value models of modular multilevel converters," *IEEE Trans. on Power Delivery*, vol. 31, no. 5, pp. 2260–2269, Oct 2016.
- [41] F. Yu, W. Lin, X. Wang, and D. Xie, "Fast voltage-balancing control and fast numerical simulation model for the modular multilevel converter," *IEEE Trans. on Power Delivery*, vol. 30, no. 1, pp. 220–228, Feb 2015.
- [42] F. Xinkai, Z. Baohui, and W. Yanting, "Fast electromagnetic transient simulation models of full-bridge modular multilevel converter," in *2016 IEEE PES Asia-Pacific Power and Energy Engineering Conference (APPEEC)*, Oct 2016, pp. 998–1002.
- [43] J. Peralta, H. Saad, S. Denetiere, J. Mahseredjian, and S. Nguéfeu, "Detailed and averaged models for a 401-level mmc-hvdc system," *IEEE Trans. on Power Delivery*, vol. 27, no. 3, pp. 1501–1508, July 2012.
- [44] M. Lpez, F. Briz, A. Zapico, D. Diaz-Reigosa, and J. M. Guerrero, "Operation of modular multilevel converters under voltage constraints," in *2015 IEEE Energy Conv. Congress and Exposition (ECCE)*, Sept 2015, pp. 3550–3556.
- [45] R. Sahu and S. D. Sudhoff, "High-speed simulation of modular multilevel converters for optimization based design," in *2017 IEEE Electric Ship Technologies Symposium (ESTS)*, Aug 2017, pp. 134–141.
- [46] S. Wang, "Automated design approaches for power electronics converters," Ph.D. dissertation, Purdue University, West Lafayette, July 2010.
- [47] C. Gammeter, F. Krismer, and J. W. Kolar, "Weight optimization of a cooling system composed of fan and extruded-fin heat sink," *IEEE Trans. Ind. Apl.*, vol. 51, no. 1, pp. 509–520, Jan 2015.
- [48] U. Drogenik, A. Stupar, and J. W. Kolar, "Analysis of theoretical limits of forced-air cooling using advanced composite materials with high thermal conductivities," *IEEE Transactions on Components, Packaging and Manufacturing Technology*, vol. 1, no. 4, pp. 528–535, April 2011.
- [49] [Online]. Available: www.vishay.com/docs/26015/mkp1848cdclink.pdf
- [50] V. S. Duppalli and S. Sudhoff, "Power density comparison of three-phase ac inductor architectures," in *2017 IEEE Electric Ship Technologies Symposium (ESTS)*, Aug 2017, pp. 217–224.
- [51] S. D. Sudhoff, R. R. Swanson, A. E. Kasha, and V. S. Duppalli, "Magnetic analysis of symmetrical 3-phase y-core inductors," *IEEE Trans. Energy Convers.*, vol. PP, no. 99, pp. 1–1, 2017.
- [52] G. M. Shane and S. D. Sudhoff, "Design and optimization of permanent magnet inductors," in *2012 Twenty-Seventh Annual IEEE Applied Power Electronics Conference and Exposition (APEC)*, Feb 2012, pp. 1770–1777.
- [53] G. M. Shane and S. D. Sudhoff, "Design paradigm for permanent-magnet-inductor-based power converters," *IEEE Trans. Energy Convers.*, vol. 28, no. 4, pp. 880–893, Dec 2013.

- [54] [Online]. Available: http://www.hilltech.com/pdf/Hitachi/Datasheets/FINEMET_CMC_Core_FT-3KM_F_Series.pdf
- [55] [Online]. Available: media.digikey.com/pdf/Data%20Sheets/International%20Rectifier%20PDFs/ga400td25s.pdf
- [56] [Online]. Available: digikey.com/product-detail/en/microsemi-corporation/APTGT600A60G/APTGT600A60G-ND/1920683
- [57] [Online]. Available: www.pwr.com/pwr/docs/CM300DY-24S.pdf
- [58] [Online]. Available: https://engineering.purdue.edu/ECE/Research/Areas/PEDS/go_system_engineering_toolbox

APPENDICES

A. SEMICONDUCTOR DEVICE PARAMETERS

$\mathbf{V}_{sw,r}$	$\begin{bmatrix} 250 & 600 & 1200 \end{bmatrix}$ V
$\mathbf{I}_{sw,r}$	$\begin{bmatrix} 500 & 600 & 600 \end{bmatrix}$ A
$\mathbf{E}_{off,r}$	$\begin{bmatrix} 0.0371 & 0.0565 & 0.1334 \end{bmatrix}$ J
$\mathbf{E}_{on,r}$	$\begin{bmatrix} 0.0371 & 0.0136 & 0.1357 \end{bmatrix}$ J
$\mathbf{E}_{rr,r}$	$\begin{bmatrix} 0.0750 & 0.0460 & 0.0925 \end{bmatrix}$ J
$\mathbf{V}_{sw,fw}$	$\begin{bmatrix} 0.7705 & 0.6000 & 0.8000 \end{bmatrix}$ V
$\mathbf{R}_{sw,fw}$	$\begin{bmatrix} 0.001174 & 0.001528 & 0.002700 \end{bmatrix}$ Ω
$\mathbf{V}_{sw,d}$	$\begin{bmatrix} 0.6911 & 0.5600 & 0.7300 \end{bmatrix}$ V
$\mathbf{R}_{sw,d}$	$\begin{bmatrix} 0.002598 & 0.001700 & 0.003200 \end{bmatrix}$ Ω
$\boldsymbol{\alpha}_s$	$\begin{bmatrix} 0.7216 & 0.2547 & 0.7363 \end{bmatrix}$
$\boldsymbol{\beta}_s$	$\begin{bmatrix} 0.0022 & 0.0412 & 0.0089 \end{bmatrix}$
\mathbf{n}_s	$\begin{bmatrix} 0.9098 & 0.5306 & 0.8128 \end{bmatrix}$
$\boldsymbol{\alpha}_d$	$\begin{bmatrix} 0.4224 & 0.4766 & 0.4857 \end{bmatrix}$
$\boldsymbol{\beta}_d$	$\begin{bmatrix} 0.0493 & 0.0288 & 0.0467 \end{bmatrix}$
\mathbf{n}_d	$\begin{bmatrix} 0.5355 & 0.5411 & 0.5730 \end{bmatrix}$

B. POLYPROPYLENE CAPACITOR MODEL PARAMETERS

Table B.1.
Polypropylene Capacitor Model Parameters

Parameter	Value	Parameter	Value	Parameter	Value
α_{cm}	0.018	β_{cm}	27.56	γ_{cm}	0.64
V_{cm}	1.79	$\alpha_{c,esr,1}$	$3 \cdot 10^{-9}$	$\gamma_{c,esr,1}$	0.26
$\gamma_{c,esr,1}$	9.69	$\alpha_{c,esr,2}$	$7 \cdot 10^{-8}$	$\beta_{c,esr}$	0.0022
$V_{c,esr,1}$	584.28	$V_{c,esr,2}$	763.48	$V_{b,g}$	1200
$\alpha_{g,a}$	1.1948	$\alpha_{g,b}$	0.3619	$\alpha_{g,c}$	532.83
$\alpha_{g,d}$	3.9168	$\beta_{g,a}$	0.4067	$\beta_{g,b}$	183350
$\beta_{g,c}$	0.7285	$\beta_{g,d}$	$1.0168 \cdot 10^{-4}$	$T_{c,max}$	70 °C

C. INDUCTOR MATERIAL PARAMETERS

Table C.1.
FINEMET FT3-M Core Material Parameters

Parameter	Value
Density ρ	5704.5 kg/m^3
Low Frequency Core Loss	$k_{e,hf} = 4.32 \times 10^{-4}$ $\alpha_{ehf} = 2.106, \beta_{ehf} = 2.185$
High Frequency Core Loss	$k_e = 0, k_h = 4.33 \times 10^{-4}$ $\alpha = 2.105, \beta = 2.183$
μ_B Parameters	$\mu_r = 7.398 \times 10^5$ $\alpha = [1000 \ 0.2316 \ 0.2315 \ 0.444 \ 5.161 \times 10^{-3}]$ $\beta = [73.7 \ 4.53 \ 781.3 \ 87.52 \ 16.78]$ $\gamma = [50 \ 2.71 \ 0.946 \ 0.9548 \ 1.083]$

Table C.2.
Permanent Magnet Parameters

Material	B_r (T)	H_{ci} (kA/m)	ξ_m	ρ (kg/m ³)
NdFeB N35	1.19	-867	0.09	7500

D. FEA VALIDATIONS OF INDUCTOR MEC

Using the parameters of FINEMET material, 2-D Finite Element Analysis (FEA) of notional EE-PMI and standard EE-core are carried out using Ansys-Maxwell and the MEC solution is compared. The parameters of notional EE-PMI and standard EE-core inductors are shown in Tables. D.1 and D.2, respectively. Inductor material parameters are taken from Appendix C. Results for inductor validations are shown in Figs. D.2 and D.4 for EE-PMI and EE-core inductors, respectively. As can be seen, the MEC solution matches closely with 2D-FEA solution.

Table D.1.
EE-PMI Design Parameters

Parameter	Value	Parameter	Value
l_c	1 m	w_e	10 mm
w_s	10 mm	d_s	20 mm
g_e	1 mm	g_c	10^{-3} mm
w_w	8 mm	d_w	30 mm
d_{pm}	5 mm	w_{pm}	2 mm
w_{st}	4 mm	N_{tee}	0 - 1500 A turns
Core	FINEMET	PM	NdFeB N35

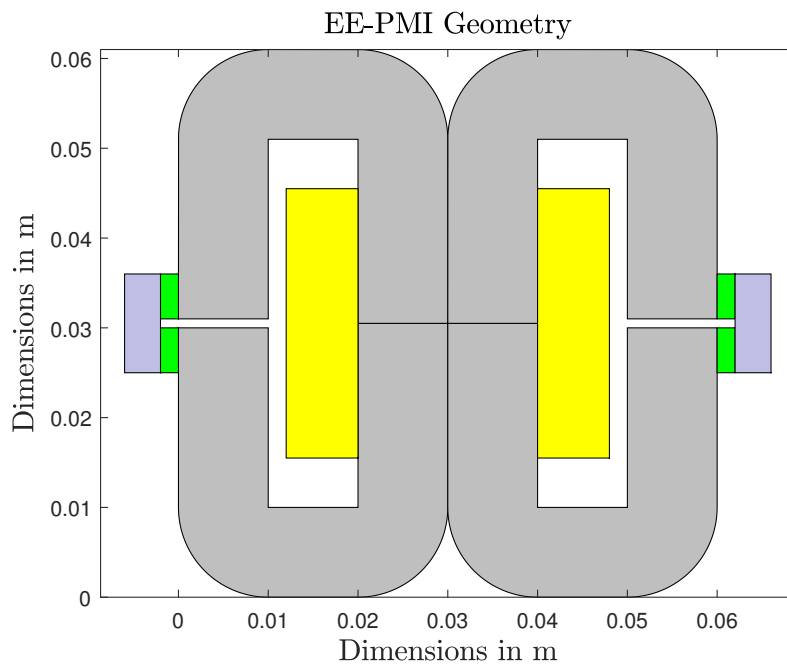


Fig. D.1. EE-PMI Geometry

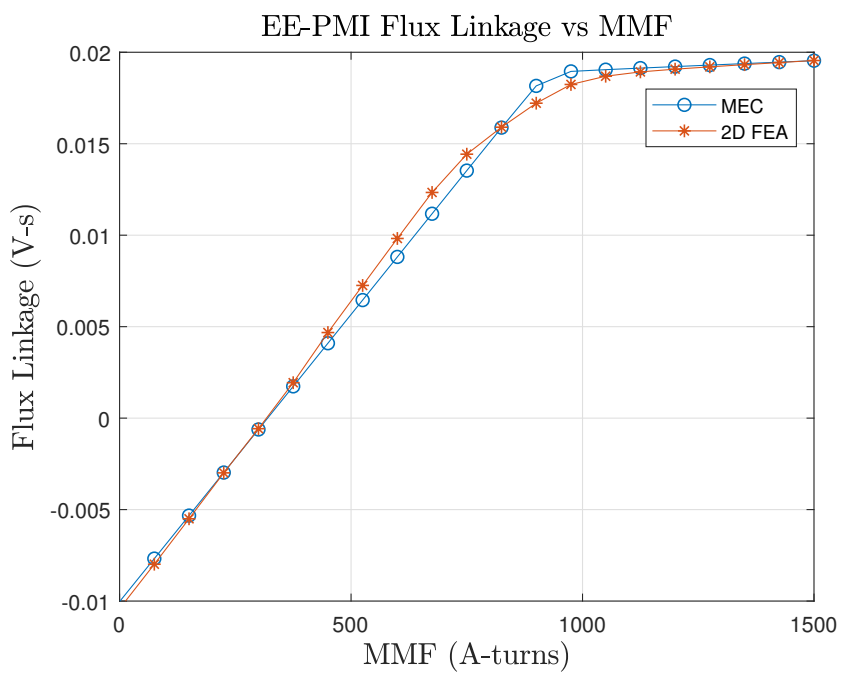


Fig. D.2. EE-PMI FEA Validation

Table D.2.
Standard EE-Core Design Parameters

Parameter	Value	Parameter	Value
l_c	1 m	w_e	10 mm
w_s	10 mm	d_s	20 mm
g_e	1 mm	g_c	1 mm
w_w	8 mm	d_w	30 mm
Core	FINEMET	$N_{ti_{ee}}$	0 - 1500 A turns

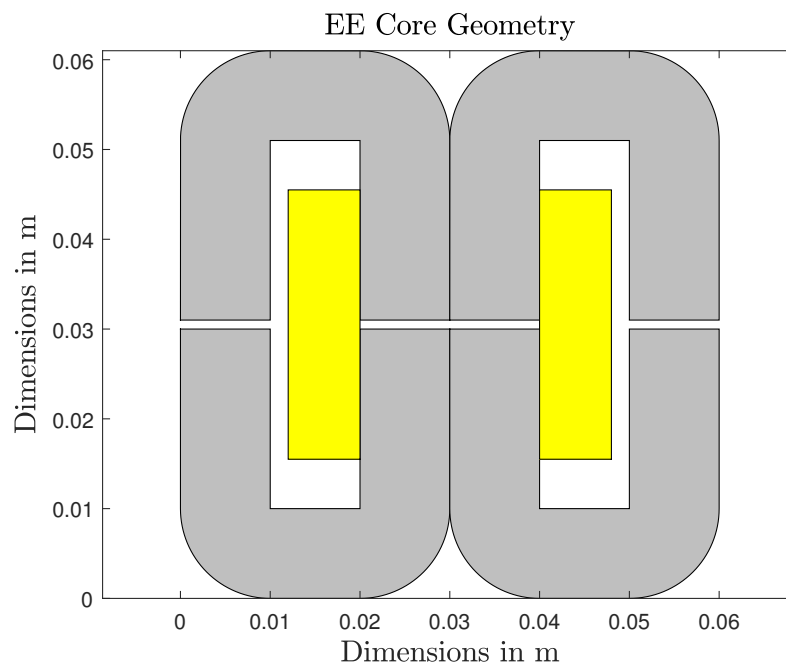


Fig. D.3. EE-Core Geometry

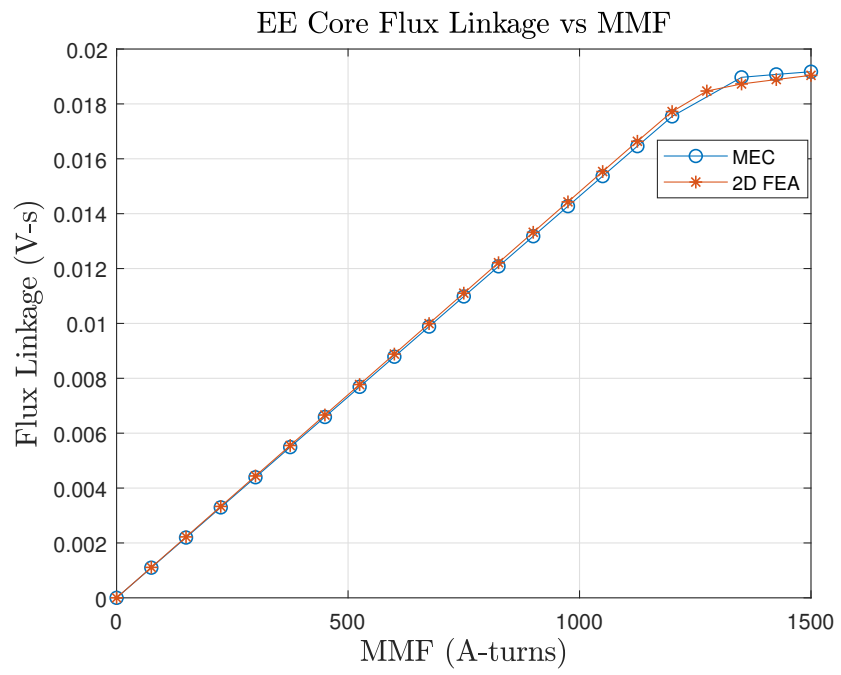


Fig. D.4. EE-Core FEA Validation

VITA

VITA

Raj Sahu received his with Bachelors (Hons.) in Electrical Engineering and Masters in Instrumentation and Signal Processing Engineering from Indian Institute of Technology, Kharagpur, in July 2014. He joined School of Electrical and Computer Engineering, Purdue University for Doctoral Program in Fall, 2014 with focus on Power and Energy Systems. During his course of study, he worked on medium to high voltage power electronic converter system design and optimization, and metamodel tools for electric machines. His research interests include high voltage power electronic converters, electric machinery design, MVDC microgrids, and multi-objective optimization.